A Combined Investigation of Iron and Silicon Isotopes in Meteorites:

Implications for Planetary Accretion and Differentiation

by

Soumya Ray

A Dissertation Presented in Partial Fulfillment
of the Requirements for the Degree
Doctor of Philosophy

Approved August 2021 by the
Graduate Supervisory Committee:

Meenakshi Wadhwa, Chair
Laurence Garvie
Christy Till
Richard Hervig
Devin Schrader

ARIZONA STATE UNIVERSITY

December 2021

ABSTRACT

Meteorites provide an opportunity to reconstruct the history of the Solar System. Differentiated meteorites, also called achondrites, are the result of melting and differentiation processes on their parent body. Stable isotopic compositions of differentiated meteorites and their components have added to the understanding of physical parameters, such as temperature, pressure, and redox conditions relevant to differentiation processes on planetesimals and planets in the early Solar System. In particular, Fe and Si isotopes have proven to be useful in advancing the understanding of physical and chemical processes during planetary accretion and subsequent evolution.

In this work, I developed a new method to simultaneously purify Fe and Si from a single aliquot of sample while ensuring consistently high yields and accurate and precise isotopic measurements. I then measured the Fe isotope compositions and Si contents of metals from aubrite meteorites to infer the structure and thermal evolution of their asteroidal parent body. Thereafter, I determined the combined Si and Fe isotope compositions of aubrite metals and the Horse Creek iron meteorite, and compared the magnitude of Si and Fe isotope fractionation factors between metal and silicates for both enstatite chondrites and aubrites to estimate the effect of high-temperature core formation that occurred on the aubrite parent body. I additionally assessed whether correlated Si and Fe isotope systematics can be used to trace core formation and partial melting processes for the aubrite parent body, angrite parent body, Mars, Vesta, Moon, and Earth. Finally, I measured the combined Fe and Si isotope composition of a variety of ungrouped achondrites and brachinites that record different degrees of differentiation under different redox conditions to evaluate the role of differentiation and oxygen fugacity in controlling their Fe and Si isotope compositions. Taken together, this comprehensive dataset reveals the thermal evolution of the aubrite parent body, provides insights into the factors

controlling the Fe and Si isotope compositions of various planetary materials, and helps constrain the bulk starting composition of planets and planetesimals.

This dissertation is dedicated to my grandparents who constantly reminded me that there is no substitute for education, hard work, perseverance, and a kind heart.

ACKNOWLEDGMENTS

Although I am the author of this document, this has not been a one-person job. Almost five years ago when I embarked on this journey, I had a faint inkling about the life-altering potential of this process but I was certain I would have the support of numerous people whose advice, guidance, and help has been instrumental in keeping me strong, grounded, and focused throughout.

First and foremost, I would like to thank my advisor, Meenakshi Wadhwa for giving me this opportunity and providing me with all the support and guidance throughout my time at ASU. I am also thankful to all the members of my committee over the years – Laurence Garvie, Christy Till, Rick Hervig, Devin Schrader, Steven Desch, and Jim Bell who have imparted their invaluable knowledge and expertise and enabled my growth as a scientist. I am extremely grateful to Vinai Rai, Rebekah Hines, Stephen Romaniello, Gwyneth Gordon, Tyler Goepfert, and Trevor Martin whose help and extensive knowledge about laboratory protocols and instruments facilitated data collection in the laboratory. I would also like to thank Axel Wittmann for being immensely helpful and accommodating during all the microprobe sessions and Joseph O'Rourke for many engaging discussions about planetary core formation. I am forever indebted to all the current and past members of the Center for Meteorite Studies and the Isotope Cosmochemistry and Geochronology Laboratory at ASU. I owe it to Talat Ahmad for his engrossing igneous petrology and geochemistry lessons which propelled me into the world of meteoritics and cosmochemistry.

I had never imagined I would have the privilege of calling my colleagues some of my closest friends. I would especially like to thank Zack Torrano, Emilie Dunham, Alice Stephant, and Prajkta Mane for making grad school memorable for me. Without them, it would have been a very mundane ordeal devoid of any humor or travel. I would also like to thank many other wonderful people I get to call my

friends: Samantha Jacob, Hannah Shamloo, Anusha Kalyaan, Alex Pye, Aleisha Johnson, Jessica Noviello amongst many others.

I would be remiss if I did not thank Rebecca Davis, Rebecca Dial, Juana Garcia, Cami Skiba, and many others who are undisputed, behind-the-scene heroes and have always been extremely helpful regardless of the frequency and length of my emails related to administrative and financial matters.

I am grateful to all my friends and family who have always encouraged and supported me. This would not have been possible without Batuk's love, support, and sacrifice. Last but not least, I would like to thank my parents, Santosh and Rajashree, who have always had unconditional love and support; my brother, Shakti, who is my biggest cheerleader; and all my canine friends who have brought unadulterated joy in my life.

This work was supported by a NASA Earth and Space Science Fellowship awarded to Soumya Ray and a NASA Emerging Worlds grant to Meenakshi Wadhwa.

TABLE OF CONTENTS

Page

LIST OF TABLES

LIST OF FIGURES

CHAPTER 1

INTRODUCTION

The advent of multi-collector inductively coupled plasma mass spectrometry (Halliday et al., 1995; Halliday et al., 1998) led the foray into non-traditional stable isotope geochemistry by enabling routine, high-precision isotopic measurements of elements other than the more traditional stable isotope systems of elements such as H, C, N, O, and S. Since then, stable isotopes of non-traditional elements have been utilized to answer a wide range of questions in the fields of planetary, earth, ocean, environmental, and biological sciences (for detailed reviews, see Johnson et al., 2004; Teng et al., 2017). In planetary science, stable isotopes are regarded as record-keepers of conditions of accretion, differentiation, and evolution of planetary bodies. Stable isotopes of non-traditional elements such as Mg, Si, Fe, Ni, Cr, and Ti amongst others have been utilized as tracers of spatial and temporal heterogeneity in the solar nebula (e.g., Warren, 2011; Kruijer et al., 2019; Kleine et al., 2020), evaporation and condensation processes (Richter et al., 2004; Richter et al., 2007; Poitrasson et al., 2004; Hin et al., 2017; Poitrasson et al., 2019), core formation (Bourdon et al., 2018 and references therein), partial melting and fractional crystallization in magma systems (Weyer and Ionov, 2007; Teng et al., 2008; Savage et al., 2011; Craddock et al., 2013), redox conditions during high-temperature processes (Williams et al., 2004; Dauphas et al., 2009; Pringle et al., 2013a; Bonnand and Halliday, 2018), and the compositions of planetary cores (Georg et al., 2007; Moynier et al., 2011a; Shahar et al., 2016).

In this thesis, I have reported and discussed the Fe and Si isotopic compositions of various planetary materials. Iron and Si isotopic compositions are particularly useful because both Fe and Si are major elements in planetary reservoirs and are sensitive to prevailing oxygen fugacity, temperature, and pressure conditions. As such, the Fe and Si isotopic compositions of meteorites can help to

advance our understanding of the (1) physical and chemical processes during planetary accretion and differentiation, and (2) bulk starting compositions of various planetary bodies.

Homogenization of Fe isotopes in the solar nebula occurred prior to the formation of chondrules and meteorite parent bodies (Zhu et al., 2001). Subsequent mass-dependent fractionation of Fe isotopes (expressed as $\delta^{56}Fe$, which is the deviation in parts per mil of $^{56}Fe/^{54}Fe$ ratio relative to IRMM-014 standard) during accretion and differentiation processes on these parent bodies provides an array of planetary materials with different Fe isotope compositions (e.g., Poitrasson et al., 2004; Weyer et al., 2005; Schoenberg and von Blanckenburg, 2006; Craddock and Dauphas, 2011; Wang et al., 2012; Wang et al., 2014 a and b). The specific processes responsible for inducing fractionation of Fe isotopes are debated and include (1) evaporation processes during accretion (Sossi and Moynier, 2017; Jordan et al., 2019) or due to impacts (Poitrasson et al., 2004; Liu et al., 2017; Poitrasson et al., 2019), (2) core formation or metal-silicate segregation (Shahar et al., 2015; Elardo and Shahar, 2017; Elardo et al., 2019) and, (3) magma differentiation (Weyer et al., 2005; Teng et al., 2008; Craddock et al., 2013). Similar to Fe isotopes, the absence of resolvable Si isotope anomalies in bulk meteorites suggests that primitive meteorites and bulk planetesimals formed in a reservoir that was isotopically homogenous with respect to Si (Pringle et al., 2013b). A major lithophile element, Si, exhibits siderophile behavior and enters the metallic phase under conditions of low oxygen fugacity or high temperature (Kilburn and Wood, 1997; Gessmann et al., 2001; Wade and Wood, 2005). Just as for Fe isotopes, mass-dependent variations in Si isotopes (expressed as $\delta^{30}Si$, which is the deviation in parts per mil of $^{30}Si/^{28}Si$ ratio relative to NBS-28 standard) have been demonstrated to be present in a variety of planetary materials. This variation in Si isotope compositions is interpreted to reflect (1) incorporation of Si into the core of a differentiated body (Georg et al.,

2007; Fitoussi et al., 2009; Armytage et al., 2011; Ziegler et al., 2010), (2) volatile depletion (Pringle et al., 2014; Moynier et al., 2020) or, (3) nebular condensation processes (Dauphas et al., 2015; Kadlag et al., 2019; Sikdar and Rai, 2020).

As is evident, the causes of systematic differences in Fe and Si isotopic compositions have been attributed to similar processes. Here, I conducted a combined investigation of the Fe and Si isotope compositions of a variety of meteorites to understand the origin of these isotopic variations in planetary materials. This thesis consists of the following chapters that are summarized below.

Chapter 2: A new method for the simultaneous chromatographic separation of silicon and iron for stable isotopic analyses by MC-ICPMS.

Fractionation of both Si and Fe isotopes are associated with a variety of processes ranging from high-temperature nebular and igneous processes to low-temperature biogeochemical processes. In previous studies, Fe and Si isotopes have typically been measured in separate aliquots of terrestrial and meteorite samples in an effort to better understand these processes. Here, we present a new alkali-fusion sample preparation method to simultaneously purify Si and Fe from the same aliquot of a given sample. The procedure involves fusing ~1 mg of homogenized sample with approximately 200 mg sodium hydroxide monohydrate ($NaOH.H_2O$) in a Teflon beaker followed by a two-step cation and anion column chromatography to separate Si and Fe. The Si and Fe isotope compositions of four terrestrial standards (BHVO-1, BCR-2, AGV-2, and diatomaceous earth) and one CV3 meteorite (Allende) were determined via the Thermo Neptune multi-collector ICPMS in high and medium resolution, respectively. To correct for instrumental mass bias, Si was doped with Mg while Fe was doped with Cu and mass bias correction was done using the exponential law. To determine the accuracy and precision of the isotope data, several tests were conducted which reveal that Si/Mg and Fe/Cu in samples should not deviate more

than 10% from that in the bracketing standard and presence of residual Na from the columns in the purified Si solutions adversely affects δ^{30}Si of that sample.

Chapter 3: Correlated iron isotopes and silicon contents in aubrite metals reveal structure of their asteroidal parent body.

In this chapter, we report the results of a correlated investigation of Fe isotope compositions and Si contents of Si-bearing metal grains from several aubritic meteorites. Based on their Fe isotopic and elemental Si compositions and thermal modelling, we show that these aubrite metals equilibrated with silicates at temperatures ranging from ~1430 K to ~1640 K and likely sampled different depths within their asteroidal parent body. We show that the highest temperature in this range corresponds to metal-silicate equilibration at a minimum depth of up to ~35 km from the surface of the aubrite parent body, followed by brecciation and excavation by impacts within 4.3 Myr after Solar System formation.

Chapter 4: Silicon and iron isotope compositions of aubrites and Horse Creek iron meteorite: Implications for using δ^{30}Si–δ^{56}Fe systematics as a tracer of core formation and partial melting.

Stable isotopes can help trace planetary differentiation processes such as formation of a metallic core and partial melting of the silicate mantle. The difference in Fe isotope compositions between chondrites and magmatic iron meteorites has been attributed to core formation on meteorite parent bodies. Similarly, the difference in the Si isotope compositions of chondrites and bulk silicate Earth (BSE) has been interpreted to reflect the incorporation of Si into Earth's core. Alternative mechanisms such as partial melting, evaporation and/or nebular condensation have also been invoked to explain the Fe and Si isotope compositions of distinct planetary materials. However, the simultaneous effect of core formation and partial melting on

both Fe and Si isotopes has not been considered so far. Here, I report the Si and Fe isotope composition of the Horse Creek iron meteorite and the Si isotope composition of a variety of aubrite metals for which the Fe isotopic compositions have already been reported and discussed in Chapter 3. Thereafter, I assess the isotopic effect of the segregation of a Si-bearing metallic core on the aubrite parent body and partial melting of the resulting mantle. Using similar lines of evidence, I also assess whether the Fe and Si isotope compositions of basalts from the angrite parent body, Mars, Vesta, the Moon, and Earth can be explained by the segregation of metallic cores followed by partial melting of their respective mantles.

Chapter 5: Combined silicon and iron isotope compositions of brachinites and ungrouped achondrites: Implications for oxygen fugacity and degree of partial melting in planetesimals.

In this chapter, I report the combined Si and Fe isotope compositions of bulk samples of brachinites and a variety of ungrouped primitive and other achondrites from distinct planetesimals to understand the fractionation of Si and Fe isotopes in response to varying degrees of silicate partial melting on planetesimals under different redox conditions. In this chapter, I assess whether combined Fe and Si isotope compositions of ungrouped achondrites can be used as tracers of differentiation processes on their parent bodies.

CHAPTER 2

A NEW METHOD FOR THE SIMULTANEOUS CHROMATOGRAPHIC SEPARATION OF SILICON AND IRON FOR CORRELATED STABLE ISOTOPIC ANALYSES BY MC-ICPMS

2.1 Introduction

The condensation temperature range of the three most abundant rock-forming elements, viz., Mg, Fe, and Si or the "common elements", separates volatile elements from refractory elements (Lodders, 2003). Isotopic fractionation of these "common elements" during nebular condensation (Dauphas et al., 2015; Sikdar and Rai, 2020), volatile depletion (Poitrasson et al., 2004; Young et al., 2009; Pringle et al., 2014; Sossi et al., 2016a and b; Hin et al., 2017; Young et al., 2019, Poitrasson et al., 2019), metal segregation (Georg et al., 2007; Shahar et al., 2009; Shahar et al., 2011; Ziegler et al., 2010; Hin et al., 2014; Shahar et al., 2015; Elardo and Shahar, 2017; Elardo et al., 2019, Shahar and Young, 2020), silicate differentiation (Weyer et al., 2005; Teng et al., 2008; Craddock et al., 2013; Telus et al., 2012; Savage et al., 2011; Sedaghatpour and Jacobsen, 2019; Zambardi et al., 2014; Gajos et al., 2016) and, biogeochemical processes (Brantley et al., 2001; Anbar, 2004; Sutton et al., 2018; Wang et al., 2019; Black et al., 2008) has been extensively studied.

Enrichment of heavy isotopes of Mg, Fe and Si in planetary materials has been attributed to the role of evaporation in accreting planetesimals (Poitrasson et al., 2004; Pringle et al., 2014; Hin et al., 2017; Young et al., 2019; Poitrasson et al., 2019). However, this hypothesis is not undisputed. Condensation from the nebula (Dauphas et al., 2015; Sikdar and Rai, 2020), core formation (Georg et al., 2007; Shahar et al., 2009; Shahar et al., 2011; Shahar et al., 2015; Elardo and Shahar, 2017; Elardo et al., 2019), and partial melting (Weyer et al., 2005; Teng et al., 2008; Craddock et al., 2013; Telus et al., 2012; Savage et al., 2011; Weyer and

Ionov, 2007; Savage et al., 2013; Teng et al., 2013) have been invoked to explain the Fe and Si isotope compositions of various planetary materials. Since solubility of Mg in Fe-rich metal is detectable beyond 3000 K (Wahl and Militzer, 2015; Takafuji et al., 2005; Fischer et al., 2015), fractionation of Mg isotopes, if any, during core formation will be obliterated at such high temperatures (Hin et al., 2017). However, Fe and Si isotope fractionation during metal-silicate equilibration has led to a long-standing debate.

Mass transfer of Fe during core formation leads to a change in the oxidation state (from Fe^{2+} or Fe^{3+} in silicates to Fe^{0} in metal) and, bonding environment. Such changes, according to first principles (Schauble, 2004; Young et al., 2015 and references therein), should be accompanied by a temperature-dependent fractionation of Fe isotopes. In pallasites (Poitrasson et al., 2005) and magmatic iron meteorites (Williams et al., 2006), which are considered to sample the core-mantle boundary and metallic cores of differentiated asteroids, respectively, heavy Fe isotope composition of metal compared to co-existing silicates and sulphides, seems to provide evidence for Fe isotope fractionation during core formation. This interpretation has subsequently been both supported (Shahar et al., 2015; Wang et al., 2015; Elardo and Shahar, 2017; Elardo et al., 2019) and challenged by experimental results (Poitrasson et al., 2007; Hin et al., 2012), isotopic analyses of meteorites (Poitrasson et al., 2019; Jordan et al., 2019), and nuclear resonant inelastic X-Ray spectroscopy of multi-anvil charges (Liu et al., 2017). Fractionation of Fe isotopes during partial melting has also been documented. For instance, terrestrial basalts show an offset in $\delta^{56}Fe$ of about ~0.1‰ from terrestrial mantle (Weyer et al., 2005; Craddock et al., 2013). Furthermore, a positive correlation between ^{56}Fe and SiO_2 wt% in granitoids has been attributed to magmatic differentiation (Telus et al., 2012; Zambardi et al., 2014).

Silicon, a lithophile or rock-forming element exhibits siderophile behavior and enters the metallic phase under conditions of low oxygen fugacity and high temperature (Kilburn and Wood, 1997; Gessmann et al., 2001; Wade and Wood, 2005). As with Fe isotopes, mass-dependent variations in Si isotopes have been reported to be present in a variety of planetary materials, and are interpreted to reflect either incorporation of Si into the core of a differentiated body (Georg et al., 2007; Ziegler et al., 2010; Armytage et al., 2011; Fitoussi et al., 2009), volatile depletion during impact processes or the magma ocean stage (Pringle et al., 2014; Hin et al., 2017; Young et al., 2019), equilibrium fractionation between forsterite (Mg_2SiO_4) and gaseous SiO in the solar nebula (Dauphas et al., 2015) or fractionation of light Si isotopes during Fe-metal condensation in the low C/O regions of the solar nebular (Sikdar and Rai, 2020). The effect of partial melting on Si isotopes is limited (Savage et al., 2014 and references therein); however, a correlation between the $\delta^{30}Si$ values and SiO_2 wt% of terrestrial rocks from equilibrium melt assemblages is observed (Savage et al., 2011; Savage et al., 2013; Savage et al., 2014; Zambardi et al., 2014).

The aforementioned studies clearly demonstrate that while the Fe and Si isotope compositions of a variety of meteoritic and terrestrial materials have been reported, a coupled investigation of these isotopes in the same sample aliquots has not yet been described. This is because the most common method of silicate digestion involves an acid mixture containing hydrofluoric acid (HF), which breaks down the silicate structure. However, volatile SiF_4 formed during the reaction between silicates and HF is lost, thereby precluding the measurement of Si isotopes in samples that are digested in this manner. To circumvent the loss of volatile SiF_4 and enable analyses of Si isotopes in silicate samples, the alkali fusion method is instead the method of choice (Georg et al., 2006; van Der Boorn et al., 2006; Fitoussi et al., 2009, Chakrabarti and Jacobsen, 2010; Armytage et al., 2011;

Zambardi and Poitrasson, 2011; Fitoussi and Bourdon, 2012; Zambardi et al., 2013; Pringle et al., 2013a; Pringle et al., 2014; Dauphas et al., 2015; Oelze et al., 2016; Sikdar and Rai, 2017; Sikdar and Rai, 2020). Since the Fe and Si isotopic composition of many terrestrial and meteoritic materials seem to be controlled by similar processes, a coupled investigation of both Fe and Si isotopes in bulk meteorites and mineral separates could provide important constraints on processes occurring during accretion and differentiation of meteorite parent bodies.

In this study, we report a new method for the simultaneous purification of Fe and Si isotopes from a single aliquot of sample. This will enable the high precision Fe and Si isotope measurement of the same sample. This in turn will help elucidate the Fe and Si isotopic composition of meteoritic materials, which could provide valuable insights into processes involved in their formation.

2.2 Materials and Methods

The sample set studied here includes the Allende CV3 meteorite, and 5 terrestrial standards, viz. NBS-28, diatomaceous earth, basalts (BCR-2, BHVO-1), and andesite AGV-2. All reagents used during the course of this work were selected to ensure low procedural blanks, including Merck Suprapur® Sodium hydroxide monohydrate flakes ($NaOH.H_2O$), and hydrochloric acid (HCl) which was distilled using the Savillex DST-1000 Acid Purification System. All water used for acid dilutions and column chromatography was passed through a Millipore Super-Q® water purification system (resistivity ~18 MΩ-cm) and a Millipore Milli-Q® water purification system with a 0.1 µm final filter (resistivity >18.2 MΩ-cm).

2.2.1 Sample digestion

To digest standards, approximately 1mg of homogenized powder of the standard was mixed with 200 mg of $NaOH.H_2O$ flakes in a 15 ml Teflon beaker. This

200:1 flux-sample mixture was heated on a hotplate at ~250°C for 96 hours to ensure complete digestion, following an alkali fusion technique adapted from and modified after previous studies (Georg et al., 2006; Oelze et al., 2006; Sikdar and Rai, 2017). During the course of this study, we found that unlike previously described methods of Chakrabarti and Jacobsen, 2010 and Sikdar and Rai, 2017; the addition of Milli-Q® water to the sample before heating caused the water to condense at the top of the beaker along the lid. This condensed water, in some cases, would drop to the bottom of the beaker and splatter the sample to the walls of the beaker inhibiting further reaction with the $NaOH.H_2O$. This typically resulted in incomplete dissolution of the sample in most cases. Milli-Q® water was, therefore, not added to samples prior to the heating step in this study, and the water in the $NaOH.H_2O$ crystals was adequate to form a slurry of sample and flux, ensuring complete digestion. After the 96-hour hotplate digestion step, the powders formed a fused cake at the bottom of the Teflon jar. Concentrated HCl and Milli-Q® water were then added to make a 10 ml clear solution with pH ~2 to ensure the predominance of silicic acid required for high Si yields during chromatographic separation.

2.2.2 Chromatographic purification of silicon and iron

All column chromatography was performed in the Class 1,000 clean Isotope Cosmochemistry and Geochronology Laboratory (ICGL) at Arizona State University, inside Class 10 or better fume hoods. The Fe and Si were purified using column methods modified after the combined protocols of Georg et al. (2006) and Sikdar and Rai (2017) for Si and Arnold et al. (2004) for Fe. To purify Si, 1.8ml of AG50W-X8 (200-400 mesh) cation exchange resin was cleaned using 8 mL each of 3 N HCl, 6 N HCl and 7 N HNO_3 and conditioned with ~20 mL Milli-Q® water. This is necessary to ensure that pH of the resin column is neutral before loading samples. Whole rock

solutions containing 25-40 μg of Si and proportional concentration of other elements (including Fe depending on the sample), were loaded onto the resin column. Elements such as Fe exist as cations in the solution and are adsorbed onto the cation exchange resin. But, since Si occurs as neutral or negative ions, it is not exchanged on the cation exchange resin, facilitating its elution using incremental volumes of a total 15 ml of Milli-Q® water. Silicon yields were typically better than 99%. The purified Si was acidified using concentrated HCl to make a final solution of 1 ppm Si doped with 0.5 ppm Merck Mg in 0.05 N HCl.

Table 2.1. Column chromatography procedure for simultaneous purification of Si and Fe from the same aliquot of sample.

Procedure	**Reagent**	**Volume**
Step 1: Si separation using 1.8 mL AG50W-X8 (200-400 mesh) cation exchange resin		
Column clean up	3N HCl, 6N HCl, 7N HNO_3	8 mL each
Column conditioning	Milli-Q® water	20 mL
Load sample (~25-40 μg Si)	0.01 N HCl (pH-2)	
Si elution	Milli-Q® water	15 mL
Cation elution into pre-cleaned* and pre-conditioned** 1 mL AG1-X8 (200-400 mesh) anion resin placed underneath the cation resin column	6N HCl	22 mL
Remove column with cation exchange resin.		
Step 2: Fe separation using 1mL AG1-X8 (200-400 mesh) anion exchange resin		
Matrix elution	6N HCl	16 mL
Fe elution	0.5 N HCl	14 mL
*Pre-cleaning AG1-X8 (200-400 mesh) anion resin	0.05 N HCl	10 mL
**Pre-conditioning AG1-X8 (200-400 mesh) anion resin	6 N	10 mL

After elution of Si from the cation resin column into collection beakers, a second column containing 1ml of pre-cleaned and pre-conditioned AG1-X8 anion exchange resin was placed under the cation resin column. To elute the cations adsorbed on the cation exchange resin, 22 ml of 6N HCl was passed through it. In a 6 N HCl medium, Fe has low distribution co-efficient (K_d) for cation exchange resin. After being eluted from the cation exchange resin, Fe gets adsorbed on the anion exchange resin placed below. After this, the resin column with the cation exchange resin was removed and an Fe separation procedure (adapted from Arnold et al.,

2004) was carried out. To separate Fe from the anion exchange resin, 24 ml of 6N HCl was passed to elute cations such as Na, Mg, Al, Ca, Ti, V, Cr, Ni, Cu followed by 14 ml of 0.5 N HCl to elute Fe. The Fe cut was then dried down on a hot plate and brought up in 2% HNO_3. About 5% of the aliquot was used to measure yields of the Fe columns on the Quadrupole-ICPMS which were always better than 98.5%. The remaining aliquot was diluted to an Fe concentration of 0.5 ppm doped with 0.5 ppm of NIST Cu (in 2% HNO_3) for measurement of Fe isotopes.

Table 2.2. Parameters for the measurement of Si and Fe isotopes.

	Si isotope measurement	**Fe isotope measurement**
Radio frequency power	1200 W	1200 W
Extraction lens voltage	−2000 V	−2000 V
Focus (Typical)	~ −630	~ −690
Skimmer cone	H	H
Sampler cone	Jet	Jet
Slit resolution	High	Medium
Faraday cup set-up	^{28}Si (L2) - ^{28}Si (C) - ^{30}Si (H2) ^{24}Mg (L3) - ^{25}Mg (L1) - ^{26}Mg (H1)	^{54}Fe (L2) - ^{56}Fe (C) - ^{57}Fe (H1) ^{63}Cu (L1) - ^{65}Cu (C)
Resolving power	~10000	~8500
Measurement mode	Two-line measurement	Two-line measurement
Sample gas (Argon)	0.980 L/min	0.976 L/min
Cool gas (Argon)	15.75 L/min	15.75 L/min
Auxiliary gas (Argon)	0.90 L/min	0.80 L/min
Rinsing time	120 s	120 s
Uptake time	60 s	60 s
Sample concentrations	Si: 1 ppm; Mg: 0.5 ppm	Fe: 0.5 ppm; Cu: 0.5 ppm
Nebulizer flux	~100 μL/min	~100 μL/min
Element consumption per analysis	10 μg Si; 5 μg Mg	3 μg Fe; 3 μg Cu

2.2.3 Measurement of silicon isotopes

Silicon isotopic data were acquired with the Thermo Finnigan Neptune multi-collector inductively coupled plasma mass spectrometer (MC-ICPMS) at ASU using a

jet sample cone and an H-skimmer cone in high resolution mode (i.e., with a mass resolving power >10000). Samples were introduced through an ESI APEX desolvating nebulizer attached to a self-aspirating PFA probe with an uptake rate of 100 μL/min. An uptake time of 60 s and a wash time between consecutive sample and standard measurements of 120 s were used for each cycle. Each run for a sample, standard, or blank comprised 30 cycles with an 8 s integration time per cycle. The purified Si standards were analyzed at concentrations of 1 ppm doped with 0.5 ppm Merck Mg to correct for instrumental mass bias. Typical signal sensitivity for ^{28}Si signal was ~9 V/ppm Si using a $10^{11}\Omega$ resistor. Data were collected by switching between two different cup configurations wherein ^{28}Si, ^{29}Si, and ^{30}Si isotopes were measured in parallel during the first integration of 8 s using the L2, C, and H2 Faraday cups respectively. Subsequently,^{24}Mg, ^{25}Mg, and ^{26}Mg were measured during the second integration of 8 s using the L3, L1, and H1 Faraday cups, respectively. Instrumental mass fractionation was corrected for using the exponential mass fractionation law such that corrected isotope ratio (denoted by an asterisk) is

$$\left(\frac{^{x}\mathrm{Si}}{^{28}\mathrm{Si}}\right)^{*} = \left(\frac{^{x}\mathrm{Si}}{^{28}\mathrm{Si}}\right)_{\mathrm{measured}} \times \left(\frac{\mathrm{M_x}}{\mathrm{M_{28}}}\right)^{\beta} \quad (2.1)$$

where ^{x}Si is ^{29}Si or ^{30}Si, M_x and M_{28} are masses of ^{x}Si and ^{28}Si respectively and β is defined by

$$\beta = \frac{\ln\left[\frac{\left(\frac{^{25}\mathrm{Mg}}{^{24}\mathrm{Mg}}\right)_{\mathrm{true}}}{\left(\frac{^{25}\mathrm{Mg}}{^{24}\mathrm{Mg}}\right)_{\mathrm{measured}}}\right]}{\ln\left(\frac{\mathrm{M_{25}}}{\mathrm{M_{24}}}\right)} \quad (2.2)$$

where $(^{25}\mathrm{Mg}/^{24}\mathrm{Mg})_{\mathrm{true}}$ is assumed to be 0.1265187 and M_{25}, M_{24} are masses of ^{25}Mg and ^{24}Mg respectively. Silicon isotope compositions are reported using the δ notation,

i.e., parts per thousand deviation (‰) relative to the bracketing standard NBS-28 according to

$$\delta^{30}\mathrm{Si}(‰) = \left[\frac{\left(\frac{^{30}\mathrm{Si}}{^{28}\mathrm{Si}}\right)^{*}_{\text{sample}}}{\left(\frac{^{30}\mathrm{Si}}{^{28}\mathrm{Si}}\right)_{\text{standard}}} - 1\right] * 1000 \qquad (2.3)$$

Silicon isotope values for each sample run is the average of six repeats and is reported with the internal 2SE of these measurements or the external long-term reproducibility, whichever is larger. The external reproducibility of our analyses based on repeated measurements of the NBS-28 bracketing standard over the course of this study is 0.015‰ for δ^{29}Si and 0.016‰ for δ^{30}Si (Fig. 2.1).

2.2.4 Measurement of iron isotopes

Iron isotopic data were acquired with the Thermo Finnigan Neptune multi-collector inductively coupled plasma mass spectrometer (MC-ICPMS) at ASU using a jet sample cone and an H-skimmer cone in medium resolution mode (i.e., with a mass resolving power >8500). Samples were introduced through an ESI APEX desolvating nebulizer attached to a self-aspirating PFA with an uptake rate of 100 μL/min. An uptake time of 60 s and a wash time between consecutive sample and standard measurements of 120 s were used for each cycle. Typical sensitivity achieved for ^{56}Fe signal was ~70V/ppm Fe using a $10^{11}\Omega$ resistor. Data were collected by switching between two different cup configurations wherein ^{53}Cr, ^{54}Fe, ^{56}Fe, ^{57}Fe, ^{58}Fe, and ^{60}Ni isotopes were measured in parallel during the first integration of 8 s using the L4, L2, C, H1, H2, and H4 Faraday cups respectively. Subsequently, ^{63}Cu and ^{65}Cu were measured during the second integration of 4 s using the L1 and C Faraday cups respectively. Each run for a sample, standard, or blank comprised 20 cycles. Measurements of ^{53}Cr and ^{60}Ni were used to correct for potential isobaric interferences of ^{54}Cr and ^{58}Ni on ^{54}Fe and ^{58}Fe, respectively. All

data reduction was performed offline using the Iolite software. Instrumental mass fractionation was corrected for using the exponential mass fractionation law such that corrected isotope ratio (denoted by an asterisk) is

$$\left(\frac{^{x}Fe}{^{54}Fe}\right)^{*} = \left(\frac{^{x}Fe}{^{54}Fe}\right)_{measured} \times \left(\frac{M_x}{M_{54}}\right)^{\beta} \quad (2.4)$$

where ^{x}Fe is ^{56}Fe or ^{57}Fe, M_x and M_{54} are masses of ^{x}Fe and ^{54}Fe respectively and β is defined by

$$\beta = \frac{\ln\left[\frac{\left(\frac{^{63}Cu}{^{65}Cu}\right)_{true}}{\left(\frac{^{63}Cu}{^{65}Cu}\right)_{measured}}\right]}{\ln\left(\frac{M_{63}}{M_{65}}\right)} \quad (2.5)$$

where $(^{63}Cu/^{65}Cu)_{true}$ is assumed to be 2.24359 and M_{63}, M_{65} are masses of ^{63}Cu and ^{65}Cu respectively. Iron isotope compositions are reported using the δ notation, i.e., parts per thousand deviation (‰) relative to the bracketing standard IRMM-014 according to

$$\delta^{x}Fe(‰) = \left[\frac{\left(\frac{^{x}Fe}{^{54}Fe}\right)^{*}_{sample}}{\left(\frac{^{x}Fe}{^{54}Fe}\right)_{standard}} - 1\right] * 1000 \quad (2.6)$$

Iron isotope value for each sample is the average of six repeats and is reported with the corresponding internal 2SE of these measurements or the external long-term reproducibility, whichever is larger. The long-term external reproducibility of our analyses based on repeated measurements of the IRMM-524A bracketing standard over the course of this study is 0.010‰ for $\delta^{56}Fe$ and 0.022‰ for $\delta^{57}Fe$ (Fig. 2.1).

2.3 Results and Discussion

The Si and Fe isotope data from a single aliquot of sample analyzed in this study are reported in Table 2.3. Silicon isotope (δ^{29}Si and δ^{30}Si) and iron isotope values (δ^{56}Fe and δ^{57}Fe) calculated using both the sample standard bracketing only technique (SSB), and sample standard bracketing doped with Mg (for Si) or Cu (for Fe) (SSB+Mg or SSB+Cu respectively) have been reported. The δ^{29}Si (‰) for Allende = −0.21±0.07 (2SD); diatomaceous earth = 0.65±0.04 (2SD); BCR-2 = −0.12±0.04 (2SD); BHVO-1 = −0.14±0.03 (2SD); and AGV-2= −0.14±0.03 (2SD). The δ^{56}Fe (‰) for Allende = 0.01±0.01 (2SD); BCR-2 = 0.08±0.03 (2SD); BHVO-1 = 0.12±0.04 (2SD); and AGV-2=0.12±0.03 (2SD). Corresponding δ^{30}Si (‰) and δ^{57}Fe (‰) of analyzed standards are mass-dependent such that are δ^{30}Si = ~2* δ^{29}Si (‰) and δ^{57}Fe = ~1.5* δ^{56}Fe (‰).

Table 2.3. Summary of Si and Fe isotope data for 5 terrestrial standards and Allende CV3 chondrite.

Sample	δ^{29}Si ± 2SD	δ^{30}Si ± 2SD	δ^{56}Fe ± 2SD	δ^{57}Fe ± 2SD
Allende (this study)	−0.21±0.07	−0.46±0.13	0.01±0.01	0.04±0.01
Lit. value	−0.23±0.09	−0.45±0.16	0.00±0.04	0.01±0.05
BHVO-1 (this study)	−0.14±0.03	−0.29±0.04	0.12±0.04	0.19±0.04
Lit. value	−0.16±0.02	−0.30±0.06	0.11±0.04	0.16±0.07
BCR-2 (this study)	−0.12±0.04	−0.25±0.05	0.08±0.03	0.15±0.05
Lit. value	−0.13±0.06	−0.21±0.10	0.08±0.04	0.13±0.04
AGV-2 (this study)	−0.09±0.05	−0.20±0.05	0.12±0.03	0.17±0.03
Lit. value	−0.06±0.04	−0.12±0.21	0.10±0.02	0.15±0.02
Diatom (this study)	0.65±0.04	1.26±0.05	--	--
Lit. value	0.64±0.03	1.24±0.07	--	--

Lit. value represents the average±2SD of the published literature values.
For Si isotopes: Armytage et al. (2011); Georg et al. (2006); Chakrabarti and Jacobsen (2010); Savage and Moynier (2013); Chen et al. (2017); Savage et al. (2010); Abraham et al. (2008); Sikdar and Rai (2017); van den Boorn et al. (2006); Zambardi and Poitrasson (2011); Ziegler et al. (2010); Savage et al. (2011); Fitoussi et al. (2009); Fitoussi and Bourdon (2012); Oelze et al. (2016); Reynolds et al. (2007); Georg et al. (2009).

For Fe isotopes: Dauphas et al. (2004); Dauphas et al. (2006); Dauphas et al. (2009); Wang et al. (2012); Wang et al. (2014a, b); Wang et al. (2015); Weyer et al. (2005); Weyer and Ionov (2007); Schoenberg and von Blanckenburg (2006); Rouxel et al. (2005); Poitrasson et al. (2004); Telus et al. (2012); Zhu et al. (2001); Sossi et al. (2016a).

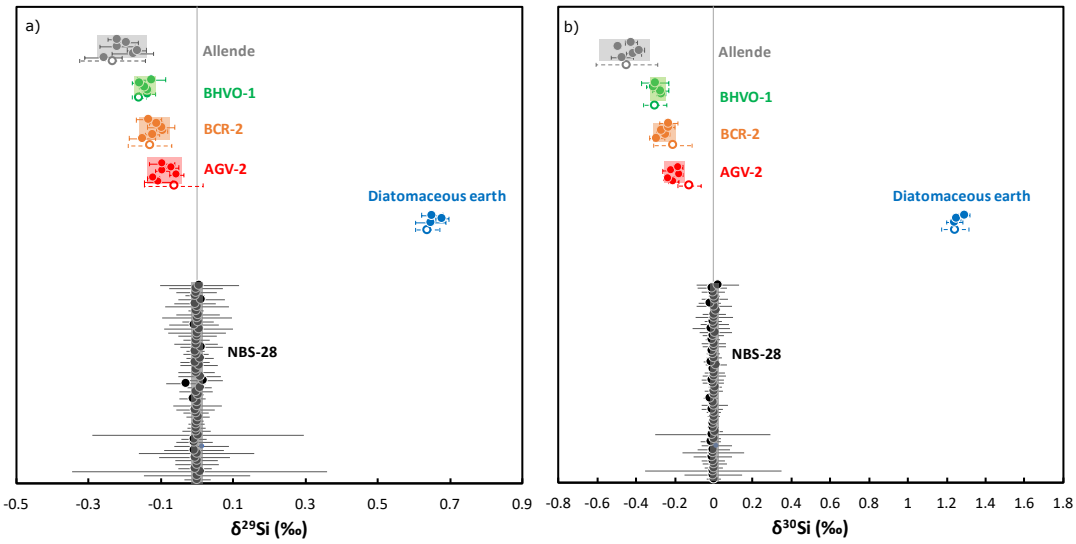

Figure 2.1. (a) $\delta^{29}Si$ and (b) $\delta^{30}Si$ of terrestrial standards and Allende CV3 chondrite. Filled symbols (average±2SE; n=6) are from this study while open symbols (average±2SD) are plotted from literature for comparison. Each solid symbol represents the average±2SE of six measurements (i.e., n=6). Colored boxes for each standard represent the average±2SD of the solid symbols (this study).

2.3.1 Accuracy and precision of Si isotope measurement

Silicon isotope data of the standards from this study comparable to those reported by other studies using differing analytical techniques (Figure 2.1 and Table 2.3). To ensure the accuracy and precision of our data, we have adopted several methods for measuring Si isotopes on the Thermo Neptune which we have discussed in the following text.

Known molecular and atomic mass interferences measured on ^{28}Si, ^{29}Si and ^{30}Si are as follows: $^{14}N_2^+$, $^{12}C^{16}O^+$, $^{56}Fe^{2+}$ on mass 28; $^{14}N^{15}N^+$, $^{12}C^{17}O^+$, $^{58}Fe^{2+}$, $^{58}Ni^{2+}$ on mass 29; and $^{14}N^{16}O^+$, $^{12}C^{18}O^+$ and $^{60}Ni^{2+}$ on mass 30. To preclude any effect of these interferences on the Si isotope ratios, we identified optimal "flatness" on the shoulder of the ^{29}Si peak for isotope measurements. In Fig. 2.2, we have illustrated

the Si isotope measurements of NBS-28 at a mass interval of 0.002 amu from the shoulder of the ^{29}Si peak. Based on repeated measurements, we identified that the "flattest" region to measure the Si isotopes is at a mass of ~0.007 amu from the beginning of the shoulder of the ^{29}Si peak.

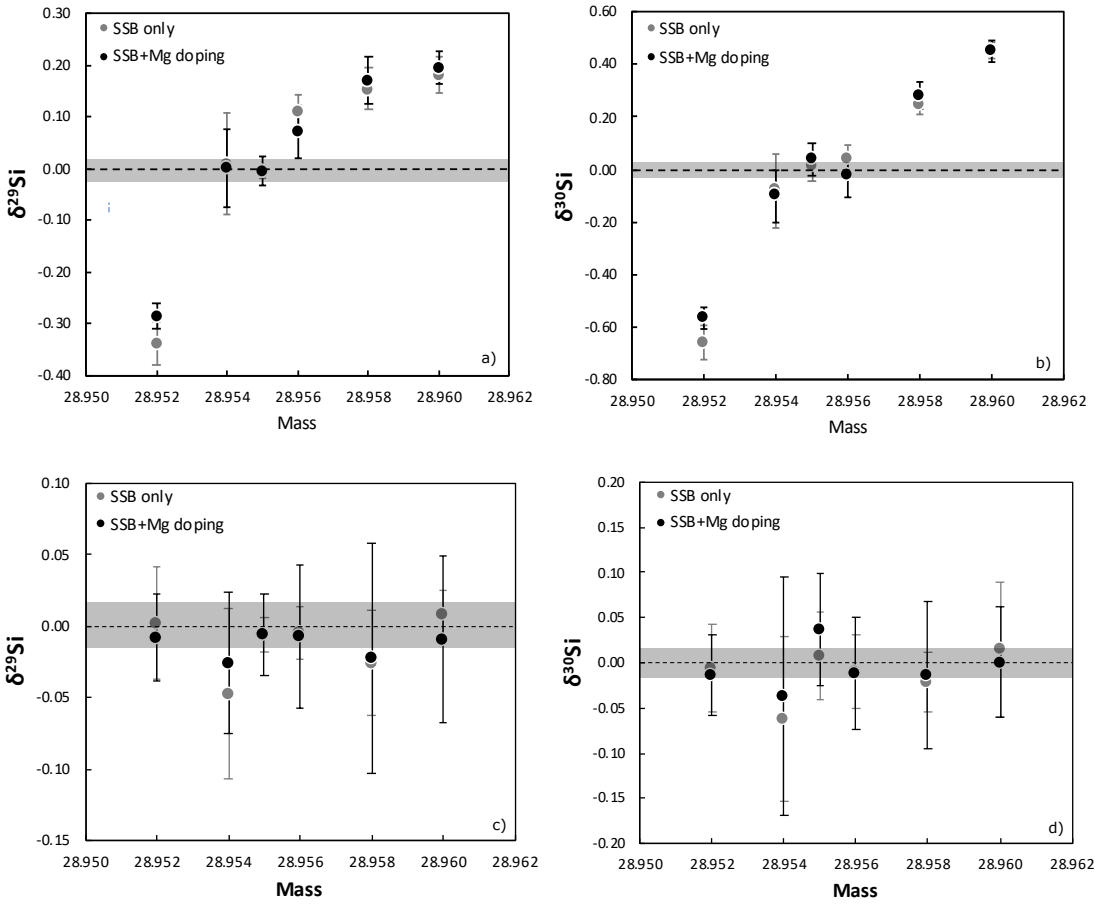

Figure 2.2. (a) δ^{29}Si of NBS-28 to determine the flattest portion of the Si peak. The bracketing standard for each data point is measured at a mass of 28.955 while the 'sample' is measured at masses ranging from 28.952 to 28.960. (b) corresponding δ^{30}Si of NBS-28. (c) δ^{29}Si of NBS-28 when the 'sample' and bracketing standard are both measured at the same mass, and (d) corresponding δ^{30}Si. All errors are 2SE. Grey circles are only sample standard bracketed against NBS-28 while black circles represent mass bias correction with Merck Mg and sample standard bracketing. Grey box represents the average±2SD of the external reproducibility of NBS-28 from Fig. 2.1.

The advantages of combined sample standard bracketing + Mg doping (SSB+Mg, hereafter) for correction of instrumental mass bias has been discussed in

prior studies (Zambardi and Poitrasson 2011; Oelze et al, 2016; Cardinal et al, 2003; Engstrom et al, 2006). Such studies have also discussed the effect of Si or Mg concentration, acid molarity matching, and anion contamination on the Si isotope measurements. We have adopted the SSB+Mg technique for all standards in this study. In an ideal situation, Si/Mg in both sample and standard should be identical, i.e., $\frac{(\mathbf{Si/Mg})_{\mathbf{sample}}}{(\mathbf{Si/Mg})_{\mathbf{standard}}} = 1$, for accurate and precise Si isotope data. In order to test the acceptable tolerance for deviation from the optimal value of 1, we prepared solutions of purified NBS-28 standard solutions with variable Si concentrations (1.44, 1.23, 1.11, 1, 0.90, 0.82, and 0.76 ppm respectively) and doped them with 0.5 ppm Merck Mg. These solutions with variable Si/Mg ratio were bracketed against the NBS-28 standard which had an Si/Mg ratio of 1ppm/0.5 ppm. We were thus able to measure variations in the solutions' Si concentration relative to NBS-28 while the Mg concentration remained constant at 0.5 ppm in both the sample and the standard. Since the concentration of Merck Mg in each solution remained constant, any deviation from the Si/Mg ratio of the sample is therefore, due to deviation of the Si concentration from 1 ppm. This is most relevant to our actual samples since the Merck Mg solution is added from a stock of known concentration (100 ppm in 0.05 N HCl) such that the concentration in the final solutions is 0.5 ppm.

Previous studies have shown that Si concentration of the sample could vary $\pm$50% compared to the bracketing standard without affecting the δ^{29}Si or δ^{30}Si values (Oelze et al., 2016). In Fig 2.3a, it is evident that the δ^{29}Si (SSB only) are similar within error irrespective of their Si concentrations compared to that of the bracketing standard. However, the δ^{29}Si (SSB + Mg) become distinct from each other and the δ^{29}Si (SSB only) for that sample as the $(Si/Mg)_{sample/standard}$ increases beyond 1. Similarly, in Fig. 3.3b, δ^{30}Si (SSB only) are mostly similar within $\pm$20% of Si concentration of the bracketing standard. On the other hand, the δ^{30}Si (SSB + Mg)

are more scattered and distinct from $\delta^{30}Si$ (SSB only) for a sample when $(Si/Mg)_{sample/standard}$ deviates from 1. This study provides evidence that although mass bias correction using Mg doping results in more precise Si isotope values with relatively small errors in the long run, it is essential to ensure that (Si/Mg) is within ±5%.

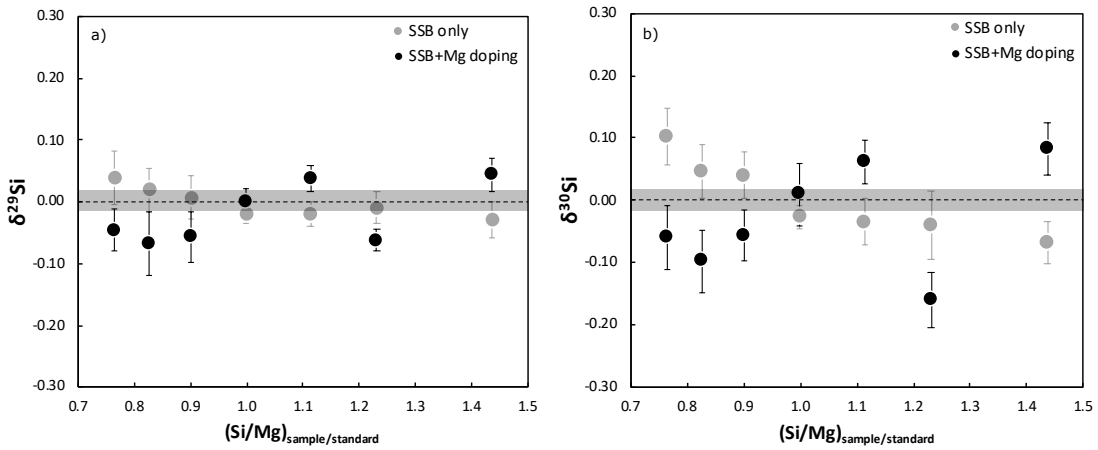

Figure 2.3. (a) $\delta^{29}Si$ and (b) $\delta^{30}Si$ of NBS-28 wherein the $\frac{(Si/Mg)_{sample}}{(Si/Mg)_{standard}}$ changes from 0.76 to 1.44, i.e., deviates from 1. All errors are 2SE. Grey box represents the average±2SD of the external reproducibility of NBS-28 from Fig. 2.1.

As already mentioned, alkali fusion of the sample with $NaOH.H_2O$ is the method of choice for sample dissolution to measure Si isotopes. For this reason, the sample solution contains a high concentration of inherited Na. It is extremely important to ensure the complete removal of Na from the Si for accurate measurements of Si isotopes. This is because Na could potentially form NaH^+ and interfere with Mg which in turn would affect the mass bias correction applied to the Si isotope ratios. Column chromatography using cation-exchange resin ensures removal of Na from the Si elute. To ascertain the effect of and tolerance level for Na in measuring Mg-corrected Si isotope ratios, we doped Si purified from Merck Certipur® Si standard solution with variable concentrations of Na (ranging from 50 ppb to 0.5 ppm) and constant Merck Mg (0.5 ppm) for mass bias correction. Results

of these experiments have been illustrated in Fig. 2.4. As the concentration of Na increases, the $\delta^{29}Si$ and $\delta^{30}Si$ values deviate from the expected value of ~0 and suggests that presence of residual Na in the final solution will result in erroneous $\delta^{29}Si$ and $\delta^{30}Si$ values. Although this is true for both the SSB only and SSB+Mg doped isotopic values, the SSB+Mg doped value is accurate within error up to 100 ppb Na while the SSB only values are less tolerant to the presence of Na. Thus, extreme care must be taken to ensure that the purified Si solutions are entirely free of Na especially when not employing Mg doping for mass bias corrections.

2.3.2 Accuracy and precision of Fe isotope measurement

The Fe isotope data of the standards from this study are consistent with those reported in literature (Fig. 2.5). As with our Si isotope measurements, we have adopted several methods and protocols to ensure the accuracy and precision of our Fe isotope data.

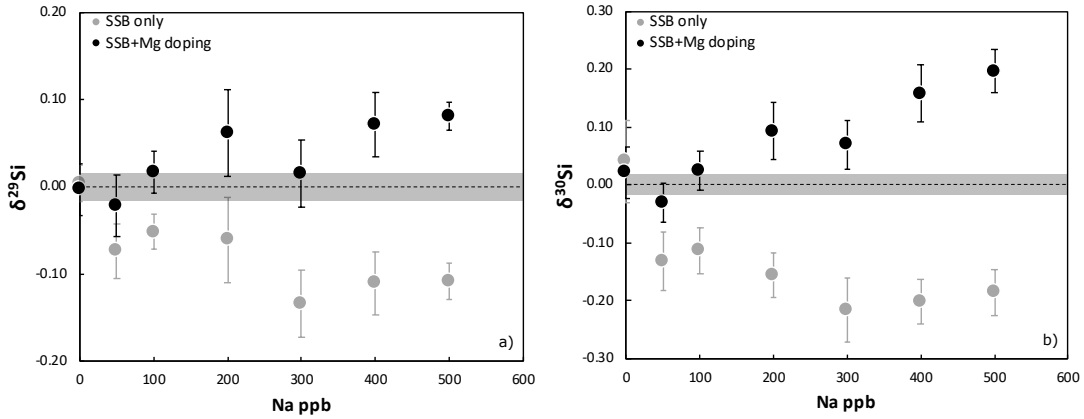

Figure 2.4. $\delta^{29}Si$ and $\delta^{30}Si$ values of Merck Certipur® Si standard solution doped with variable concentrations of Na. Grey box represents the average±2SD of the external reproducibility of NBS-28 from Fig. 2.1.

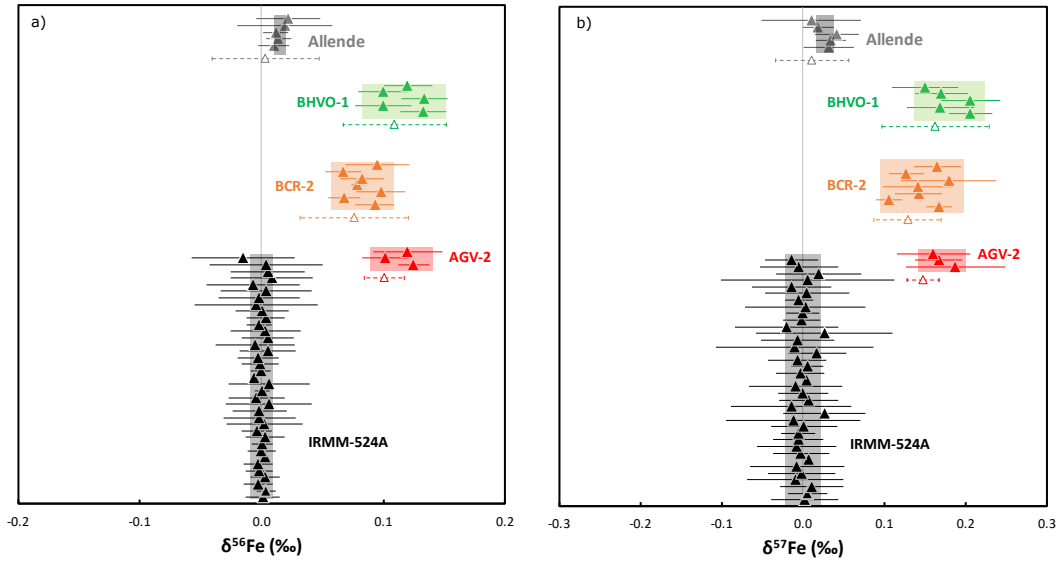

Figure 2.5. (a) $\delta^{56}Fe$ and (b) $\delta^{57}Fe$ of terrestrial standards and Allende CV3 chondrite. Filled symbols (average±2SE; n=6) are from this study while open symbols (average±2SD) are plotted from literature for comparison. Each solid symbol represents the average±2SE of six measurements (i.e., n=6). Colored box for each standard represents the average±2SD of the solid symbols (this study).

Molecular interferences on ^{54}Fe, ^{56}Fe and ^{57}Fe are $^{40}Ar^{14}N^{+}$, $^{40}Ar^{16}O^{+}$, and $^{40}Ar^{16}O^{1}H^{+}$ respectively. To preclude the effect of these interferences on the Fe isotopes, we identified "the flatness" on the shoulder of the ^{56}Fe peak for isotope measurements. In Fig. 2.6, we have illustrated the Fe isotope measurements of IRMM-524A at a mass interval of 0.002 from the shoulder of the ^{56}Fe peak. Based on repeated measurements, we identified that the "flattest" region to measure the Fe isotopes was at a mass of ~0.007 amu from the beginning of the shoulder. Throughout this study, Fe isotopes have been measured at a mass at least ~0.007 from the ^{56}Fe shoulder.

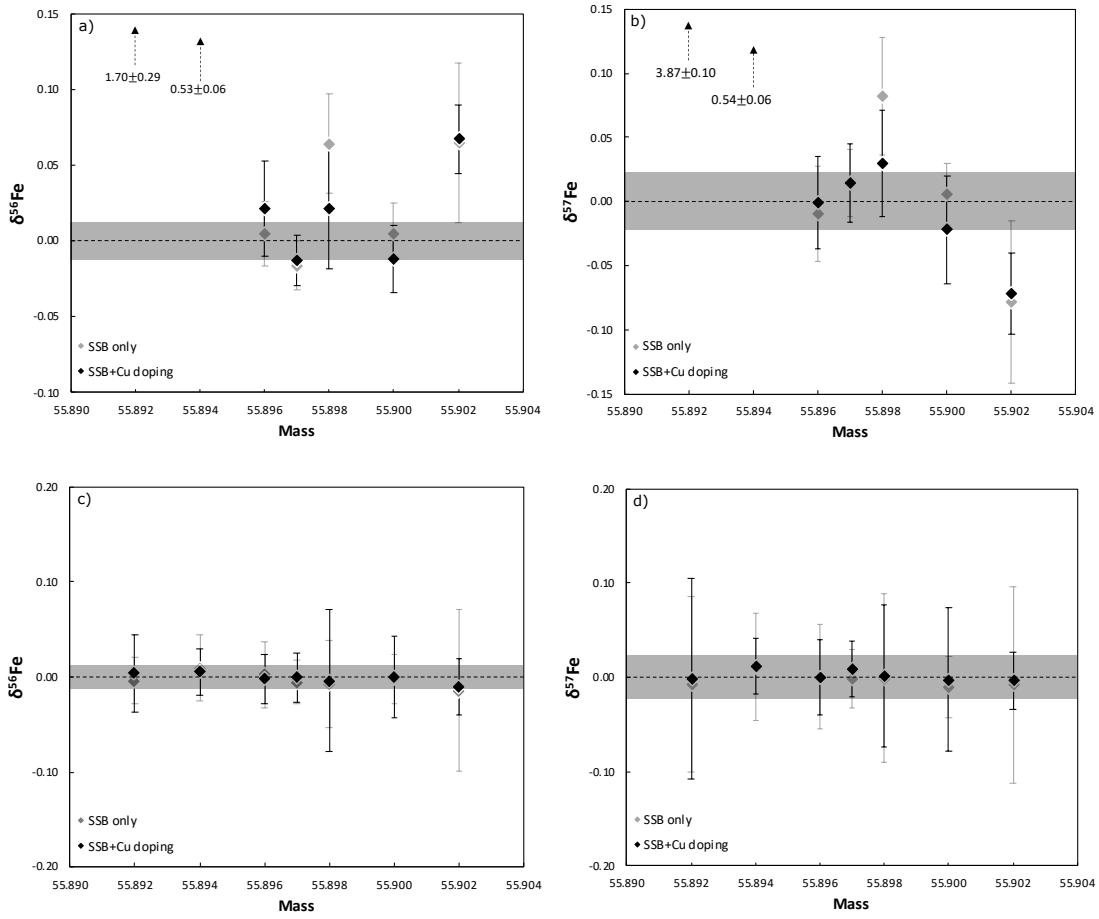

Figure 2.6. (a) δ^{56}Fe of IRMM-524A to determine the flattest portion of the Fe peak. The bracketing standard for each data point is measured at a mass of 55.897 while the 'sample' is measured at masses ranging from 55.892 to 55.902. (b) corresponding δ^{57}fe of IRMM-524A. (c) δ^{56}Fe of IRMM-524A when the 'sample' and bracketing standard are both measured at the same mass, and (d) corresponding δ^{57}Fe. All errors are 2SE. Grey diamonds are only sample standard bracketed against IRMM-524A while black diamonds represent mass bias correction with NIST Cu and sample standard bracketing. Grey box represents the average±2SD of the external reproducibility of IRMM-524A from Fig. 2.5.

Since purified Fe solutions are doped with Cu for mass bias corrections, we have tested the permissible departure from the $\frac{(\mathbf{Fe/Cu})_{\mathbf{sample}}}{(\mathbf{Fe/Cu})_{\mathbf{standard}}} = 1$ to ensure the most precise and accurate Fe isotope data. For this, we followed a protocol similar to that for Mg doped Si. The concentration of the IRMM-524A bracketing standard is 0.5 ppm Fe doped with 0.5 ppm NIST Cu solution. Keeping the Cu concentration constant at 0.5 ppm, we prepared sample solutions of IRMM-524A with Fe

concentrations of 0.3, 0.4, 0.45, 0.5, 0.55, 0.6, 0.7 ppm such that the $(Fe/Cu)_{sample/standard}$ was 0.6, 0.8, 0.9, 1, 1.1, 1.2, 1.4, i.e., a range of ±40% from the Fe/Cu ratio in the bracketing standard. Results are illustrated in Fig 2.7. For both $\delta^{56}Fe$ and $\delta^{57}Fe$, the most accurate and precise values are reported for $\frac{(\mathbf{Fe/Cu})_{\mathbf{sample}}}{(\mathbf{Fe/Cu})_{\mathbf{standard}}}$ =1 such that the SSB only and SSB+Cu are almost identical. For $\frac{(\mathbf{Fe/Cu})_{\mathbf{sample}}}{(\mathbf{Fe/Cu})_{\mathbf{standard}}}$ between 0.9 to 1.4, SSB only and SSB+Cu doped Fe isotope values have larger errors and are similar to each other and the often the actual value denoted by the grey bar. The SSB only and SSB+Cu doped Fe isotope values are distinct for $\frac{(\mathbf{Fe/Cu})_{\mathbf{sample}}}{(\mathbf{Fe/Cu})_{\mathbf{standard}}}$ < 0.9. This study shows that departure from the $\frac{(\mathbf{Fe/Cu})_{\mathbf{sample}}}{(\mathbf{Fe/Cu})_{\mathbf{standard}}}$ = 1 results in increase in errors and non-similarity between the SSB only and SSB+Cu doped Fe isotope values and therefore, the $(Fe/Cu)_{sample}$ should be restricted to within ±10% of the $(Fe/Cu)_{standard}$.

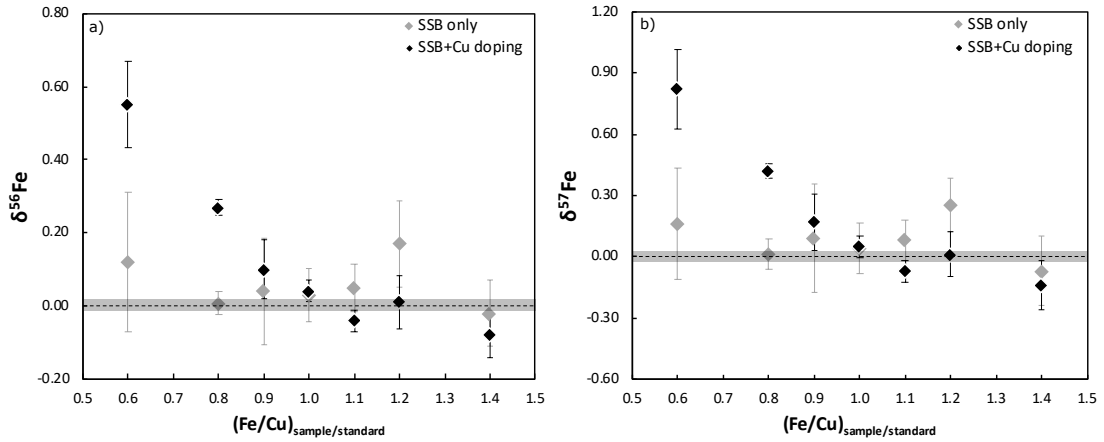

Figure 2.7. Figure 7: (a) $\delta^{56}Fe$ and (b) $\delta^{57}Fe$ of IRMM-524A wherein the $\frac{(\mathbf{Fe/Cu})_{\mathbf{sample}}}{(\mathbf{Fe/Cu})_{\mathbf{standard}}}$ changes from 0.6 to 1.4, i.e., deviates from 1. All errors are 2SE. Grey box represents the average±2SD of the external reproducibility of IRMM-524A from Fig. 2.5.

2.4 Conclusion

Here, we have described a new method to simultaneously separate Si and Fe from a single aliquot of sample via column chromatography followed by high precision measurement of Si and Fe isotopes. The robustness of the method is established by determining the isotope composition of four terrestrial standards (BHVO-1, BCR-2, AGV-2, and diatomaceous earth) and CV3 Allende meteorite. All isotope data are reproducible and comparable to published values in the literature. This new method precludes possible heterogeneity at the scale of sampling as well as reduces the amount of sample required for such isotopic analyses. This new method is applicable to a wide variety of samples in both the terrestrial and extra-terrestrial realm and can help constrain processes involving the fractionation of Fe and Si isotopes.

CHAPTER 3

CORRELATED IRON ISOTOPES AND SILICON CONTENTS IN AUBRITE METALS REVEAL STRUCTURE OF THEIR ASTEROIDAL PARENT BODY

Abstract

Iron isotopes record the physical parameters, such as temperature and redox conditions, during differentiation processes on rocky bodies. Here we report the results of a correlated investigation of iron isotope compositions and silicon contents of silicon-bearing metal grains from several aubritic meteorites. Based on their Fe isotopic and elemental Si compositions and thermal modelling, we show that these aubrite metals equilibrated with silicates at temperatures ranging from ~1430 K to ~1640 K and likely sampled different depths within their asteroidal parent body. The highest temperature in this range corresponds to their equilibration at a minimum depth of up to ~35 km from the surface of the aubrite parent body, followed by brecciation and excavation by impacts within the first ~4 Myr of Solar System history.

3.1 Introduction

Metal segregation in accreting rocky bodies occurred very early on in the history of the Solar System, in some cases within 1 Myr after the formation of calcium-aluminum-rich inclusions (CAIs) which are the oldest known solids to have formed in the solar nebula and are, therefore, thought to represent the time of Solar System formation[1-3]. While magmatic iron meteorites sample cores of differentiated asteroidal bodies and provide insights into the processes and timescales of core formation[3-5], achondritic meteorites are key for providing complementary understanding of silicate differentiation and crust formation on such bodies[6]. In particular, the stable isotopic compositions of differentiated meteorites and their

components have added to our understanding of the physical parameters, such as temperature, pressure, and redox conditions relevant to differentiation processes on planetesimals in the early Solar System[7,8].

Iron is the most abundant multi-valent element in planetary reservoirs. Its abundance and variable oxidation states (i.e., Fe^0 in iron metal, Fe^{2+} in silicates/sulfides, and Fe^{3+} in silicates/oxides) have allowed it to be used in studies aimed at understanding the effects of metal-silicate equilibration on stable iron isotope compositions[9-17]. During equilibration of metal with silicates, the iron isotope composition (expressed as $\delta^{56}Fe$ which is the deviation in parts per thousand of the $^{56}Fe/^{54}Fe$ ratio of the sample relative to the IRMM-014 bracketing standard) of iron metal is expected to be enriched in the heavier isotopes of iron compared to co-existing silicates. This expectation stems from crystal chemical principles involving an interplay of bond strength, bond length, bond stiffness, co-ordination number, valence and associated vibrational frequencies that govern the occupation of crystallographic sites by heavy or light isotopes[18,19]. A short and stiff bond is expected to accommodate the heavier isotopes of a given element. The presence of delocalized electrons in iron metal facilitates shorter and stiffer metallic bonds, compared to the Fe-O bonds in silicates, which favors the enrichment of heavier iron isotopes in the iron metal[19]. This is consistent with the observation that metals from pallasites[9], enstatite chondrites[13], aubrites[13,17], iron meteorites[20], and ordinary chondrites[21-23] are characterized by heavier iron isotope composition compared to co-existing silicates and sulfides. This further leads to the expectation, supported by some recent experimental studies[14-16], that the metallic core of a differentiated body should have a heavier iron isotopic composition compared to its silicate mantle.

However, there is no detectable fractionation of iron isotopes between co-existing metal and silicate in the run products from at least some piston cylinder experiments[11,12]. Recently, the effect of Si content of metal on $\Delta^{56}Fe_{metal\text{-}silicate}$ (i.e.,

$\delta^{56}Fe_{metal}$ - $\delta^{56}Fe_{silicate}$) was studied[16]. This study suggested that a combined substitution of Ni, S, and Si in the iron metal would lead to a heavier iron isotopic composition of the metal compared to the silicate. In contrast, based on Nuclear Resonant inelastic X-Ray spectroscopic (NRIXS) measurements of mean force constants of Fe bonds in basaltic glass and metal alloys (such as Fe-Ni, Fe-Si and Fe-S), no significant fractionation between silicate and metal at pressures of up to 206 GPa was found[24]. Thus far, there have been no studies that have investigated the potential correlation of Si content with iron isotope fractionation in natural metallic samples that record metal-silicate equilibration.

Aubrites are pyroxenitic achondrites that are known to contain Si-bearing Fe-Ni metal. The pattern of siderophile element abundances in these Si-bearing aubrite metals reflects their residual nature, i.e., they represent metal that was trapped in the silicate-sulfide magma during partial melting and inefficient metal segregation (i.e., core formation) on the aubrite parent body[25]. Therefore, aubrites provide the opportunity to study the correlation between Si content and $\delta^{56}Fe$ of these metals that are thought to have equilibrated with the surrounding silicates. Aubrites are dominated by almost FeO-free enstatite, with lesser amounts of diopside and forsterite, troilite, Si-bearing Fe-Ni metal, and a variety of accessory minerals that reflect the highly reducing conditions during their formation[26]. Aubrites are thought to represent the differentiated products of enstatite chondrite-like starting materials[27-29] and are postulated to have originated on at least two distinct parent bodies: the main aubrite parent body, from which most aubrites are thought to have originated, and the Shallowater parent body[26,30]. Most aubrites from the main aubrite body are fragmental or regolith breccias, while Shallowater is unbrecciated[26]. The unique unbrecciated, metal-rich Mount Egerton aubrite has been considered to either represent the core-mantle boundary of the main aubrite parent body[31] or have originated on a distinct parent body[32].

The Si content of Fe-metal is strongly temperature-dependent[33,34], and has been used to determine the equilibration temperatures in enstatite meteorites[13,17,35,36]. However, these studies used a single Si content for all metals within a given aubrite to derive a metal-silicate equilibration temperature for that sample[13,17,36]. For example, equilibration temperatures were calculated to be ~1060 K for 2 mol.% Si in metal for Shallowater[13], ~1200 K[36] for 4.5 mol.% Si in metal or ~1460 K[17] for 2 wt.% Si in metal for Mount Egerton, and ~1130 K[36] for 2.1 mol.% Si in metal or ~1415 K[17] for 0.91 wt.% Si in metal for Norton County. However, the Si contents of different metal grains within a given aubrite have been shown to vary significantly[25,37]. This variability may indicate that individual metal grains equilibrated with silicates over a range of temperatures and/or redox conditions which may additionally be reflected in their iron isotope compositions. Here, we address the question of the origin of metal grains in the aubrites based on their major element composition, with a focus on Si, coupled with their δ^{56}Fe. Since the elemental composition of metal, especially Si content, and δ^{56}Fe are likely to be functions of temperature and redox conditions during metal-silicate equilibration, a correlation, if any, would provide insights into the physical conditions governing the formation of aubrites. Furthermore, we have modeled the thermal evolution of the aubrite parent body which allows us to infer the physical setting of the metal grains in the aubrites studied here and has implications for the structure of their parent body.

3.2 Results

3.2.1 Elemental and iron isotope compositions of aubrite metals

We measured the elemental abundances (Fe, Ni, Co, P, and Si) and Fe isotope compositions of ten metal grains from Norton County, four from Mount Egerton, one from Bishopville, and two from Shallowater. These aubrite metals have Si contents ranging between 0.1 to 2.12 wt.% and δ^{56}Fe values ranging from 0.015±0.018‰ to

0.149±0.026‰ (Table 3.1). Moreover, the $\delta^{56}Fe$ values of these metal grains are inversely correlated with their Si contents (Fig. 3.1). There appears to be no strong correlation between the abundances of other elements (Fe, Ni, Co, P) and $\delta^{56}Fe$ for the metal grains studied here (Supplementary Fig. A3.3). There are two previous studies[13,17] that report the iron isotope compositions of aubrite metals. Unlike our study, neither of these studies[13,17] analyzed the Si content in the aubrite metal. In one of these studies[13], two magnetic fractions (presumably enriched in metal) separated from Shallowater have $\delta^{56}Fe$ of 0.039 ± 0.044‰ and 0.075 ± 0.059‰, and Fe contents of 46.4 wt.% and 30.1 wt.%, respectively. These magnetic fractions have lower $\delta^{56}Fe$ values and Fe contents than the aubrite metal grains analyzed here (Table 3.1), suggesting that phase(s) with lower $\delta^{56}Fe$ and Fe content than metallic Fe-Ni contributed to these magnetic fractions[13]. Four metal samples from Norton County with $\delta^{56}Fe_{avg.}$ = 0.025± 0.012‰ (2SE) and two metal samples from Mount Egerton with $\delta^{56}Fe_{avg.}$ = 0.002± 0.017‰ (2SE) were reported in the other previous study[17]. These iron isotope compositions are similar to some of those from Norton County (NC8–10) and Mount Egerton (ME1–4) reported here, but distinct from those of other aubrite metals reported in our study (Table 3.1).

3.2.2 Equilibration temperatures and oxygen fugacities

Based on the elemental compositions of the metal grains and silicates from each of the aubrites studied here, we calculated the metal-silicate equilibration temperatures and fO_2 values (see Methods below for the equations and parameters used for these calculations). The calculated equilibration temperatures (Table 3.1, Fig. 3.2a and 3.2b) based on partitioning of Si and Fe between metal and silicate range from ~1432 K to ~1635 K. The four metal grains from Mount Egerton (ME1–4) record the highest equilibration temperatures that are the same within the errors (Table 3.1). The metals from Shallowater (SW1 and SW3) record lower equilibration

temperatures that are also, within the errors, similar to each other (Table 3.1). However, the 10 metal grains from Norton County record a temperature range of about ~130 K, from 1493 K in NC4 to 1626 K in NC9. Calculated fO_2 values (Table 3.1, Fig. 3.2c and 3.2d) are similar within the errors, with an average value of −5.5±0.4 (2SD) log units relative to the iron-wüstite buffer (ΔIW); these values are similar to those previously reported for aubrites[38].

Table 3.1. Elemental and Fe isotopic compositions of the metal grains from the Norton County (NC), Mount Egerton (ME), Bishopville (BSP), and Shallowater (SW) aubrites. Elemental concentrations are in wt.% and are obtained by electron probe microanalysis (EPMA). Numbers within parentheses indicate number of EPMA data points averaged to obtain the elemental abundances of Fe, Ni, Co, P, and Si in each nodule. The $\Delta^{56}Fe_{\text{metal-silicate}}$ values are calculated using the $\delta^{56}Fe_{metal}$ from this study and published values[13,17] of $\delta^{56}Fe_{silicate}$ for that particular meteorite; $\Delta^{57}Fe_{\text{metal-silicate}}$ is calculated similarly (note that $\delta^{56}Fe_{silicate}$ for BSP does not exist, so $\Delta^{56}Fe$ and $\Delta^{57}Fe$ for this aubrite are not calculated). Calculated equilibration temperature (T in K) and fO_2 (ΔIW) for each of these aubrite metals are also shown.

Samples	Size* (mm)	Fe	Ni	Co	P	Si	$\delta^{56}Fe\pm2SE$	$\delta^{57}Fe\pm2SE$	n	$\Delta^{56}Fe\pm2SE$	$\Delta^{57}Fe\pm2SE$	T(K)	fO_2 (ΔIW)
NC2 (100)	2	92.14	7.14	0.42	0.04	0.81	0.115±0.010	0.157±0.027	6	0.151±0.018	0.215±0.033	1559±28	-5.5
NC3 (100)	2	93.26	6.02	0.47	0.07	0.38	0.137±0.024	0.197±0.039	6	0.173±0.020	0.255±0.043	1510±27	-5.5
NC4 (100)	3	94.30	5.64	0.36	0.10	0.29	0.149±0.026	0.292±0.024	12	0.185±0.030	0.350±0.031	1493±26	-5.5
NC6 (100)	3	94.42	5.85	0.38	0.09	0.32	0.143±0.029	0.222±0.035	6	0.179±0.033	0.280±0.040	1499±26	-5.5
NC7 (200)	8	91.93	5.81	0.32	0.10	1.67	0.057±0.012	0.082±0.023	12	0.093±0.019	0.140±0.024	1608±30	-5.5
NC8 (200)	21	91.22	6.51	0.28	0.08	1.39	0.048±0.016	0.066±0.018	12	0.084±0.022	0.124±0.028	1596±30	-5.5
NC9 (200)	14	91.38	6.33	0.33	0.06	2.12	0.036±0.015	0.068±0.027	13	0.072±0.021	0.126±0.033	1626±31	-5.5
NC10 (200)	7	90.56	6.67	0.35	0.05	1.75	0.038±0.014	0.086±0.023	12	0.074±0.021	0.144±0.028	1613±30	-5.5
NC11 (200)	15	91.16	7.11	0.32	0.09	0.64	0.127±0.018	0.248±0.062	12	0.163±0.023	0.306±0.065	1545±28	-5.5
NC12 (200)	18	89.91	8.07	0.30	0.09	0.73	0.105±0.014	0.218±0.037	12	0.141±0.021	0.276±0.042	1555±28	-5.5
ME1 (200)	15	91.55	5.52	0.36	0.07	2.00	0.026±0.010	0.067±0.025	6	0.064±0.012	0.119±0.028	1633±31	-5.4
ME2 (200)	11	90.71	6.94	0.34	0.07	2.00	0.020±0.014	0.061±0.030	6	0.058±0.016	0.113±0.032	1634±31	-5.4
ME3 (200)	12	91.07	6.69	0.34	0.08	2.01	0.025±0.015	0.057±0.023	6	0.063±0.017	0.109±0.020	1633±31	-5.4
ME4 (200)	10	91.51	6.15	0.34	0.09	2.07	0.015±0.018	0.062±0.028	6	0.053±0.019	0.114±0.030	1635±31	-5.4
BSP3 (40)	1	93.44	6.03	0.35	0.06	0.10	0.130±0.015	0.170±0.036	6	–	–	1432±24	-5.5
SW1 (40)	1	93.31	5.24	0.37	0.36	0.89	0.115±0.010	0.154±0.023	6	0.094±0.060	0.225±0.109	1541±28	-5.7
SW3 (40)	1	88.98	8.61	0.30	0.24	0.86	0.104±0.010	0.137±0.023	6	0.083±0.060	0.137±0.109	1544±28	-5.7

*Size refers to the longest axis (in most cases, diameter) of the metal grain in mm

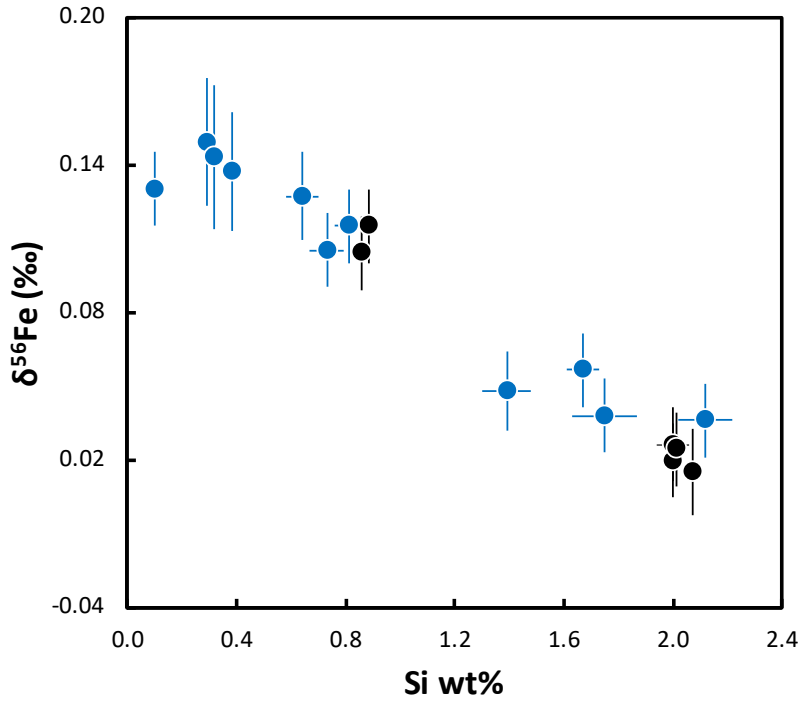

Figure 3.1. δ^{56}Fe versus Si content of aubrite metals. Blue symbols represent metals from brecciated aubrites (Norton County and Bishopville) and black symbols show metals from non-brecciated aubrites (Shallowater and Mount Egerton). An inverse correlation between the δ^{56}Fe and Si content of aubrite metals is observed. All errors are 2SE.

3.2.3 Modeling the thermal evolution of the aubrite parent body

Heating and melting processes on early-formed planetesimals are thought to be driven largely by the decay of the short-lived radionuclide ^{26}Al[39]. The evolution of the interior temperatures of parent bodies can be calculated using the analytical solution to the partial differential equation for heat conduction based on estimates of the ^{26}Al content at the time of accretion assuming a constant heat capacity[41,42] (see Methods below for equations and parameters used for these calculations). Since we are only interested in a first-order relationship between the accretion timescales and evolution of interior temperatures, we have assumed constant heat capacity (C_P), thermal conductivity (K), density (ρ), and other appropriate parameters for the aubrite parent body (Supplementary Table A2.3), to calculate temperatures (T in Kelvin) as a function of distance from the center (r in km) of the parent body at

different times. For these calculations, we assume that the maximum accretion time for the aubrite parent body was ~1.5 Myr after CAI formation[40]; as such, for illustrative purposes, we have performed the calculations described above for accretion times of 1.0, 1.3, and 1.5 Myr after CAI formation. Figure 2.3 shows that a temperature profile relevant to the range of metal-silicate equilibration temperatures recorded by the aubrite metals studied here can be attained within 4.3 Myr after CAI formation. Moreover, the highest recorded equilibration temperature is achieved at a minimum depth of up to ~35 km from the surface of the parent body (at the maximum estimated accretion time of ~1.5 Myr after CAI formation).

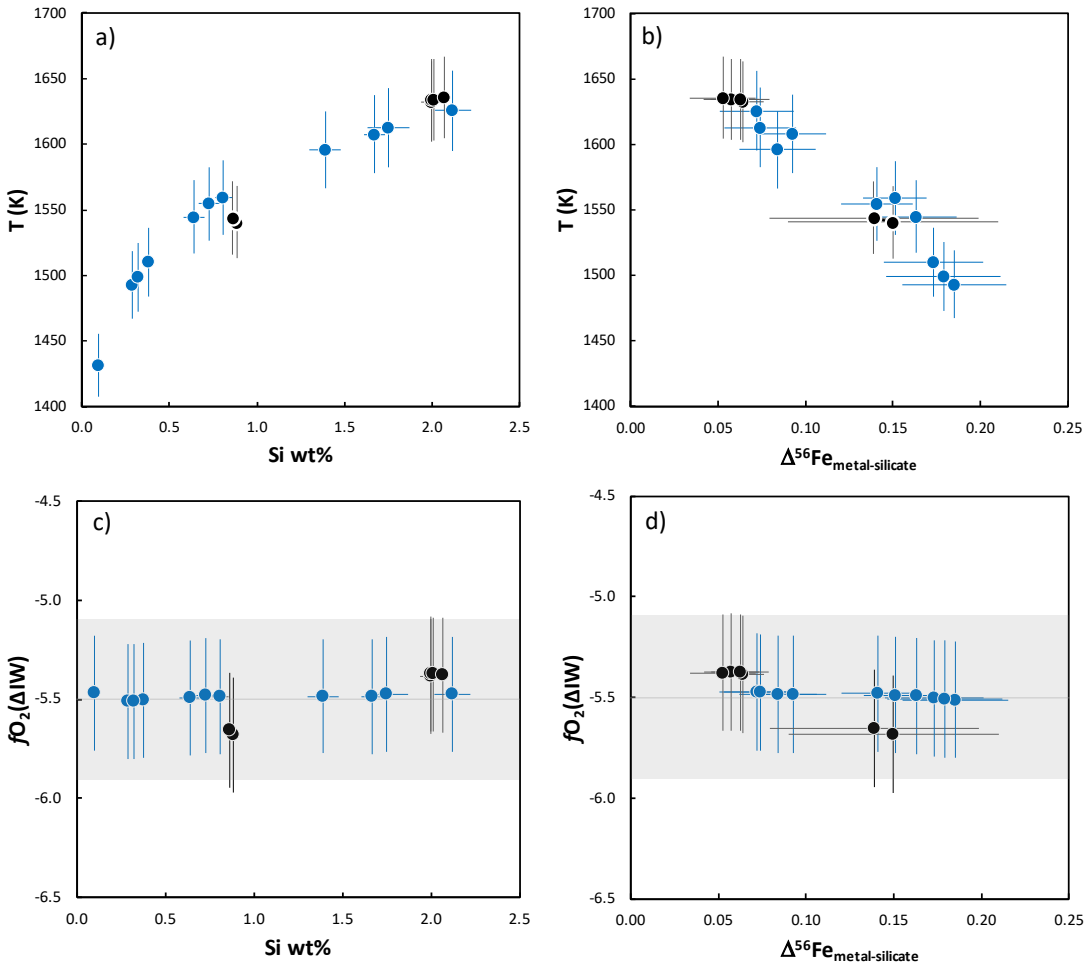

Figure 3.2. Plots of (a) calculated metal-silicate equilibration temperature (T in Kelvin) vs. measured Si content (wt.%); (b) calculated metal-silicate equilibration temperature (T in Kelvin) vs. $\Delta^{56}Fe_{metal\text{-}silicate}$; (c) calculated fO_2 (ΔIW) vs. Si content (wt.%); and (d) calculated fO_2 (ΔIW) vs. $\Delta^{56}Fe_{metal\text{-}silicate}$ for aubrite metals. The

horizontal grey line and box in 2c and 2d represent the average±2SD (i.e.,−5.5±0.4) of the calculated fO_2 for the aubrite metals. The $\Delta^{56}Fe_{metal\text{-}silicate}$ ($\delta^{56}Fe_{metal} - \delta^{56}Fe_{silicate}$) values are calculated using $\delta^{56}Fe_{metal}$ from this study and $\delta^{56}Fe_{silicate}$ for Norton County, Mount Egerton, and Shallowater from previous studies[13,17]; the Bishopville data point is not shown in (b) and (d) because the $\delta^{56}Fe_{silicate}$ value for this sample has not been reported and the $\Delta^{56}Fe_{metal\text{-}silicate}$ value could not be calculated. The symbols are same as in Fig. 3.1.

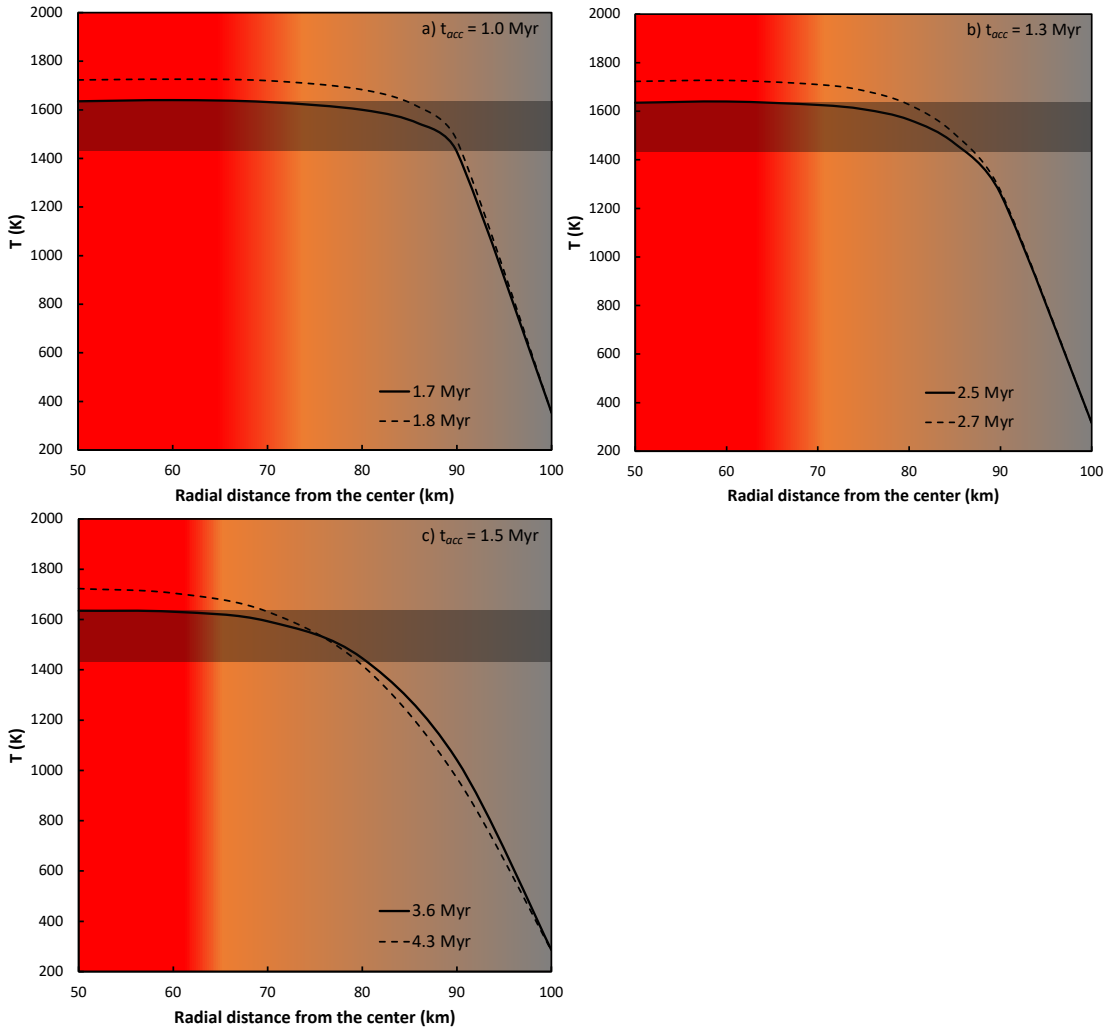

Figure 3.3. The calculated temperature (T in Kelvin) versus radial distance (r in km) from the center of the 200 km diameter aubrite parent body (AuPB) at 1 AU from the Sun at different times (shown by solid and dashed curves) assuming that the time of accretion was (a) 1.0 Myr; (b) 1.3 Myr; and (c) 1.5 Myr after CAI formation. The parameters used for these calculations are listed in Supplementary Table A3.3 and the detailed procedure for the calculations are described in Section 3.4.4. Warmer colors represent higher temperatures with increasing depth from the surface of the AuPB. The black solid curve corresponds to the thermal profile with interior T of 1635 K (i.e., the highest estimated metal-silicate equilibration temperature recorded in the aubrite metals in this study). The black dashed curve represents the thermal gradient with interior T of 1723 K beyond which >50% silicate melting would lead to

obliteration of the thermal gradient in the AuPB (see text for details). Horizontal gray bar illustrates the range of metal-silicate equilibration temperatures (1432−1635 K) estimated for the aubrite metals in this study. The thermal gradient within the AuPB inferred from the metal-silicate equilibration temperatures recorded by the aubrite metals in this study is attained by (a) 1.7−1.8 Myr (for t_{acc}= 1.0 Myr), (b) 2.5−2.7 Myr (for t_{acc}= 1.3 Myr), and (c) 3.6−4.3 Myr (for t_{acc}= 1.5 Myr) after CAI formation**.** Therefore, the aubrite parent body likely acquired this thermal gradient well within 4.3 Myr after CAI formation (assuming its accretion occurred within ~1.5 Myr after CAI formation[40]). Note that the required minimum depth of excavation increases with increasing accretion time, with an excavation depth of at least ~35 km for an accretion time of ~1.5 Myr after CAI formation.

3.3 Discussion

The degree of mass-dependent fractionation of iron isotopes between metal and silicates is expected to decrease with increasing temperature of equilibration[18,19,43,44]. In addition, metal-silicate equilibration experiments demonstrate increased partitioning of Si in metal with temperature[33,34]. We hypothesize that the anti-correlation between Si content and δ^{56}Fe of aubrite metals (Fig. 3.1) can be explained in terms of their dependence on the metal-silicate equilibration temperatures. The equilibration between metal and silicates in aubrites can be expressed by the following reaction:

$$SiO_2 + 2Fe_{metal} = 2FeO + Si_{metal} \quad (3.1)$$

Previous estimates[13,36] of metal-silicate equilibration temperatures for aubrites were considered to be too low[17] given the temperatures required for the onset of melting for an enstatite chondrite composition[45,46]. Here, we calculate the metal-silicate equilibration temperatures based on the solubility of Si in iron metal (Table 1; Fig 3.2a and 3.2b) using an equation utilized previously[34].

Prior studies have discussed the control of fO_2 on mass-dependent fractionation of iron isotopes of various planetary materials[47-49]. In general, an ion with a higher valence is preferentially enriched in the heavier isotopes of that element[18,19]. A linear positive correlation between the Fe force constant and $\sum Fe^{3+}/Fe_{total}$ in synthetic silicate was observed[49]. Force constants are measures of

bond strengths and thus, a higher force constant translates to stronger bonds which in turn facilitates the enrichment of heavier isotopes. Therefore, a higher force constant for a higher $\sum Fe^{3+}/Fe_{total}$ predicts that Fe^{3+}-bearing phases are more enriched in the heavier Fe isotopes compared to Fe^{2+}-bearing phases. It was, however, suggested that only 1/3 of the Fe isotope fractionation between mid-oceanic ridge basalts and terrestrial mantle could be explained due to the change in oxidation state of Fe in basaltic melt, while a change in the structural environment of the silicate melt was invoked to explain the remaining offset[49]. Given their highly reduced nature (and the resulting absence of Fe^{3+}) of the aubrites, the increasingly lighter $\delta^{56}Fe$ values of metals correspond to smaller $\Delta^{56}Fe_{metal\text{-}silicate}$ values are likely a function of the change in Fe-bonding environment with increasing temperature and Si content. For ordinary chondrites, the $\delta^{56}Fe$ of metal increases from H (most reduced of OCs) through L to LL (most oxidized of OCs), although a temperature dependence related to petrographic grade is also observed[21,22]. Studies have also shown the increased partitioning of Si in metal with decreasing oxygen fugacity[34,45,46]. To assess the effect of redox on the iron isotope fractionation recorded in the aubrite metals, we also calculated fO_2 values for aubrites. The aubrite metals show a narrow range of fO_2 from -5.1 to -5.4 log units relative to the iron-wüstite buffer (ΔIW) (Table 3.1); these values are similar to those previously reported for aubrites[38] suggesting that the primary control on the Si content and the iron isotopic composition of metal in the aubrites is the metal-silicate equilibration temperature. We conclude that the observed anti-correlation between Si content and $\delta^{56}Fe$ in the Si-bearing metals from the aubrites studied here (Fig. 3.1) is consistent with these metals recording a range of metal-silicate equilibration temperatures (Figs. 3.2a and 3.2b), with little variation in the redox conditions (Figs. 3.2c and 3.2d).

The incorporation of Si along with other elements such as Ni and S in metal has the potential to alter the bonding environment of Fe, such as bond strength, length, and stiffness. However, a series of piston cylinder experiments at 1850º C and 1 GPa were unable to detect any resolvable metal-silicate Fe isotope fractionation with varying Si content in the metal, even though a change in bond length with incorporation of Si in iron metal was invoked[16]. The radial distribution function (RDF) or probability of finding another atom in a spherical shell of radius *r* in iron alloys with 17 wt.% Si between 0-3 GPa and 1570–2040 K reveals that the packing structure around Fe does not change significantly from that of pure Fe-liquids[50]. Although the first neighbor interatomic distance (r_1) decreases slightly from 2.56–2.57 Å in pure Fe melt to 2.54–2.53 Å in the alloy and is invariant with respect to pressure (P) or temperature (T), large structural changes in Fe-Si alloys compared to pure Fe-metal are not predicted[50]. Therefore, it seems unlikely that greater incorporation of Si in aubrite metal is the cause of the progressively lighter δ^{56}Fe of such metal, especially since the Si content of aubrite metal is much lower (≤2.12 wt.% Si) compared to that in the studied Fe-Si alloy (17 wt.% Si)[50].

A linear relationship between force constants of Fe bonds and pressure based on NRIXS spectroscopy is reported for Fe-alloys[24]. Force constants, which are a measure of bond strength, can be used to derive reduced partition function ratios, also called β-factors, which in turn can be used to calculate the Fe isotope composition at a given temperature. Based on the linear relationship between force constant ($\langle F \rangle$) and pressure (P), i.e.,

$$\langle F \rangle = a*P+b \quad (3.2)$$

and the constants *a* and *b* corresponding to Fe-alloys[24], we find that the values for $\langle F \rangle$ of Fe bonds in $Fe_{86.8}Ni_{8.6}Si_{4.6}$ (174.20±6.50 N/m) and $Fe_{92}Ni_8$ (167.00±17.30 N/m) are similar at a pressure of ~0 GPa (appropriate for the interior of the aubrite parent

body). As such, no resolvable difference is expected in the β-factors of Fe bonds in $Fe_{86.8}Ni_{8.6}Si_{4.6}$ and $Fe_{92}Ni_8$ alloys. This suggests that at the same temperature, fractionation of iron isotopes between Fe-Ni-Si or Fe-Ni alloy and silicate will be indistinguishable under the low-pressure conditions relevant to asteroidal-sized bodies. We propose here that the range of equilibration temperatures recorded by the aubrite metals (Table 3.1; Fig. 3.2a and 3.2b) is likely related to metal-silicate equilibration at different depths within the aubrite parent body in the early Solar System. This could be the result of inefficient separation of metal during partial melting and differentiation on the aubrite parent bodies[25]. As such, residual metal at greater depths experienced a higher equilibration temperature and, therefore would have a higher Si content and smaller iron isotope fractionation (relative to silicates) compared with metals that equilibrated at shallower depths.

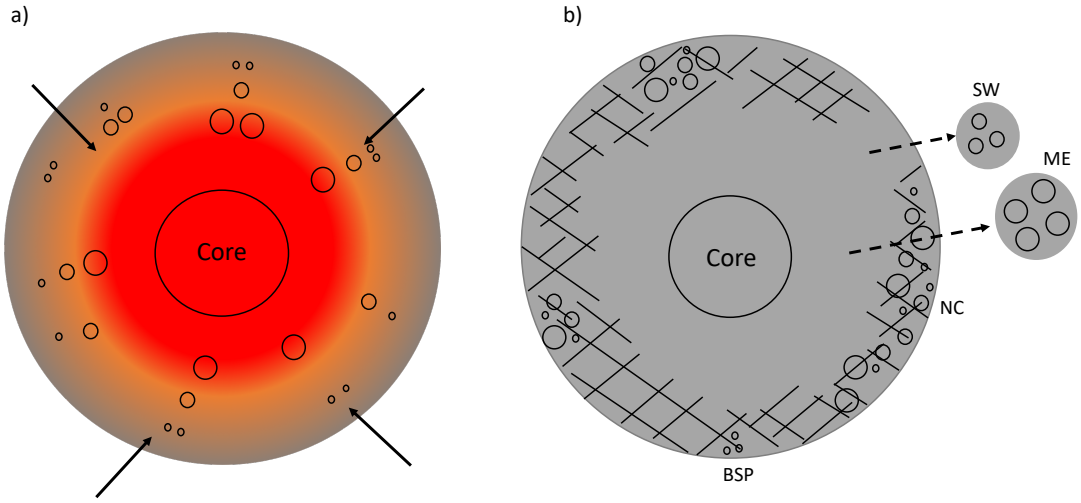

Figure 3.4. (a) Schematic illustration of the aubrite parent body (AuPB) at a time within 4.3 Myr after CAI formation, with warmer colors indicating higher temperatures. Silicon contents and iron isotope compositions of metal grains in aubrites likely record a thermal gradient with depth from surface (larger circles represent metal grains recording higher equilibration temperatures). Impacts (shown as arrows) at this time, while the AuPB was still hot, could have excavated metals from depths of up to ~35 km from the surface. As a result, these excavated metals would have cooled quickly, quenching and preserving the Si contents and $\delta^{56}Fe$ values at their respective metal-silicate equilibration temperatures. (b) Schematic

illustration of the AuPB following impacts that excavated and quenched metals from different depths (and thus record different equilibration temperatures); such metals occur together in the brecciated aubrites, such as Norton County (NC) and Bishopville (BSP), that likely formed at the surface of the main AuPB. The non-brecciated aubrites Mount Egerton (ME) and Shallowater (SW) contain metals that only record equilibration at a particular depth (and equilibration temperature) at their sampling scale. It is possible that these samples may have been ejected altogether from the main AuPB by impacts (and thus did not form as part of near-surface breccias) or originated on distinct parent bodies that were disrupted by impacts.

Several experiments have demonstrated the importance of oxygen concentration in lowering the dihedral angle in Fe-O-S liquids, formation of an interconnected metallic melt network, and percolation of metal in relatively oxidized bodies[51,52]. However, under reducing conditions such as those that existed on the aubrite parent body(s), the presence of Si in iron metal does not reduce its surface tension which consequently increases the dihedral angle above the 60° threshold[52]. This high angle prevents the formation of an interconnected metallic melt network until the percolation threshold is exceeded[53,54]. Once this percolation threshold is exceeded, the metal segregates. But eventually, the melt network is again disconnected as the melt fraction decreases below this threshold; e.g., ~1–2% metal remains trapped in the silicate melt[54]. These trapped pockets of residual metal would subsequently equilibrate with the surrounding silicates. The formation of a metallic core in the aubrite parent body[13,25,55] likely occurred through silicate melting and not percolation alone[52]. Melting experiments conducted on the Indarch EH4 chondrite show onset of melting at 1273 K and complete melting of silicates at 1773 K at ambient pressure[45]; complete melting of such a composition at 1 GPa occurs at 1873 K[46]. Based on these melting experiments[45,46], the calculated equilibration temperatures of between 1432 to 1635 K for the aubrite metals in this study suggest ~7−20% partial silicate melting in the aubrite parent body. This degree of silicate partial melting is insufficient compared to the ~50% silicate melting required for complete segregation of metal[53] (possibly leading to the inefficient separation of

metal). At 1723 K, ~50% silicate melting occurs[45] which leads to loss of shear strength due to convective motion[41] and efficient segregation of metal[53]. Therefore, we consider 1723 K as an upper limit for our calculations of the thermal profile within the aubrite parent body (Fig. 3.3) as further increase in temperature would lead to the near-complete melting of the aubrite parent body[45], onset of convective motion obliterating any thermal gradient[41], and efficient separation of metal[53]. Our calculations indicate that the thermal profile relevant to the equilibration temperature range recorded by the Si-bearing aubrite metals can be attained within 4.3 Myr after CAI formation, at a minimum depth of up to ~35 km from the surface (Fig. 3.3). This time interval is consistent with the ^{26}Al-^{26}Mg age of ~2.9 Myr after CAI formation[56] and the ^{129}I-^{129}Xe age of 4 ± 0.43 Myr after CAI formation for the crystallization of aubrite pyroxene[57], and the ^{53}Mn-^{53}Cr age of ~4 Myr after CAI formation for the last Mn/Cr fractionation (i.e., global differentiation) event in the aubrite parent body[58]. Subsequent large-scale impacts while the parent body was still hot would have brought the metal grains from a range of depths to the surface, where they would have undergone rapid cooling and retained the Si contents and iron isotope compositions they acquired during metal-silicate equilibration. Indeed, previous studies have suggested that the aubrite parent body(s) underwent a globally disruptive collision and subsequent reassembly to form a "rubble pile" asteroid[27,30].

In such a scenario, the brecciated aubrites would be expected to contain metals that equilibrated at different depths and were mixed together on the size-scale of the known meteorite sample. This is thought to be the case for the Norton County aubrite. This 1-ton meteorite provides abundant material for study, and over half of the metal grains studied here are from this sample. In contrast, the known masses of the unbrecciated aubrites Shallowater and Mount Egerton would be expected to only sample material from specific (shallower and deeper, respectively)

depths of their parent body(s) (Fig. 3.4). Lack of brecciation (and thus no mixing of populations from different depths) explains the uniformity of the Si contents and δ^{56}Fe values in different metal grains in each of these samples.

Shallowater[30] and Mount Egerton[32] have been proposed to belong to parent bodies distinct from the main aubrite body (from which Norton County and Bishopville originated). In fact, Shallowater is suggested to have undergone a complex cooling history, the first stage of which involved fast cooling from well above ~1273K, most likely due to a low-velocity collision, breakup and reassembly of a partly molten parent body[30]. Irrespective of whether or not these unbrecciated aubrites originated on the main aubrite parent body, the anti-correlation between the Si and δ^{56}Fe holds true for all the aubrite metals studied here and likely implies broadly similar cooling and disruption histories. Furthermore, given that our study shows that brecciated aubrite metals record equilibration with silicates over a range of temperatures, one cannot assume a single equilibration temperature to estimate the metal-silicate iron isotope fractionation factor from such samples.

3.4 Methods

3.4.1 Bulk elemental composition and iron isotope measurements

Bulk compositions were measured by wavelength-dispersive spectroscopy (WDS) using a JEOL JXA-8530F electron microprobe in the Eyring Materials Center at Arizona State University (ASU) and a CAMECA SX100 electron microprobe in the Michael J. Drake Electron Microprobe laboratory at University of Arizona. Standards used for calibration are Fe-metal, troilite, and schreibersite (Fe and P), Ni metal, Co metal, troilite (S), and elemental Si. Bulk elemental abundances (Table 3.1) were acquired using a defocused diameter 100 μm beam at operating conditions of 20 kV and 20 nA. Elemental abundances for each metal are reported as averages of 40 to 200 analyzed points along transects across the metal. Accuracy and precision of our

analyses were verified by comparing the elemental compositions of the Horse Creek, Monahans, and Santiago Papasquiero iron meteorites with published values. The samples studied here include 17 metal grains from four aubrites: ten from Norton County (NC2 to NC4, NC6 to NC12), four from Mount Egerton (ME1-4), two from Shallowater (SW1, SW3), and one from Bishopville (BSP3). Each metal grain was cut in half using a diamond-plated wafering blade; one half of each metal was used to create a polished mount for electron microprobe study (Supplementary Fig. A3.1).

The half of each metal small grain not embedded in epoxy was abraded using sand-paper and inspected under the microscope to ensure it was free of adhering silicates and rust. For the largest metal grains (NC7-12; ME1-4), a clean interior piece was cut using the diamond-plated wafering blade. The cleaned metal pieces were ultrasonicated in methanol, dried, and then dissolved in concentrated HCl. After careful inspection to ensure complete dissolution, solutions were then purified via column chromatography to separate Fe for isotopic measurements. All chemical procedures were carried out under clean laboratory conditions in the Isotope Cosmochemistry and Geochronology Laboratory (ICGL) at ASU. To ensure low procedural blanks, all reagents used were obtained or prepared as follows. Nitric acid (HNO_3) was twice distilled from trace metal grade acid using the sub-boiling Savillex DST-1000 Acid Purification System. Hydrochloric acid (HCl) was distilled once from trace metal grade acid using the Savillex DST-1000. Water for acid dilutions and chromatography was purified from reverse osmosis (RO) water using a Millipore Super-Q® water purification system (resistivity ~18 MΩ.cm) followed by a Milli-Q® Element water purification system with a 0.1 µm final filter (resistivity >18.2 MΩ.cm).

Iron purification was conducted via ion exchange column chromatography in the ICGL at ASU following procedures similar to those described previously[59]. Iron was purified using a Bio-Rad column packed with 1 mL of pre-cleaned anion

exchange Bio-Rad AG 1-X8 200-400 mesh resin. The resin was further cleaned using 0.5 N HCl followed by pre-conditioning with 6 N HCl. Aliquots of dissolved sample solutions (having a maximum of 100 μg of Fe per sample) were loaded onto the column in a 6 N HCl medium. Cations such as Na, Mg, Al, Ca, Ti, V, Cr, and Ni were eluted using 6 N HCl and then Fe was eluted with 0.5 N HCl. The Fe column yield was typically better than 98.5%. The average total procedural blank for all chemical processing including sample digestion and Fe purification was ~10 ng of Fe. Iron isotopes were measured with the Thermo Finnigan Neptune multi-collector inductively coupled plasma mass spectrometer (MC-ICPMS) at ASU using a jet sample cone and an H-skimmer cone in medium-resolution mode (i.e., with a mass resolving power ≥8500). The purified Fe samples and standards were analyzed at concentrations of 500 ppb doped with 500 ppb NIST Cu to correct for instrumental mass bias. Samples were introduced through an ESI APEX-Q sample introduction system attached to a self-aspirating PFA nebulizer with an uptake rate of 100 μL/min. An uptake time of 90 s and a wash time between consecutive sample and standard measurements of 120 s were used. Typical sensitivity achieved for ^{56}Fe signal was ~70V/ppm Fe using a $10^{11}\Omega$ resistor. Data were collected by switching between two different cup configurations wherein ^{53}Cr, ^{54}Fe, ^{56}Fe, ^{57}Fe, ^{58}Fe, and ^{60}Ni isotopes were measured in parallel during the first integration of 8 s using the L4, L2, C, H1, H2, and H4 Faraday cups respectively. Subsequently, ^{63}Cu and ^{65}Cu were measured during the second integration of 4 s using the L1 and C Faraday cups respectively. Each run for a sample, standard, or blank comprised 20 cycles. Measurements of ^{53}Cr and ^{60}Ni were used to correct for potential isobaric interferences of ^{54}Cr and ^{58}Ni on ^{54}Fe and ^{58}Fe, respectively. All data reduction was performed offline using the Iolite software. We corrected for instrumental mass fractionation using the exponential mass fractionation law such that the corrected isotope ratio (denoted by an asterisk) is given by:

$$\left(\frac{^{x}Fe}{^{54}Fe}\right)^{*} = \left(\frac{^{x}Fe}{^{54}Fe}\right)_{measured} \times \left(\frac{M_x}{M_{54}}\right)^{\beta} \quad (3.3)$$

where ^{x}Fe is ^{56}Fe or ^{57}Fe, M_x and M_{54} are atomic masses of ^{x}Fe and ^{54}Fe respectively and fractionation factor β is defined by

$$\beta = \frac{\ln\left[\frac{\left(\frac{^{63}Cu}{^{65}Cu}\right)_{true}}{\left(\frac{^{63}Cu}{^{65}Cu}\right)_{measured}}\right]}{\ln\left(\frac{M_{63}}{M_{65}}\right)} \quad (3.4)$$

where $(^{63}Cu/^{65}Cu)_{true}$ is the true isotopic abundance ratio of ^{63}Cu and ^{65}Cu, and M_{63}, M_{65} are atomic masses of ^{63}Cu and ^{65}Cu respectively. Iron isotope compositions are reported using the δ notation, i.e., parts per thousand deviation (‰) relative to the bracketing standard IRMM-524A according to:

$$\delta^{x}Fe_{sample}(‰) = \left[\frac{\left(\frac{^{x}Fe}{^{54}Fe}\right)^{*}_{sample}}{\left(\frac{^{x}Fe}{^{54}Fe}\right)^{*}_{IRMM-524A}} - 1\right] \times 1000 \quad (3.5)$$

To assess the accuracy and precision of our methodology for Fe isotopic analyses (including chemical separation and mass spectrometry), we analyzed purified Fe from BCR-2, BIR, BHVO-1, TAG-sulfide terrestrial rock standards as well as from a homogenized bulk sample of the Allende CV3 chondrite along with the aubrite metal samples during each MC-ICPMS analytical session. The iron isotope composition reported for each sample is the average of six repeat runs and is reported with the internal 2SE uncertainty of these measurements or the external long-term reproducibility, whichever is larger. The long-term external reproducibility of our analyses based on repeated measurements of the IRMM-524A bracketing standard over the course of this study is 0.010‰ for $\delta^{56}Fe$ and 0.015‰ for $\delta^{57}Fe$ (Supplementary Fig. A3.2).

3.4.2 Calculation of temperature of metal-silicate equilibration

The following relationship[34] was used to calculate the metal-silicate equilibration temperature:

$$\log\left(\frac{x_{Si}^{metal}}{x_{SiO_2}^{silicate}}\right) = a + \frac{b}{\mathrm{T}} + \frac{c\mathrm{P}}{\mathrm{T}} + d\frac{nbo}{t} - 2\log\left(\frac{x_{FeO}^{silicate}}{x_{Fe}^{metal}}\right) - \log\left(\frac{\gamma_{Si}^{metal}}{\left(\gamma_{Fe}^{metal}\right)^2}\right) \quad (3.6)$$

where $x_i^{phase}$is the molar fraction of element *i* in the phase of interest, γ_i^{phase} is the activity coefficient of component '*i*' in the phase of interest. The term *nbo/t* is the ratio of non-bridging oxygens to tetrahedrally coordinated cations in the silicate melt, P is the pressure in GPa, T is temperature in Kelvin, and *a*, *b*, *c*, and *d* are parameters obtained from the regression of experimental data[34] (Supplementary Table A3.1). In their experiment[34], these authors estimated *nbo/t*=1.74 for a reduced E chondrite-like starting composition, a value we also use for the similarly reduced aubrites. The terms x_{Si}^{metal} and x_{Fe}^{metal} for each metal grain have been calculated using the bulk elemental composition (Supplementary Table A3.2). The terms $x_{SiO_2}^{silicate}$ and $x_{Feo}^{silicate}$for each aubrite have been calculated as the weighted average of SiO_2 and FeO, respectively, in various silicate phases in that particular aubrite based on published data[60] (Supplementary Table A3.2). We used γ_{Fe}^{metal}= 0.8 as previously suggested[34], for all our calculations. Uncertainties in T mostly represent uncertainties in the regression parameters[34]. The term γ_{Si}^{metal} for each metal has been calculated using the following equation[61]:

$$\ln\gamma_{Si} = \ln\gamma_{Fe} + \ln\gamma_{Si}^{0} - \varepsilon_{Si}^{Si}\ln(1-x_{Si}) - \sum_{j=2(j\neq Si)}^{N}\varepsilon_{Si}^{j}x_j\left(1 + \frac{\ln(1-x_j)}{x_j} - \frac{1}{1-x_{Si}}\right) +$$

$$\sum_{j=2(j\neq Si)}^{N}\varepsilon_i^j x_j^2\, x_{Si}\left(\frac{1}{1-x_{Si}} + \frac{1}{1-x_j} + \frac{x_{Si}}{2(1-x_{Si})^2} - 1\right) \quad (3.7)$$

where $\ln\gamma_{Si}$ is the activity coefficient of solute Si in the molten alloy made up of N constituents. For this study, based on our bulk elemental data for the metal grains (Table 3.1), we use three constituents (i.e., Ni, Co, and P) other than Si and Fe in

the metal. The term γ_{Si}^{0} is the Raoultian activity coefficient of solute Si at an infinite dilution in pure liquid Fe; ε_{Si}^{j} is the first-order interaction parameter of solute *j* upon Si, and x_{Si}, x_j are the mole fractions of Si and solute *j* in metal. Similar to the previous study[34], we have extrapolated the terms γ_{Si}^{0} and ε_{Si}^{j} which were acquired at 1873 K to a temperature 'T', i.e., calculated *ln* $\gamma_{Si}^{0}(T)$ and $\varepsilon_{Si}^{j}(T)$ according to the following equations:

$$ln\ \gamma_{Si}^{0}(T) = \frac{1873 * ln\,\gamma_{Si}^{0}}{T} \tag{3.8}$$

$$\varepsilon_{Si}^{j}(T) = \frac{1873 * \varepsilon_{Si}^{j}}{T} \tag{3.9}$$

Equations (3.8) and (3.9) and the values of γ_{Si}^{0} and ε_{Si}^{j} at 1873 K have been obtained from the from the Steelmaking Data Sourcebook[62] and are presented in Supplementary Table A3.1.

3.4.3 Calculation of oxygen fugacity

The following relationship was used to calculate the oxygen fugacity relative to the iron-wüstite (IW) buffer:

$$\Delta\mathrm{IW} = 2\log\left(\frac{x_{Feo}^{silicate}}{x_{Fe}^{metal}}\right) + 2\log\left(\frac{\gamma_{Feo}^{silicate}}{\gamma_{Fe}^{metal}}\right) \tag{3.10}$$

where x_i^{phase} and γ_i^{phase} are the molar fraction and activity co-efficient of component '*i*' in the phase of interest, respectively. The term $x_{Feo}^{silicate}$ for each aubrite was calculated as the weighted average of FeO in the silicate phases in that particular aubrite based on published data[60] (Supplementary Table A3.2). We have used $\gamma_{Feo}^{silicate}$= 3±1 and γ_{Fe}^{metal}= 0.8 after a previous study[34]. Uncertainties in fO_2 primarily reflect the uncertainty in $\gamma_{Feo}^{silicate}$. A higher value for $\gamma_{Feo}^{silicate}$ (= 5.83) was used in a previous study[17] to account for the high MgO content (~40 wt.%) in aubrite silicates; using this value translates to fO_2 in the range of –4.8 to –5.1 log units relative to the

iron-wüstite buffer for aubrite metals studied here (compared to –5.1 to –5.4 estimated here; Table 3.1). Irrespective of the choice of $\gamma_{Feo}^{silicate}$ values, the calculated fO_2 values vary little, suggesting that the primary control on Si content and $\delta^{56}Fe$ of metal is temperature.

3.4.4 Thermal modeling of the aubrite parent body

We have used the following equation[41] for calculating the temperature profiles within the aubrite parent body at different times after its accretion:

$$T = T_0 + \frac{\kappa A_0}{K\lambda} e^{-\lambda t}\left[\frac{Rsin\left(r\sqrt{\frac{\lambda}{\kappa}}\right)}{rsin\left(R\sqrt{\frac{\lambda}{\kappa}}\right)} - 1\right] + \frac{2R^3 A_0}{r\pi^3 K}\sum_{n=1}^{\infty}\frac{-1^n}{n\left(n^2 - \frac{\lambda R^2}{\kappa\pi^2}\right)} sin\left(\frac{n\pi r}{R}\right) e^{-\frac{\kappa n^2\pi^2 t}{R^2}} \quad (3.11)$$

where T_0 is the ambient temperature in the disk at the time of accretion of the aubrite parent body; $\mathrm{K\ is\ thermal\ conductivity;}$ κ is the thermal diffusivity defined as $(K/\rho C_P)$, where ρ is density and C_P is specific heat capacity; A_0 is the power output per unit volume at the time of planetesimal formation (see Supplementary Table A3.3 for details on the calculation of A_0); λ is the decay constant of ^{26}Al; t is the time elapsed since accretion; r is the distance from center; and R is the radius of the aubrite parent body. All parameters used in equation (3.11) above are given in Supplementary Table A3.3. Aubrites are suggested to have formed within ~1 AU of the Sun based on their reduced nature[63,64]. As such, as a bounding case, we have used parameters appropriate for formation at 1 AU (Supplementary Table A3.3). We note that the accretion time of the aubrite parent body is not well-constrained. However, thermal modeling assuming ^{26}Al as the primary heat source for core formation on the aubrite parent body suggests that it accreted at or before ~1.5 Myr following CAI formation[40]. The main uncertainties in the modeled accretion age are associated with the temperature of core formation and the Al concentration of the aubrite parent body[40]. Given the estimated upper limit on the accretion time of the

aubrite parent body, we chose to perform our calculations assuming accretion times of 1.0, 1.3, and 1.5 Myr after CAI formation to illustrate the differences in the depth from surface and the time after CAI formation at which the aubrite parent body could have acquired the thermal gradient relevant to the range of metal-silicate equilibration temperatures recorded by the aubrite metals in this study. For each of these accretion times, the relevant ambient temperature at the time of accretion (T_0) at 1 AU is assumed[65] (Supplementary Table A3.3). In Fig. 3.3a–c, for an accretion time of 1.0, 1.3, and 1.5 Myr, respectively, after CAI formation, we have shown the calculated temperature (T in Kelvin) as a function of the distance from the center (r in km) of the aubrite parent body at two different times since CAI formation such that the temperature within the parent body reaches 1635 K (black solid line) (i.e., the highest metal-silicate equilibration temperature recorded in the aubrite metals studied here) and 1723 K (black dashed line) (i.e., the temperature beyond which complete silicate melting occurs such that the resulting convective motion would obliterate any thermal gradient).

We note that recent numerical modeling suggested a formation location of ~2 AU from the Sun for the aubrite parent body[65]. Using parameters relevant for formation at 2 AU (Supplementary Table A3.3) and accretion times of 1.0, 1.3, and 1.5 Myr after CAI formation, we have estimated the times at which the appropriate thermal gradient will be acquired by the aubrite parent body (Supplementary Fig. A3.4). As such, if the aubrite parent body formed at 2 AU, for an estimated maximum accretion time of ~1.5 Myr after CAI formation, we show that the relevant thermal gradient will be attained by 2.5–2.6 Myr after CAI formation; this is well within the maximum time interval of ~4.3 Myr estimated for acquiring the appropriate thermal gradient if the aubrite parent body formed at 1 AU. We also note that our calculations described above are done assuming a canonical $^{26}Al/^{27}Al$ ratio[66-68]. However, if we assume a lower $^{26}Al/^{27}Al$ ratio for inner solar system solids[69], the

aubrite parent body would have to accrete within a few hundred thousand years after CAI formation to generate enough heat to reach a temperature up to ~1635 K in its interior. In such a case, a thermal gradient relevant to the range of metal-silicate equilibration temperatures recorded by the aubrite metals could be acquired within ~5 Myr after CAI formation.

References

1. Kleine, T., Mezger, K., Palme, H., Scherer, E. & Münker, C. Early core formation in asteroids and late accretion of chondrite parent bodies: Evidence from ^{182}Hf-^{182}W in CAIs, metal-rich chondrites, and iron meteorites. *Geochim. Cosmochim. Acta* **69**, 5805–5818 (2005).

2. Scherstén, A., Elliott, T., Hawkesworth, C., Russell, S. & Masarik, J. Hf-W evidence for rapid differentiation of iron meteorite parent bodies. *Earth Planet. Sci. Lett*. **241**, 530–542 (2006).

3. Kruijer, T. S., Burkhardt, C., Budde, G. & Kleine, T. Age of Jupiter inferred from the distinct genetics and formation times of meteorites. *Proc. Natl. Acad. Sci. U. S. A.* **114**, 6712–6716 (2017).

4. Goldstein, J. I., Scott, E. R. D., & Chabot, N. L. Iron meteorites: Crystallization, thermal history, parent bodies, and origin. *Chemie der Erde* **69**, 293–325 (2009).

5. Bonnand, P., & Halliday, A. N. Oxidized conditions in iron meteorite parent bodies. *Nat. Geosci.* **11**, 401-404 (2018).

6. Mittlefehldt, D. W. Achondrites. In *Treatise on Geochemistry* (Second Edition) (eds. K. K. Turekian and H. D. Holland). Elsevier, Oxford, pp. 1-63 (2013).

7. Shahar, A., Savage, P. & Moynier, F. Stable Isotope Evidence for the Differentiation of Planetesimals, In *Planetesimals*, Edited by L.T. Elkins-Tanton and B.P. Weiss Cambridge University Press (2017).

8. Bourdon, B., Roskosz, M. & Hin R. C. Isotope tracers of core formation. *Earth-Science Rev.* **181**, 61–81 (2018).

9. Poitrasson, F., Levasseur, S. & Teutsch, N. Significance of iron isotope mineral fractionation in pallasites and iron meteorites for the core-mantle differentiation of terrestrial planets. *Earth Planet. Sci. Lett.* **234**, 151–164 (2005).

10. Weyer, S. *et al.* Iron isotope fractionation during planetary differentiation. *Earth Planet. Sci. Lett.* **240**, 251–264 (2005).

11. Poitrasson, F., Roskosz, M. & Corgne, A. No iron isotope fractionation between molten alloys and silicate melt to 2000 °C and 7.7 GPa: Experimental evidence and implications for planetary differentiation and accretion. *Earth Planet. Sci. Lett.* **278**, 376–385 (2009).

12. Hin, R. C., Schmidt, M. W. & Bourdon, B. Experimental evidence for the absence of iron isotope fractionation between metal and silicate liquids at 1 GPa and 1250–1300 °C and its cosmochemical consequences. *Geochim. Cosmochim. Acta* **93**, 164–181 (2012).

13. Wang, K., Savage, P. S. & Moynier, F. The iron isotope composition of enstatite meteorites: Implications for their origin and the metal/sulfide Fe isotopic fractionation factor. *Geochim. Cosmochim. Acta* **142**, 149–165 (2014).

14. Shahar, A. *et al.* Sulfur-controlled iron isotope fractionation experiments of core formation in planetary bodies. *Geochim. Cosmochim. Acta* **150**, 253–264 (2015).

15. Elardo, S. M. & Shahar, A. Non-chondritic iron isotope ratios in planetary mantles as a result of core formation. *Nat. Geosci.* **10**, 317–321 (2017).

16. Elardo, S. M., Shahar, A., Mock, T. D. & Sio, C. K. The effect of core composition on iron isotope fractionation between planetary cores and mantles. *Earth Planet. Sci. Lett.* **513**, 124–134 (2019).

17. Jordan, M. K., Tang, H. L., Kohl, I. E. & Young, E. D. Iron isotope constraints on planetesimal core formation in the early solar system. *Geochim. Cosmochim. Acta* **246**, 461–477 (2019).

18. Schauble, E. A. Applying stable isotope fractionation theory to new systems. *Rev. Mineral. Geochemistry* **55**, 65–111 (2004).

19. Young, E. D. *et al.* High-temperature equilibrium isotope fractionation of non-traditional stable isotopes: Experiments, theory, and applications. *Chem. Geol.* **395**, 176–195 (2015).

20. Williams, H. M. *et al.* Fe isotope fractionation in iron meteorites: New insights into metal-sulphide segregation and planetary accretion. *Earth Planet. Sci. Lett.* **250**, 486–500 (2006).

21. Needham, A. W., Porcelli, D. & Russell, S. S. An Fe isotope study of ordinary chondrites. *Geochim. Cosmochim. Acta* **73**, 7399–7413 (2009).

22. Theis, K. J., Burgess, R., Lyon, I. C. & Sears, D. W. The origin and history of ordinary chondrites: A study by iron isotope measurements of metal grains from ordinary chondrites. *Geochim. Cosmochim. Acta* **72**, 4440–4456 (2008).

23. Wang, K., Day, J. M. D., Korotev, R. L., Zeigler, R. A. & Moynier, F. Iron isotope fractionation during sulfide-rich felsic partial melting in early planetesimals. *Earth Planet. Sci. Lett.* **392**, 124–132 (2014).

24. Liu, J. *et al.* Iron isotopic fractionation between silicate mantle and metallic core at high pressure. *Nat. Commun.* **8**, 1–6 (2017).

25. Casanova, I., Keil, K. & Newsom, H. E. Composition of metal in aubrites: Constraints on core formation. *Geochim. Cosmochim. Acta* **57**, 675–682, (1993).

26. Keil, K. Enstatite achondrite meteorites (aubrites) and the histories of their asteroidal parent bodies. *Chemie der Erde* **70**, 295–317 (2010).

27. Okada, A., Keil K., Taylor, G. J. & Newsom, H. Igneous history of the aubrite parent asteroid: evidence from the Norton County enstatite achondrite. *Meteoritics* **23**, 59–74 (1988).

28. Keil, K. Enstatite meteorites and their parent bodies. *Meteoritics* **24**, 195–208 (1989).

29. Mittlefehldt, D.W., McCoy, T.J., Goodrich, C.A. & Kracher, A. Non-chondritic meteorites from asteroidal bodies. *Reviews in Mineralogy and Planetary Materials*, **36**, Mineralogical Society of America, 1-195 (1998).

30. Keil, K., Ntaflos, T., Taylor, G. J., Brearley, A. J., Newsom, H. E. & Romig, A. D. The Shallowater aubrite: Evidence for origin by planetesimal impacts. *Geochim. Cosmochim. Acta* **53**, 3291–3307 (1989).

31. Watters, T. R. & Prinz, M. Mt. Egerton and the aubrite parent body. *Lunar Planet. Sci. Conf.* **11**, 1225-1226 (1980).

32. Barrat, J. A., Greenwood, R. C., Keil, K., Rouget, M. L., Boesenberg, J. S., Zanda, B. & Franchi, I. A. The origin of aubrites: Evidence from lithophile trace element abundances and oxygen isotope compositions. *Geochim. Cosmochim. Acta* **192**, 29–48 (2016).

33. Wade, J. & Wood, B. J. Core formation and the oxidation state of the Earth. *Earth Planet. Sci. Lett.* **236**, 78–95 (2005).

34. Corgne, A., Keshav, S., Wood, B. J., McDonough, W. F. & Fei, Y. Metal-silicate partitioning and constraints on core composition and oxygen fugacity during Earth accretion. *Geochim. Cosmochim. Acta* **72**, 574–589 (2008).

35. Wasson, J.T., Kallemeyn, G.W. & Rubin, A.E. Equilibration temperatures of EL chondrites: a major downward revision in the ferrosilite contents of enstatite. *Meteoritics* **29**, 658–662 (1994).

36. Ziegler, K., Young, E. D., Schauble, E. A. & Wasson, J. T. Metal-silicate silicon isotope fractionation in enstatite meteorites and constraints on Earth's core formation. *Earth Planet. Sci. Lett.* **295**, 487–496 (2010).

37. Ntaflos, T., Keil, K. & Newsom, H. E. Khor Temiki: An enstatite achondrite with evidence of mixing of metal and sulfides from separate sources. *LPSC XIX,* (1988).

38. McCoy, T. J. & Bullock, E. S. Differentiation under highly reducing conditions: New insights from enstatite meteorites and Mercury. In *Planetesimals*, Edited by L.T. Elkins-Tanton and B.P. Weiss Cambridge University Press (2017).

39. Kleine, T. & Wadhwa, M. Chronology of Planetesimal Differentiation, In *Planetesimals*, Edited by L.T. Elkins-Tanton and B.P. Weiss Cambridge University Press (2017).

40. Sugiura, N. & Fujiya, W. Correlated accretion ages and ε^{54}Cr of meteorite parent bodies and the evolution of the solar nebula. *Meteorit. Planet. Sci.* **49**, 772–787 (2014).

41. Hevey, P. J. & Sanders, I. S. A model for planetesimal meltdown by ^{26}Al, and its implications for meteorite parent bodies. *Meteoritics & Planetary Science* **41**, 95-106 (2006).

42. Qin, L., Dauphas, N., Wadhwa, M., Masarik, J. & Janney, P. E. ^{182}Hf–^{182}W chronometry and thermal modeling. *Earth and Planetary Science Letters* **273**, 94-104 (2008).

43. Urey, H.C. The thermodynamic properties of isotopic substances. *J. Chem. Soc*. 562–581, (1947).

44. Bigeleisen, J. & Mayer, M.G. Calculation of equilibrium constants for isotopic exchange reactions. *J. Chem. Phys*. **15**, 261–267 (1947).

45. McCoy, T. J., Dickinson, T. L. & Lofgren, G. E. Partial melting of the Indarch (EH4) meteorite: A textural, chemical, and phase relations view of melting and melt migration. *Meteorit. Planet. Sci.* **34**, 735–746 (1999).

46. Berthet, S., Malavergne, V. & Righter, K. Melting of the Indarch meteorite (EH4 chondrite) at 1 GPa and variable oxygen fugacity: Implications for early planetary differentiation processes. *Geochim. Cosmochim. Acta* **73**, 6402–6420 (2009).

47. Shahar, A., Young, E. D. & Manning, C. E. Equilibrium high-temperature Fe isotope fractionation between fayalite and magnetite: An experimental calibration. *Earth Planet. Sci. Lett.* **268**, 330–338 (2008).

48. Dauphas, N. *et al.* Iron isotopes may reveal the redox conditions of mantle melting from Archean to present. Earth Planet. Sci. Lett. **288**, 255–267 (2009).

49. Dauphas, N. *et al*. Magma redox and structural controls on iron isotope variations in Earth's mantle and crust. *Earth Planet. Sci. Lett.* **398**, 127–140 (2014).

50. Sanloup, C., Guyot, F., Gillet, P. & Fei, Y. Physical properties of liquid Fe alloys at high pressure and their bearings on the nature of metallic planetary cores. *J. Geophys. Res.: Solid Earth*. **107**, 2272-2280 (2002).

51. Terasaki, H., Frost, D. J. & Rubie, D. C., Langenhorst, F. Percolative core formation in planetesimals. *Earth Planet. Sci. Lett.* **273**, 132–137 (2008).

52. Mann, U., Frost, D. J. & Rubie, D. C. The wetting ability of Si-bearing liquid Fe-alloys in a solid silicate matrix-percolation during core formation under reducing conditions? *Phys. Earth Planet. Inter.* **167**, 1–7 (2008).

53. Taylor, G. J. Core formation in asteroids. *J. Geophys. Res.* **97**, 717–726 (1992).

54. Ghanbarzadeh, S., Hesse, M. A., Prodanović, M. & Schubert, G. Percolative core formation in planetesimals enabled by hysteresis in metal connectivity. *Proc. Natl. Acad. Sci. U. S. A.* **114**, 13406–13411 (2017).

55. Lodders, K., Palme, H. & Wlotzka, F. Trace elements in mineral separates of the Peña Blanca Spring aubrite: Implications for the evolution of the aubrite parent body. *Meteoritics* **28**, 538-551 (1993).

56. Baker, J. A., Schiller, M. & Bizzarro, M. ^{26}Al-^{26}Mg deficit dating ultramafic meteorites and silicate planetesimal differentiation in the early Solar System? *Geochim. Cosmochim. Acta* **77**, 415–431 (2012).

57. Hohenberg, C. M. & Pravdivtseva, O. V. I-Xe dating: From adolescence to maturity. *Chemie der Erde* **68**, 339–351 (2008).

58. Shukolyukov, A. & Lugmair, G. W. Manganese-chromium isotope systematics of enstatite meteorites. *Geochim. Cosmochim. Acta* **68**, 2875–2888 (2004).

59. Arnold, G. L., Weyer, S. & Anbar, A. D. Fe isotope variations in natural materials measured using high mass resolution multiple collector ICPMS. *Anal. Chem.* **76**, 322-327 (2004).

60. Watters, T. R. & Prinz, M. Aubrites: Their origin and relationship to enstatite chondrites. *Proc. Lunar Planet. Sci Conf.* **X**, 1073-1093 (1979).

61. Ma, Z. Thermodynamic description for concentrated metallic solutions using interaction parameters. *Metall. Mater. Trans. B Process Metall. Mater. Process. Sci.* **32**, 87–103 (2001).

62. The Japan Society for the Promotion of Science and The Nineteenth Committee on Steelmaking Part 2: Recommended values of activity and activity coefficients, and interaction parameters of elements in iron alloys. In *Steelmaking Data Sourcebook*. Gordon and Breach Science Publishers, New York. pp. 273–297 (1988).

63. Baedecker, P.A. & Wasson, J.T. Elemental fractionation among enstatite chondrites. *Geochim. Cosmochim. Acta* **39**, 735–765 (1975).

64. Kallemeyn, G.W. & Wasson, J.T. Compositions of enstatite (EH3, EH4,5 and EL6) chondrites: implications regarding their formation. *Geochim. Cosmochim. Acta* **50**, 2153-2164 (1986).

65. Desch, S. J., Kalyaan, A. & Alexander C. M. O. The Effect of Jupiter's Formation on the Distribution of Refractory Elements and Inclusions in Meteorites. *Astrophys. J. Suppl. Ser.* **238**, 11 (2018).

66. Kita, N. T. *et al.* ^{26}Al-^{26}Mg isotope systematics of the first solids in the early solar system. *Meteorit. Planet. Sci.* **48**, 1383–1400 (2013).

67. Jacobsen, B. *et al.* 26Al-26Mg and 207Pb-206Pb systematics of Allende CAIs: Canonical solar initial 26Al/27Al ratio reinstated. *Earth and Planetary Science Letters* **272**, 353–364 (2008).

68. Gregory, T., Luu, T. H., Coath, C. D., Russell, S. S. & Elliott, T. Primordial formation of major silicates in a protoplanetary disc with homogeneous 26Al/27Al. *Science Advances* **6**, 1–9 (2020).

69. Schiller, M., Connelly, J. N., Glad, A. C., Mikouchi, T. & Bizzarro, M. Early accretion of protoplanets inferred from a reduced inner solar system 26Al inventory. *Earth and Planetary Science Letters* **420**, 45–54 (2015).

Data availability

The datasets generated during and/or analyzed during the current study are included in the main text and supplementary information.

Acknowledgements
We thank R. Hines and S. J. Romaniello for their invaluable assistance in the Isotope Cosmochemistry and Geochronology (ICGL) at ASU. We thank Carl Agee for providing Norton County nodules NC7-12 for this study. We also thank the two anonymous reviewers for their insightful comments that helped to improve the manuscript. We acknowledge the use of facilities in the Eyring Materials Center at Arizona State University, and are grateful to the staff at these facilities for their assistance. This work was supported by NASA Emerging Worlds grant (NNX15AH41G) to MW, NASA Earth and Space Science Fellowship (80NSSC18K1269) to SR and MW, and a NASA Emerging Worlds grant (NNX17AE56G) to L.A.J.G.

Author contributions
S.R. and M.W. designed the project. L.A.J.G and S.R. acquired elemental data for the metals. S.R. and V.K.R acquired the isotopic data. All authors contributed to the interpretation of the results, and S.R. conducted the modeling calculations. S.R. wrote the draft and all authors contributed to the revision of the manuscript.

Competing interests
The authors declare no competing interests.

Materials & Correspondence
Correspondence and materials should be addressed to S.R.

CHAPTER 4

SILICON AND IRON ISOTOPE COMPOSIITONS OF AUBRITES AND HORSE CREEK IRON METEORITE: IMPLICATIONS FOR USING $\delta^{30}Si$–$\delta^{56}Fe$ SYSTEMATICS AS A TRACER OF CORE FOMRATION AND PARTIAL MELTING

4.1 Introduction

Fractionation of stable isotopes of the 'common elements' viz., Mg, Fe, and Si has provided invaluable insights into the processes that have occurred on meteorite parent bodies. Results of numerical modeling (Hin et al., 2017, Young et al., 2019) and high precision isotope data for Mg (Young et al., 2009, Hin et al., 2017), Fe (Poitrasson et al., 2004; Sossi et al., 2016a; Poitrasson et al., 2019; Jordan et al., 2019), and Si (Pringle et al., 2014; Moynier et al., 2020) have been interpreted as evidence for vaporization or volatile depletion being the dominant process to explain the observed isotope fractionation in distinct planetary materials. An enrichment of the heavier isotopes of each 'common element' could be considered as evidence for loss of the lighter isotopes due to volatilization from molten planetesimals. Specifically, the positive correlation between Fe and Si isotopes of planetary basalts from distinct parent bodies has been interpreted to reflect volatile depletion (e.g., Sossi et al., 2016a). Although condensation from the solar nebula has been invoked to explain the Si isotope composition of various materials (Dauphas et al., 2015), recent high precision Mg (Hin et al., 2017) and Si (Moynier et al., 2020) isotope data favors vaporization/volatile depletion. Possibly, the most debated of all probable causes of the observed fractionation of Fe and Si isotopes, however, is the mass transfer of elements during core formation (e.g., Georg et al., 2007; Shahar et al., 2015; Elardo and Shahar, 2017; Elardo et al., 2019).

The formation of a core is a fundamental physical and chemical process in the evolutionary history of a rocky body. Isotopic fractionation during mass transfer of Fe

and other alloying elements to form the metal core has been extensively studied (e.g., Bourdon et al., 2018 and references therein; Elardo et al., 2019). Specifically, in the case of Fe and Si, several studies have attempted to constrain the magnitude of isotopic fractionation through investigation of meteorites (Poitrasson et al., 2004; 2007; Weyer et al., 2005; Wang et al., 2014b; Jordan et al., 2019; Georg et al., 2007; Ziegler et al., 2010; Armytage et al., 2011; Moynier et al., 2020), laboratory experiments (Poitrasson et al., 2009; Shahar et al., 2009; 2011; Hin et al., 2012; 2014; Shahar et al., 2015; Elardo and Shahar, 2017; Elardo et al., 2019), and Nuclear Resonant Inelastic X-Ray spectroscopy (Polyakov, 2009; Shahar et al., 2016; Liu et al., 2017). Magnesium would potentially fractionate into the metal core beyond 3000 K (Wahl and Militzer, 2015; Takafuji et al., 2005; Fischer et al., 2015), so fractionation of Mg isotopes, if any, during core formation will be rendered undetectable at such high temperatures (Hin et al., 2017) and is not the focus of this study.

According to first principles of crystal-chemistry involving bond strength, Fe-metal will be enriched in the heavier isotopes of Fe (Schauble, 2004; Young et al., 2015). When Si alloys with Fe-metal, due to increasing temperature or decreasing fO_2 (e.g., Gessmann et al., 2001); the Fe-metal will be enriched in the lighter isotopes of Si (Georg et al., 2007). Hence, in a differentiated body that would incorporate Si in its metallic core, the core will have a heavier δ^{56}Fe and lighter δ^{30}Si compared to its bulk starting composition. As a result, the silicate portion of such a differentiated body would be characterized by a complementary heavier δ^{30}Si and lighter δ^{56}Fe composition. On the other hand, planetesimals that do not have a Si-rich core should be expected to have a silicate mantle with chondritic δ^{30}Si and lighter δ^{56}Fe.

Parent bodies of existing magmatic iron meteorites formed under relatively oxidizing conditions as revealed by mass-dependent fractionation of Cr isotopes

(Bonnand and Halliday, 2018). The paucity of Si-bearing magmatic iron meteorites, i.e., those formed under reducing conditions, could be a result of the participation of such reduced bodies in the formation of the terrestrial planets. Our current inability to access Si-bearing cores of differentiated planets (e.g., Earth and Mercury) makes aubrites, which are samples from reduced, differentiated planetesimals, excellent windows to understand the processes operating during the differentiation of such reduced bodies. Aubrites are ortho-pyroxenites that have Si-bearing metal co-existing with silicates/sulfides (Keil, 2010) and are considered to be products of melting of an enstatite chondrite-like precursor (Casanova et al., 1993, Lodders et al., 1993). Enstatite chondrites (EC) have a δ^{56}Fe composition identical to carbonaceous (CC) and ordinary chondrites (OC) (Poitrasson et al., 2005; Schoenberg and Blanckenburg, 2006; Teng et al., 2008; Dauphas et al., 2009; Craddock and Dauphas, 2011; Wang et al., 2014b) but a lighter δ^{30}Si composition (Fitoussi et al., 2009; Armytage et al., 2011; Savage and Moynier, 2013). The lighter δ^{30}Si of ECs has been attributed to nebular processes such as equilibrium fractionation between solid forsterite and gaseous SiO in the nebula (Dauphas et al., 2015); removal of a refractory, heavy δ^{30}Si component from the source region (Kadlag et al., 2019) or fractionation during nebular condensation of Si-bearing metal in ECs (Sikdar and Rai, 2020). Compared to an EC-like starting composition, bulk aubrites have heavier δ^{30}Si and lighter δ^{56}Fe, a signature that the silicate portion of a differentiating body with Si in its core would acquire (see above). This, conversely means, that the metallic core of the aubrite parent body is characterized by a lighter δ^{30}Si and heavier δ^{56}Fe composition compared to enstatite chondrites. As aubrites are the products of separation of a Si-rich metal core on the parent body (Casanova et al., 1993), the correlated investigation of δ^{30}Si–δ^{56}Fe of metals and silicates from aubrites (products of differentiation) and enstatite chondrites (putative

starting materials) could help constrain the magnitude of fractionation of Si and Fe isotopes during core formation in reduced bodies.

Previously, we studied the correlation between δ^{56}Fe with Si wt% (Chapter 3 in this thesis). However, a systematic study of the variation of δ^{30}Si with Si wt% of aubrite metal has not been attempted so far. In this study, we report the δ^{30}Si values of metals from the brecciated Norton County and unbrecciated Mount Egerton aubrites. We also report the δ^{30}Si and δ^{56}Fe value of the Horse Creek ungrouped iron meteorite which has been considered to represent the core of the aubrite parent body (Watters and Prinz, 1980). We then compare the δ^{30}Si (this study) and δ^{56}Fe (Chapter 3) of these aubrite metals with the δ^{30}Si and δ^{56}Fe of metals from ECs and non-metallic fractions from both ECs and aubrites from published literature data. Further, we determine the Fe and Si isotope fractionation factor between metal and silicates in enstatite chondrites (undifferentiated nebular precursors) and aubrites (differentiated products). The overall goal of this study is to determine the role of metal segregation (core formation) on Fe and Si isotopes under reducing conditions and whether this isotope pair can be used as a proxy for core formation on the aubrite parent body. We also assess whether core formation and partial melting can simultaneously explain the Fe and Si of various asteroidal and planetary bodies such as the angrite parent body, Vesta, Moon, Mars, and Earth.

4.2 Methods

All analytical procedures were carried out in the Isotope Cosmochemistry and Geochronology Laboratory at ASU. To ensure low procedural blanks, all reagents used during the course of this work were obtained or prepared as follows. We obtained Suprapur sodium hydroxide monohydrate ($NaOH.H_2O$) flakes for the alkali fusion method of dissolving samples. Hydrochloric acid (HCl) was distilled once from trace metal grade acid using the Savillex DST-1000 Acid Purification System. To

purify water used for acid dilutions and chromatography, reverse osmosis (RO) water was passed through a Millipore Super-Q® water purification system (resistivity ~18 MΩ-cm) and a Millipore Milli-Q® water purification system with a 0.1 µm final filter (resistivity >18.2 MΩ-cm).

The samples in this study include eleven metals in total: six from Norton County (NC7−12), four from Mount Egerton (ME1−4), and the Horse Creek iron meteorite (HC). The Fe isotope composition of all the metals from Norton County and Mount Egerton have been previously reported in Chapter 3. From the clean, interior, and flat surface of each half of the metal that was used to sample for measuring the δ^{56}Fe (Chapter 3), sample was drilled out in raster mode using a tungsten carbide drill bit on the New Wave Research MicroMill. About ~1mg of the fine metal powder was mixed with about ~50 mg $NaOH.H_2O$ flakes in a round-bottomed Teflon beaker. This 50:1 flux-sample mixture was heated on a hotplate at 250ºC for ~40 hours to ensure complete digestion. Details of this alkali fusion technique have been described in Chapter 3. We observed that metals dissolve easily compared to silicates, hence the smaller flux/sample ratio and shorter duration of heating. The high Fe/Si ratio of Si-bearing metals resulted in the formation of a brown residue due to precipitation of $Fe(OH)_2$ as has been observed for several Fe-rich samples (Chen et al., 2017 and references therein). Addition of HCl ensured the complete dissolution of the brown precipitate and results in a clear solution. A 10 ml final solution of pH~2 was prepared for column chromatography.

Solutions containing of up to 10 µg Si were loaded onto columns with cleaned 1.8ml of AG50W-X8 (200-400 mesh) cation exchange resin. Since Si occurs as neutral or negative ions, it is not exchanged on the cation exchange resin, facilitating its elution using incremental volumes of a total 15 ml of Milli-Q® water. The metal samples are passed through the cation exchange resin multiple times to ensure that all matrix elements are removed. The Si cut was acidified using concentrated HCl to

make a final solution of 0.05 N HCl. Silicon yields were always better than ~99%. Final solutions with Si concentration of 1 ppm were made to measure Si isotopes. To purify Fe from the Horse Creek iron meteorite solution, a small volume of the sample solution was pipetted into a clean and dry Teflon beaker, dried down multiple times, and brought up in 6N HCl. Iron purification was conducted via ion exchange column chromatography following procedures similar to those described in Chapter 2. To purify iron, solution containing about 20 μg of Fe in a 6 N HCl medium was loaded onto a Bio-Rad column packed with pre-cleaned and conditioned anion exchange AG 1-X8 200-400 mesh resin, followed by matrix elution using 6 N HCl and Fe elution using 0.5 N HCl. The Fe column yield was typically better than ~99%. A final solution containing 500 ppb of Fe and 500 ppb of NIST-Cu were made to measure Fe isotopes. Subsequently, Si and Fe isotopes were measured on the Thermo Finnigan Neptune multi-collector inductively coupled plasma mass spectrometer (MC-ICPMS) according to the methods described in Chapter 2. The isotope ratios of standards such as Allende, diatomaceous earth, BCR-2, and BHVO-1 were repeatedly measured to ensure the accuracy and precision of the measurements during each analytical session.

4.3 Results

The isotope compositions of all metals are reported in Table 4.1. Metals from Mount Egerton metals (ME1−4) have similar δ^{29}Si (average = −3.255±0.247‰, 2SD) and δ^{30}Si values (average = −6.307 ± 0.489‰, 2SD). The δ^{29}Si values of metals from Norton County range from −1.889 ± 0.017‰ to −3.621 ± 0.077‰ and the δ^{30}Si values range between −3.657 ± 0.123‰ and −6.911 ± 0.124‰. For Horse Creek, the δ^{29}Si and δ^{30}Si values are −1.461 ± 0.025‰ and −2.794 ± 0.083‰ while the δ^{56}Fe and δ^{57}Fe values are 0.025 ± 0.015‰ and 0.049 ± 0.020‰.

Table 4.1. Silicon isotopic compositions of aubrite metals (NC: Norton County; ME: Mount Egerton) and Horse Creek (HC) iron meteorite. The Si wt% and equilibration temperature T (K) for NC and ME metals are from Chapter 3. The $\Delta^{30}Si_{silicate\text{-}metal}$ values are calculated using the $\delta^{30}Si_{metal}$ from this study and published values of $\delta^{30}Si_{silicate}$ (Ziegler et al., 2010; Fitoussi and Bourdon, 2012) for that particular meteorite; $\Delta^{29}Si_{silicate\text{-}metal}$ is calculated similarly. Note that Horse Creek is devoid of silicates so T, $\Delta^{29}Si$ and $\Delta^{30}Si$ for Horse Creek are not calculated).

Sample	Si wt%	δ^{29}Si±2SE (‰)	δ^{30}Si±2SE (‰)	$\Delta^{29}Si_{silicate-metal}$	$\Delta^{30}Si_{silicate-metal}$	T(K)
NC7	1.67	−1.889±0.017	−3.657±0.123	1.444±0.069	2.842±0.163	1608±30
NC8	1.39	−2.078±0.042	−4.026±0.152	1.633±0.079	3.211±0.186	1596±30
NC9	2.12	−3.229±0.077	−6.350±0.111	2.784±0.102	5.535±0.155	1626±31
NC10	1.75	−2.458±0.077	−4.875±0.124	2.013±0.102	4.060±0.164	1613±30
NC11	0.64	−3.621±0.077	−6.911±0.124	3.176±0.102	6.096±0.164	1545±28
NC12	0.73	−2.743±0.077	−5.237±0.124	2.298±0.102	4.422±0.164	1555±28
ME1	2.00	−3.186±0.058	−6.169±0.070	2.786±0.176	5.423±0.334	1633±31
ME2	2.00	−3.185±0.027	−6.155±0.029	2.785±0.168	5.408±0.328	1634±31
ME3	2.01	−3.439±0.036	−6.670±0.090	3.039±0.170	5.923±0.339	1633±31
ME4	2.07	−3.208±0.050	−6.233±0.032	2.808±0.173	5.486±0.329	1635±31
HC	2.76	−1.461±0.025	−2.794±0.083	–	–	-

4.4. Discussion

4.4.1 Aubrite parent body

4.4.1.1 Bulk aubrites

Based on the offset between δ^{30}Si of EH chondrites (-0.668 ± 0.036‰) and aubrites (-0.599 ± 0.048‰), we can calculate the fraction of Si that goes into the core of the aubrite parent body (f_{Si}^{core}) using the following mass balance equation,

$$\delta^{30}Si_{aubrites} - \delta^{30}Si_{EH} = f_{Si}^{core}(\Delta^{30}Si_{silicate-metal}) \quad (4.1)$$

where $\Delta^{30}Si_{silicate-metal}$ is $\frac{7.64\times10^6}{T^2}$ (Ziegler et al., 2010) and T is 1635 K based on peak temperature recorded by the aubrite metals (Chapter 3). A f_{Si}^{core}= 0.025 thus calculated, yields a $\delta^{30}Si_{AuPB\ core}$ ~ −3.457‰ based on the following equation,

$$(1 - f_{Si}^{core}) * \delta^{30}Si_{aubrites} + f_{Si}^{core} * \delta^{30}Si_{core} = \delta^{30}Si_{EH} \quad (4.2)$$

and C_{Si}^{core} ~ 2.1 wt% in the core according to,

$$f_{M}^{core} = \left[1 + \left(\frac{C_{M}^{mantle}}{C_{M}^{core}}\right) \times \left(\frac{M_{mantle}}{M_{core}}\right)\right]^{-1} \quad (4.3)$$

where $C_{M}^{reservoir}$ is the mass fraction of solute (Fe or Si) in that reservoir, i.e., mantle or core, M_{mantle} and M_{core} are the masses of mantle and core of the aubrite parent body (AuPB). We have assumed a C_{Si}^{mantle} = 27.3 wt% based on the 58.5 wt% SiO_2 in aubrites (Keil, 2010) and $\frac{M_{mantle}}{M_{core}} = \frac{0.75}{0.25}$ based on a core of about 25% of the mass of the parent body (Casanova et al., 1993; Lodders et al., 1993). The C_{Si}^{core}~ 2.1 wt% obtained from equation (4.2) is similar to that of the aubrite metals with Si content of ~2.1 wt% that equilibrated at the peak temperature of ~1635 K (Chapter 3). We have not used EL as a starting composition because of its heavier δ^{30}Si (-0.581 ± 0.024‰) compared to aubrites (-0.599 ± 0.048‰). Based on the findings of our previous study (Chapter 3), we concluded that as Si alloys with Fe-metal, δ^{56}Fe becomes progressively lighter. Using the correlation between the Si content (wt %) and δ^{56}Fe (Chapter 3), the δ^{56}Fe of the AuPB core is calculated to be ~0.020‰. Therefore, the AuPB core should have δ^{56}Fe ~ 0.020‰ and δ^{30}Si ~ -3.457‰. Now, using the average elemental composition of aubrite metals that equilibrated at the peak T (Chapter 3) and the Fe isotope equilibration factor $\Delta^{56}Fe_{metal\text{-}silicate} = \frac{3.85\times10^{4}(X_{sub})+7.44\times10^{4}}{T^{2}}$ (Elardo et al., 2019), we can calculate the $\delta^{56}Fe_{mantle}$ of the AuPB using the following mass balance equation

$$\delta^{56}\mathrm{Fe}_{\mathrm{mantle}} = \delta^{56}\mathrm{Fe}_{\mathrm{EC}} - \mathrm{f}_{\mathrm{Fe}}^{\mathrm{core}}(\Delta^{56}\mathrm{Fe}_{\mathrm{metal-silicate}}) \quad (4.4)$$

where $\mathrm{f}_{\mathrm{Fe}}^{\mathrm{core}}$ = 0.9854 is calculated from equation (2) using $\mathrm{C}_{\mathrm{Fe}}^{\mathrm{mantle}}$= 0.452 wt% based on a combined FeO and FeS content in aubrites (Keil, 2010), $\mathrm{C}_{\mathrm{Fe}}^{\mathrm{core}}$= 91.21 wt% (Chapter 3) and $\frac{\mathrm{M}_{\mathrm{mantle}}}{\mathrm{M}_{\mathrm{core}}} = \frac{0.75}{0.25}$. So, using a $\delta^{56}\mathrm{Fe}_{\mathrm{EC}}$ ~ 0‰, we calculate a $\delta^{56}\mathrm{Fe}_{\mathrm{mantle}}$ = −0.160±0.066‰. To account for the effect of 'missing' enstatite-plagioclase basalts (Wilson and Keil, 1991) on the $\delta^{56}\mathrm{Fe}_{\mathrm{mantle\ source}}$ (calculated above) and $\delta^{56}\mathrm{Fe}_{\mathrm{residue}}$ (aubrites), we use the following formula (Craddock et al., 2013),

$$\delta^{56}\mathrm{Fe}_{\mathrm{residue}} - \delta^{56}\mathrm{Fe}_{\mathrm{mantle\ source}} \approx -\mathrm{F}\,(\Delta^{56}\mathrm{Fe}_{\mathrm{melt-solid}}) \quad (4.5)$$

where F is the degree of melting which is 7−20% (Chapter 3) and $\Delta^{56}\mathrm{Fe}_{\mathrm{melt-solid}}$= 0.053 ±0.017 in Fe^{3+}-free systems (Elardo and Shahar, 2017; Elardo et al., 2019). The $\delta^{56}\mathrm{Fe}_{\mathrm{residue}}$ is calculated to range from −0.168‰±0.068‰ (for an average 13.5% partial melting) which overlaps with the δ^{56}Fe of the main group aubrites (− 0.135±0.062‰; Wang et al., 2014b). Based on all the calculations done above, it seems likely that a combined δ^{30}Si–δ^{56}Fe can be used to trace core formation and partial melting (Fig. 4.1).

4.4.1.2 Aubrite metals

In order for the δ^{30}Si–δ^{56}Fe of aubrites to be the result of core formation and partial melting, the AuPB core with an estimated $\delta^{56}\mathrm{Fe}$ ~ 0.020‰ and $\delta^{30}\mathrm{Si}$ ~ −3.457‰ should be identified. In Chapter 3, metals NC9 and ME1−4 from Norton County and Mount Egerton aubrites possessed the highest Si wt%, equilibration temperature and $\delta^{56}\mathrm{Fe}$ ~0.02‰. However, their $\delta^{30}\mathrm{Si}$ ranges between −6.155 ±

0.029‰ and −6.670 ± 0.090‰ (this study). The $\delta^{30}Si$ of aubrite metals has previously only been measured by Ziegler et al., 2010 who reported similar values ranging between −5.93 ± 0.16‰ and −6.62 ± 0.28‰ for metals from Norton County and Mount Egerton.

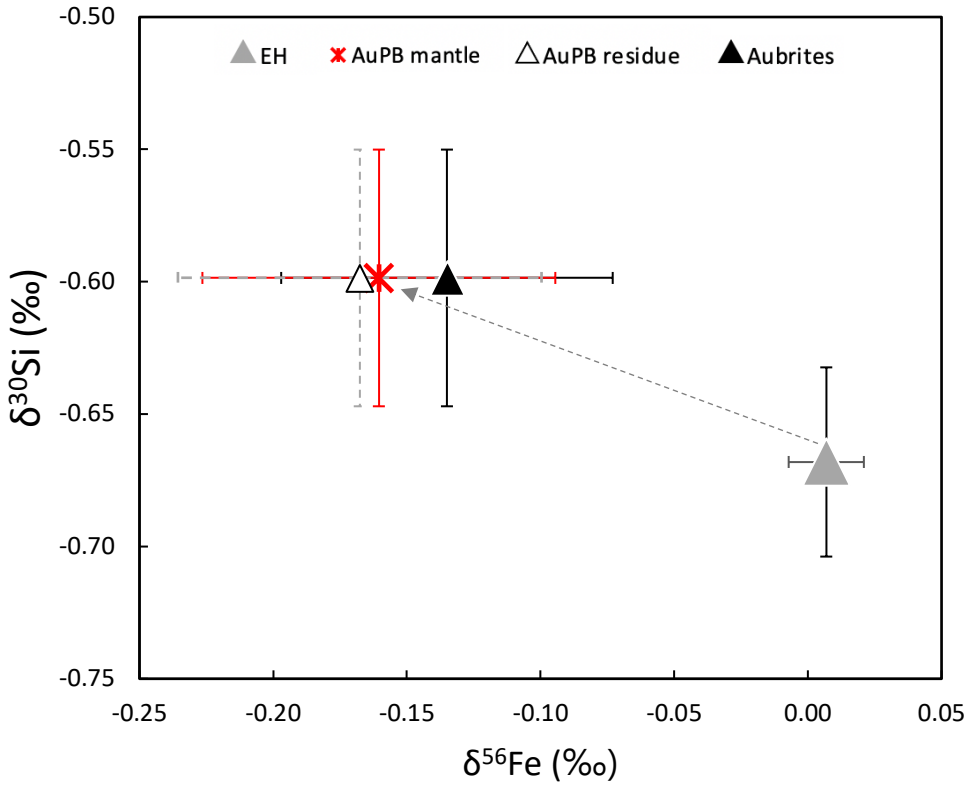

Figure 4.1. $\delta^{30}Si$ vs. $\delta^{56}Fe$ of EH chondrites and aubrites. The separation of a Si-bearing metallic core on a parent body of an EH-like composition (Armytage et al.,2011; Chakrabarti and Jacobsen, 2010; Fitoussi et al., 2009; Georg et al., 2007; Fitoussi and Bourdon, 2012; Savage and Moynier, 2013; Zambardi et al., 2013; Sikdar and Rai, 2020; Wang et al., 2014b) results in the formation of the AuPB mantle whose $\delta^{30}Si$ and $\delta^{56}Fe$ is represented by the red star. The white triangle denotes the composition of the residue left behind after the removal of the 'aubrite basalts' and overlaps with the composition of the main group aubrites (Armytage et al.,2011; Georg et al., 2007; Savage and Moynier, 2013; Wang et al., 2014b) shown here by the black triangle (See text for details).

Ziegler et al. (2010) determined the equilibration temperature of Norton County and Mount Egerton to be 1130 ± 80 K and 1200 ± 80 K, respectively, and corresponding $\Delta^{30}Si_{silicate-metal}$ of 5.69 ± 0.30‰ and 5.675 ± 0.21‰. Subsequently,

Jordan et al., 2019 reported higher equilibration temperature of ~1415 K and ~1460 K for Norton County and Mount Egerton in order to explain the Fe isotope fractionation citing higher closure temperature for Fe isotopes compared to Si isotopes such that the Si isotope fractionation persisted to sub-solidus temperatures. Recently, Moynier et al. (2020) reported $\Delta^{30}Si_{silicate-metal}$ of 2.87 $\pm$ 0.20 ‰ at a temperature of 1530 $\pm$ 0.110 K for the Itqiy enstatite achondrite which suggests that the fractionation of Si isotopes during metal-silicate equilibration on the Itqiy parent body did not persist up to sub-solidus temperatures as proposed by Jordan et al., 2019 for the aubrite parent body.

We do not observe a correlation between the $\delta^{30}Si$ and Si wt% of the aubrite metals (Fig. 4.2a) as we did for $\delta^{56}Fe$ and Si wt% (Chapter 3, Fig. 3.1). Similarly, there seems to be no correlation between the $\delta^{30}Si$ and Si wt% of EC metals (Kadlag et al., 2019; Sikdar and Rai, 2020). Metals from the unbrecciated Mount Egerton aubrite, i.e., ME1−4, which have uniform Si content and equilibration temperatures, have similar $\delta^{30}Si$ values. However, metals from the brecciated Norton County aubrite (NC7−12), which are samples from various depths on the AuPB (Chapter 3), have variable Si wt% and $\delta^{30}Si$ values. We have previously shown that the Si content of aubrite metals is a function of equilibration temperature (T) which correlated well with the $\delta^{56}Fe_{metal}$ and $\Delta^{56}Fe_{metal-silicate}$ (Chapter 3). This, however, is not true for the $\delta^{30}Si_{metal}$ and $\Delta^{30}Si_{metal-silicate}$ of aubrite metals. It is possible that the impacts causing brecciation led to the redistribution of Si isotopes between the metal and silicates on the AuPB. Such impacts did not affect the Fe isotopes as the closure temperature for Fe isotopes is higher than that for Si isotopes (Jordan et al., 2019). Savage and Moynier (2013) observed that, in general, aubrite metals have lower Si wt% compared to EC metal and bulk aubrites have $\delta^{30}Si$ that is lighter than EC silicates. They suggested that a partial or total rehomogenization of Si on the AuPB had occurred, and isotopically light Si present in kamacite prior to differentiation had

since entered the non-magnetic phases—thereby driving the non-metallic phases to lighter compositions and by extension, rendered the metals with heavier $\delta^{30}\mathrm{Si}$ values. Such removal of light Si isotopes from the metals from some Norton County metals (NC7, 8, and 10) could account for their heavier $\delta^{30}\mathrm{Si}$ values.

When an EC-like parent body undergoes incomplete differentiation (Casanova et al., 1993), the residual metals that did not completely segregate into the AuPB core, equilibrated at temperatures corresponding to their depth of entrapment (Chapter 3). Accordingly, Si content of the aubrite metals readjusted according to the solubility of Si in metal at that temperature and in order to do so, possibly expelled lighter Si isotopes to the neighboring silicates. For example, since ME1−4 and NC9 equilibrate at greater depths and higher temperatures, they somewhat retain the high Si wt% (proportional to the equilibration temperature) and corresponding $\delta^{30}\mathrm{Si}$ value inherent from the EC metals. But precursors of metals such as NC7, 8, and 10 which equilibrate at shallower depths and lower equilibration T, probably expelled lighter Si isotopes to a greater extent in order to end up with the lower Si content corresponding to their equilibration depth and temperature. However, we are not able to explain the δ^{30}Si values of NC11 and NC12 which should have the highest $\delta^{30}\mathrm{Si}$ value based on their lowest Si content. To summarize, the Si isotopes of aubrite metals, especially from brecciated aubrites such as Norton County, should be not be used to infer Si isotopic fractionation factor. Although the unbrecciated Mount Egerton aubrite provides uniform $\Delta^{30}\mathrm{Si}_{\mathrm{silicate-metal}}$, the magnitude is similar to that in enstatite chondrites.

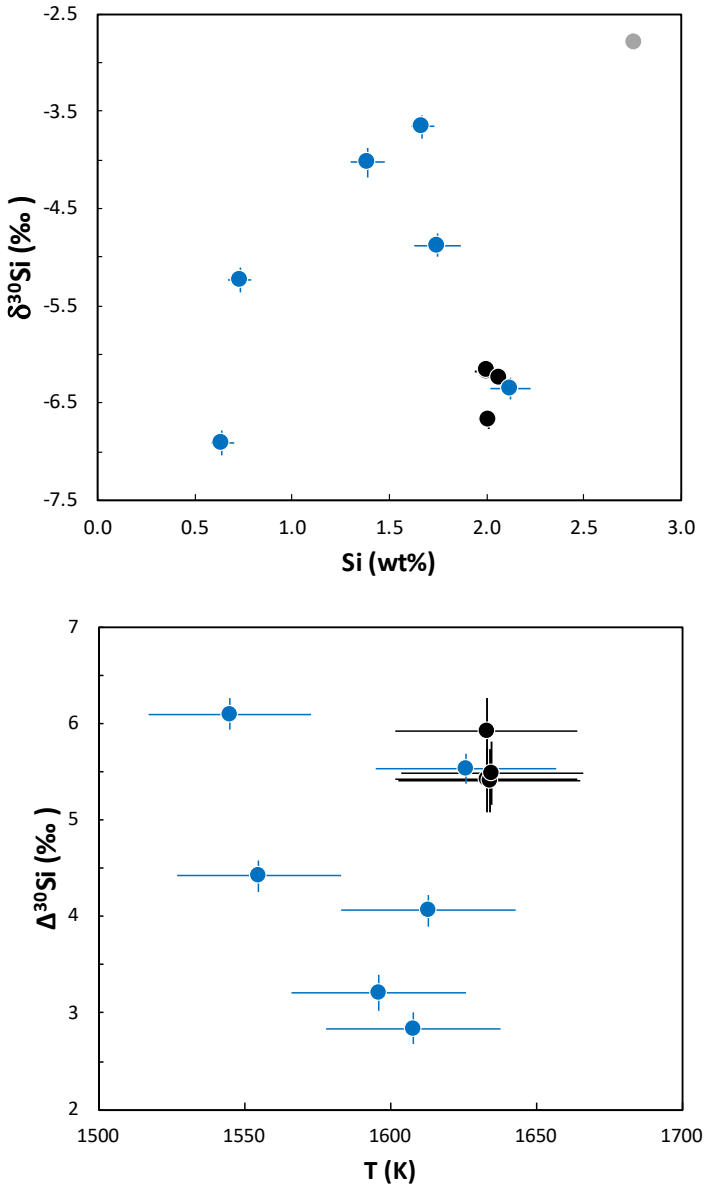

Figure 4.2. (a) $\delta^{30}Si$ versus Si content of aubrite metals and Horse Creek iron meteorite. (b) $\Delta^{30}Si_{silicate\text{-}metal}$ vs. calculated metal-silicate equilibration temperature (T in Kelvin). Blue symbols represent metals from brecciated aubrites (Norton County), black symbols show metals from non-brecciated aubrites (Mount Egerton) and grey symbol denotes Horse Creek iron meteorite. Equilibration temperatures are calculated in Chapter 3. All errors are 2SE.

4.4.1.3 Horse Creek iron meteorite

Although Horse Creek is classified as an anomalous and ungrouped iron meteorite (Buchwald, 1975), the presence of lamellar inclusions of perryite and up to

2.8 wt % Si suggests similarities with aubrite metals. In fact, Horse Creek was suggested to represent the core of the AuPB (Watters and Prinz, 1980). However, the chondritic abundance of siderophile elements were interpreted to suggest that they do not represent the core of the AuPB (Casanova et al., 1993). Nonetheless, δ^{56}Fe = 0.025 $\pm$ 0.015‰ of Horse Creek is somewhat similar to that predicted according to the mass balance calculation in Section 4.1.1.1. However, δ^{30}Si = -2.794 ± 0.083‰ is heavier than the -3.457‰ predicted for the AuPB core in Section 4.1.1.1. But the heavy δ^{30}Si could be attributed to the higher Si content of Horse Creek iron meteorite. Therefore, the δ^{30}Si and δ^{56}Fe of Horse Creek can be explained by isotopic fractionation associated with segregation of a Si-bearing metallic core to form an aubritic silicate mantle on a parent body with an EC-like starting composition. For $\delta^{30}Si_{HorseCreek} = -2.794$‰, $\delta^{30}Si_{EH} = -0.668$‰, and $\delta^{30}Si_{aubrites} = -0.599$‰, we have calculated $f_{Si}^{core} \sim 0.031$ (using equation 4.2) which translates to $\frac{M_{mantle}}{M_{core}} \sim 3.12$ (using equation 4.3 where $C_{Si}^{mantle} = 27.3$ wt% as mentioned in Section 4.1.1.1 and $C_{Si}^{core} = 2.76$ wt% as measured for the Horse Creek iron meteorite). Based on equation 4.1, this corresponds to an equilibration temperature of ~1850 K which would indicate that Horse Creek probably did not originate on the main aubrite parent body as a such high temperature (i.e., above the threshold T of 1723 K) would have obliterated the thermal gradient recorded by the aubrite metals.

4.4.1.4 Silicon and iron isotope fractionation in ECs and aubrites

The difference in isotope fractionation factor, if any, between the metal and silicate in enstatite chondrites and aubrites could be interpreted as a result of isotopic equilibration are higher temperatures during differentiation processes on the AuPB. Based on published literature data on δ^{30}Si for metals and silicates from a

variety of enstatite chondrites (Kadlag et al., 2019; Sikdar and Rai, 2020), aubrites (Ziegler et al., 2010; Jordan et al., 2019, and Table 4.1), the $\Delta^{30}Si_{silicate-metal}$ is similar for both enstatite chondrites and aubrites, i.e., 5.53 ± 0.83‰ and 5.54 ± 0.16‰ respectively (Fig. 4.3a). Such similarity could be interpreted to indicate either (1) differentiation processes occurring on the AuPB did not induce significant Si isotope fractionation, (2) the closure temperature for Si isotope fractionation on the AuPB is low such that the magnitude of $\Delta^{30}Si_{metal-silicate}$ is comparable to that observed in enstatite chondrites, or (3) metals in aubrites do not record the $\Delta^{30}Si_{metal-silicate}$ expected to explain the formation of aubrites by differentiation processes on an EC-like parent body. On the other hand, $\Delta^{56}Fe_{metal-silicate}$ is higher for enstatite chondrites (0.26 ± 0.08‰) than that for aubrites (0.07 ± 0.02‰) (Fig. 4.3b). This suggests that the higher temperature attained during differentiation processes on the AuPB were able to fractionate Fe isotopes between metals and silicates and therefore, result in a smaller $\Delta^{56}Fe_{metal-silicate}$ in aubrites. We also demonstrated the decrease in $\Delta^{56}Fe_{metal-silicate}$ with increasing equilibration T in our study of the $\delta^{56}Fe$ of metals from a variety of aubrites (Fig. 2.2b) as opposed to the lack of correlation between $\Delta^{30}Si_{silicate-metal}$ and equilibration T (Fig. 4.2b).

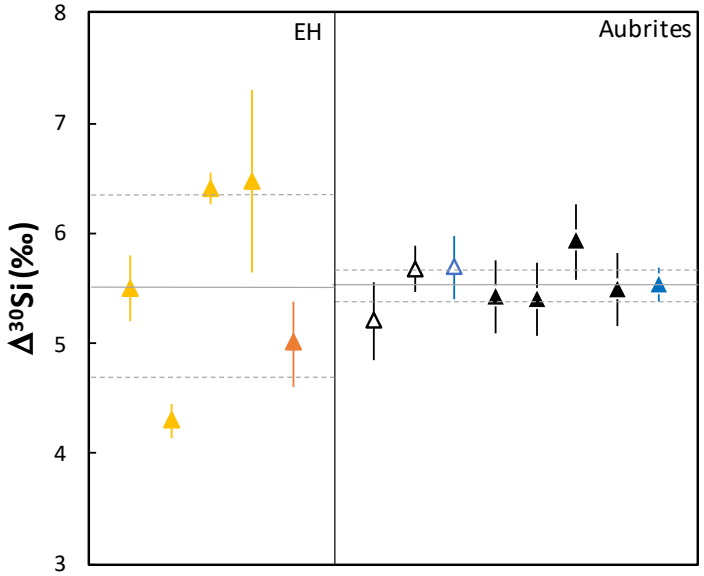

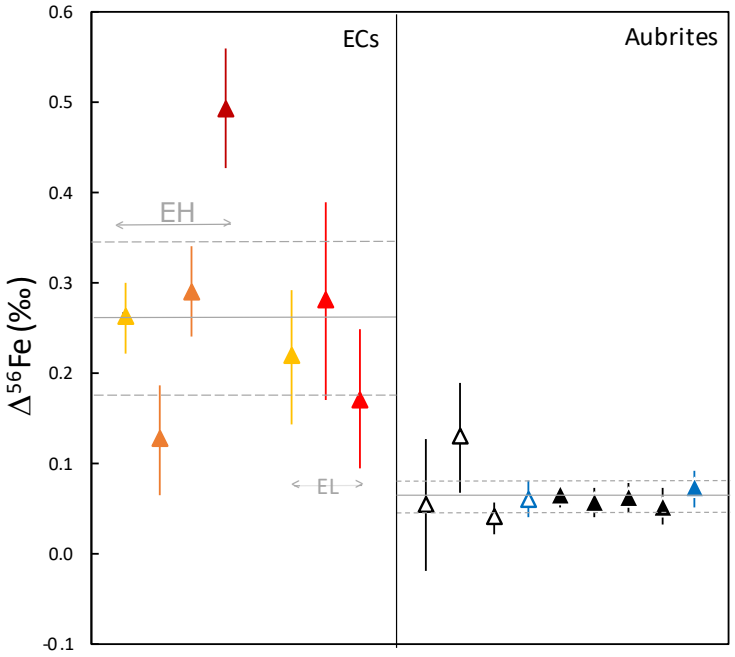

Figure 4.3. (a) $\Delta^{30}Si_{silicate-metal}$ of ECs and aubrites, (b) $\Delta^{56}Fe_{metal-silicate}$ of EH and aubrites. Symbols of different colors for ECs represent different petrographic grades: yellow-3, orange-4, maroon-5, and red-6. Blue symbols represent metals from brecciated aubrites (Norton County) and black symbols show metals from non-brecciated aubrites (Mount Egerton). All $\Delta^{30}Si_{silicate-metal}$ and $\Delta^{56}Fe_{metal-silicate}$ data for ECs are from published literature (Kadlag et al, 2019; Sikdar and Rai, 2020; Wang et al., 2014b). Open symbols for aubrites are from published literature (Zeigler et al., 2010; Wang et al., 2014b; Jordan et al., 2019) while solid symbols for aubrites are from Chapter 3 ($\Delta^{56}Fe_{metal-silicate}$) and Chapter 4 ($\Delta^{30}Si_{silicate-metal}$). Note that the solid symbols for aubrites represent the $\Delta^{30}Si_{silicate-metal}$ or $\Delta^{56}Fe_{metal-silicate}$) for metals that equilibrated at the highest equilibration T (i.e., NC9 and ME1–4).

4.4.1.5 'Missing' aubrite basalts

The formation of aubrites as a result of melting and fractionation of EC-like starting material warrants the formation of enstatite-plagioclase basalts complementary to aubrites (Wilson and Keil, 1991). The absence of such aubrite basalts in the meteorite record has been attributed to volatile-enabled, explosive volcanism on the surface of low-gravity asteroids (Wilson and Keil, 1991). The Fe and Si isotope composition of these 'missing' aubrite basalts can be calculated using the following formula from Craddock et al., 2013,

$$\delta^{56}Fe_{melt} - \delta^{56}Fe_{mantle\ source} \approx (1 - F) \times (\Delta^{56}Fe_{melt-solid}) \quad (4.6)$$

where $\delta^{56}Fe_{melt}$ is $\delta^{56}Fe_{AuPB\ basalt}$, $\delta^{56}Fe_{mantlesource} = -0.160 \pm 0.066‰$) calculated using equation 4.4, F = avg. 13.5 %, and $\Delta^{56}Fe_{melt-solid} = 0.053 \pm 0.017‰$).

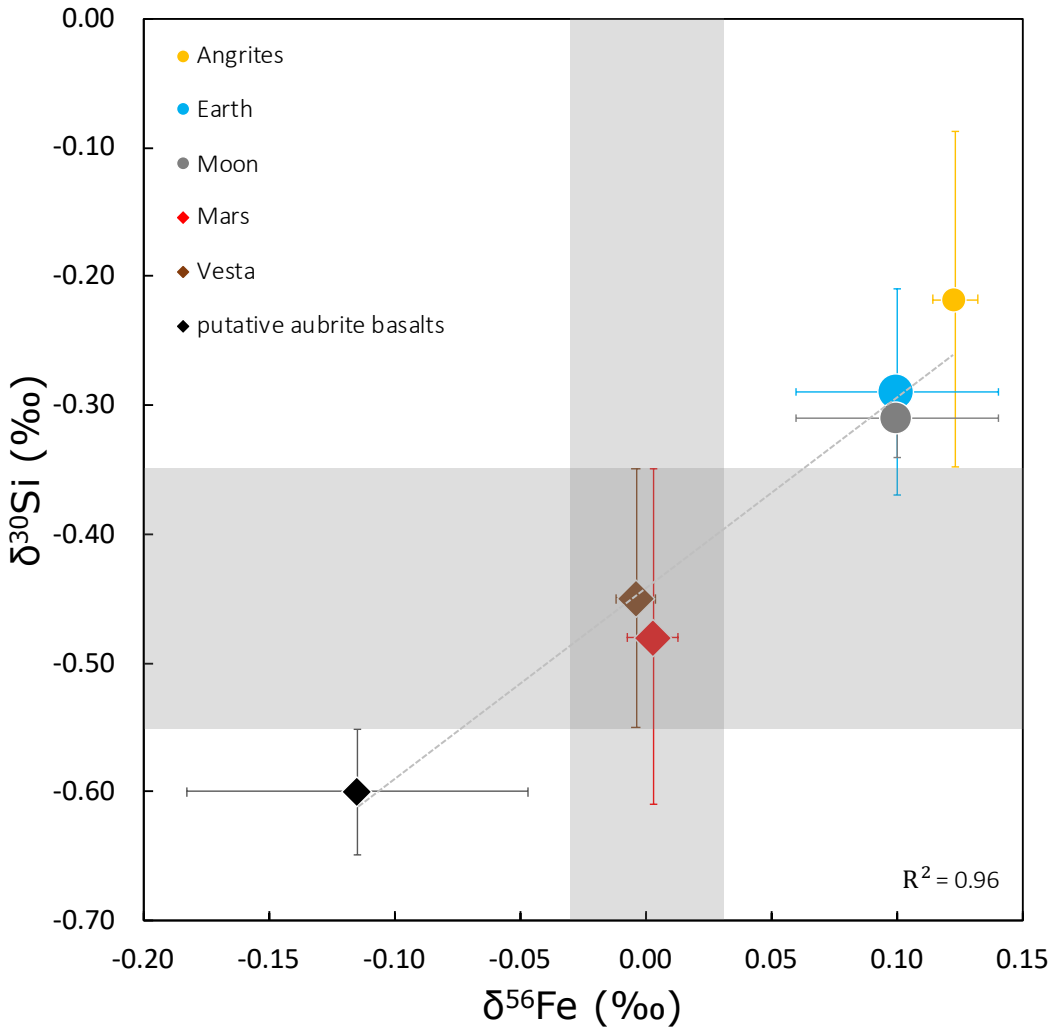

Figure 4.4. $\delta^{30}Si$ vs. $\delta^{56}Fe$ plot of planetary basalts. The isotopic composition of aubrite basalts has been calculated based on the mantle partial melting of the aubrite parent body post core formation (See Section 4.4.1.5 for details). The horizontal grey bar represents the $\delta^{30}Si$ (avg$\pm$2SD) of the ordinary and carbonaceous chondrites. The vertical grey bar represents the $\delta^{56}Fe$ (avg$\pm$2SD) of enstatite, ordinary, and carbonaceous chondrites. Isotope data for chondrites and basalts from Mars, Vesta, Moon, angrites, and Earth are from Wang et al., 2012; Teng et al., 2013; Poitrasson et al., 2019; Savage et al., 2014; Georg et al. (2007); Armytage et al. (2011); Dauphas et al. (2015); Craddock and Dauphas (2011); Fitoussi et al. (2009); Chakrabarti and Jacobsen (2010); Zambardi et al. (2013); Savage and Moynier (2013); Pringle et al. (2013); Pringle et al. (2014).

Therefore, $\delta^{56}Fe_{\text{AuPB basalt}}$ is possibly -0.114 ± 0.068‰. The $\delta^{30}Si$ remains constant as mantle partial melting to form basalts is associated with limited Si isotope fractionation (Savage et al., 2010; 2011; 2014). When the isotope composition of the putative aubrite basalt is plotted in the $\delta^{30}Si-\delta^{56}Fe$ diagram along with other planetary basalts (Fig. 4.4), a linear correlation is observed. Although aubrite basalts plot along the trendline formed by various planetary materials, the correlated $\delta^{30}Si$-$\delta^{56}Fe$ composition does not reflect volatile depletion processes as was suggested by Sossi et al., 2016a and b for other planetary basalts. Enrichment of light isotopes of Fe (except in bulk Shallowater (Wang et al., 2014b)) and Zn (Moynier et al., 2011b) of bulk aubrites rules out the role of evaporation in altering the isotopic composition of aubrites, which should enrich the target in heavier isotopes of the vaporizing element. This then leads to the next question: does the $\delta^{30}Si-\delta^{56}Fe$ correlation of planetary basalts (other than the putative aubritic basalts) reflect volatilization processes (Sossi et al., 2016a and b; Hin et al., 2017; Young et al., 2019) or is the signature of core formation followed by partial melting of the mantle (Elardo and Shahar, 2017; Elardo et al., 2019)?

4.4.2 Angrites

Angrites are meteorites of basaltic composition which record some of the earliest igneous activity in the Solar System (Keil, 2012). Angrites are enriched in the heavy isotopes of Mg (Sedaghatpour and Teng, 2016; Hin et al., 2017), Fe (Wang et al., 2012) and, Si (Pringle et al., 2014; Dauphas et al., 2015) compared to chondrites. Although such heavy isotope enrichment has been attributed to volatile depletion processes due to impact-induced magma oceans (Hin et al., 2017), the small size of the angrite parent body (APB) could not have undergone the vapor loss required to reconcile the offset of isotope composition (See Extended Data Figure 4 of Hin et al., 2017), even in a Grand Tack scenario (See Extended Data Figure 7 of

Hin et al., 2017). Similarly, as with basalts from Mars and Vesta, Young et al. (2019)'s model of vaporization from magma oceans generated due to ^{26}Al decay is unable to explain the δ^{25}Mg and δ^{30}Si of angrites.

Alternately, the heavy δ^{25}Mg can be due to the preponderance of clinopyroxene over orthopyroxene and/or olivine (Sedaghatpour and Teng, 2016) due to olivine fractional crystallization or olivine residue left behind during partial melting (Young et al., 2019) or heavy δ^{30}Si due to elevated Mg/Si inherited from nebular processes (Dauphas et al., 2015). The extreme depletion in moderately volatile elements and alkalis in angrites (Mittlefehldt, 2014) has been attributed to accretion from volatile-depleted material due to incomplete condensation from the solar nebula (e.g., Hans et al., 2013; Sanborn et al., 2015). In this case, the δ^{30}Si of angrites could have potentially sampled the refractory-rich, high Mg/Si composition inherited from the nebula (Dauphas et al., 2015) which would explain its heavy δ^{30}Si. Fractionation of Si isotopes due to sequestration of Si in the core (Ziegler et al., 2010) of the APB is unlikely due to its small size (Dauphas et al., 2015), low P, T and, fO_2 (ΔIW-1) (Righter et al., 2008; Shirai et al., 2009; Steenstra et al., 2017).

The formation of a core on the APB is reflected in its siderophile element depletion (Righter et al., 2008; Shirai et al., 2009; Steenstra et al., 2017), paleomagnetic evidence for an early core dynamo (Weiss et al., 2008) and, Hf–W systematics (Kleine et al., 2012). After formation of the core under relatively reduced conditions (ΔIW-1 to -1.4) (Righter et al., 2008; Shirai et al., 2009; Steenstra et al., 2017), melting of the APB mantle under oxidizing conditions (ΔIW$+1$ to $+2$), due to oxidation and degassing of a C-bearing phase, results in the formation of angrites (Righter et al., 2008; Shirai et al., 2009). Therefore, fractionation of Fe isotopes during core formation followed by partial melting under high fO_2 on the APB is a possibility. Additionally, volatile (including H_2O) accretion from beyond the snow line (Sarafian et al., 2017 a; b) could have further resulted in the heavy δ^{56}Fe of angrites.

In order to calculate the magnitude of Fe isotope fractionation in angrites during core formation and partial melting, we adopt the same set of formulae mentioned above. The mass of the core of the APB depends on the core composition such that $Fe_{80}Ni_{20}$ and $Fe_{70}Ni_{20}S_5C_5$ core result in core mass of 14±7% and 21±8%, respectively (Steenstra et al., 2017). So, using C_{Fe}^{mantle} = 15.68 wt% (Keil et al., 2012), C_{Fe}^{core} = 80 wt% and, $\frac{M_{mantle}}{M_{core}} = \frac{86}{14}$ in equation (4.2), we derive f_{Fe}^{core} = 0.4537. Next, in equation (4.3), using $\delta^{56}Fe_{chondrites}$ ~ 0‰ and $\Delta^{56}Fe_{metal-silicate}$ = 0.144 (for T=2073K; Shirai et al., 2009) we calculate the $\delta^{56}Fe_{mantle}$ of the APB to be −0.065‰. Finally, using equation (4.5), F=0.15 (Mikouchi et al., 2008), and $\Delta^{56}Fe_{melt-solid}$= 0.053±0.017‰ for Fe^{3+}-free systems, we calculate the $\delta^{56}Fe_{angrites}$ = −0.020‰. For the purpose of these calculations, we assume that the APB is an Fe^{3+}-free system because although in the prevailing fO_2 during angrite formation might have resulted in the formation in minor Fe^{3+} (Keil, 2012 and references therein), but not enough to fractionate isotopes based on the correlation between the $\delta^{56}Fe$ and $\sum Fe^{3+}/Fe_{total}$ (Dauphas et al., 2014). Similarly, using a core composition of $Fe_{70}Ni_{20}S_5C_5$ and mass of 21±8% (Steenstra et al., 2017); we calculate $\delta^{56}Fe_{angrites}$ = −0.048‰. These calculated values for $\delta^{56}Fe_{angrites}$ are distinctly lighter than the measured $\delta^{56}Fe_{angrites}$= 0.123±0.010‰. This discrepancy can be attributed to the multi-stage core formation on the APB (Kleine et al., 2012). Additionally, although partial melts of a devolatilized CV composition at ΔIW+1 to +2 resemble angrites (Jurewicz et al., 1993), the $\Delta^{17}O$, $\varepsilon^{54}Cr$, $\varepsilon^{50}Ti$ values for angrites provide evidence for an inner solar system origin (Warren, 2011). Thus, based on the isotope anomalies, a CV-like starting composition is not appropriate for angrites. However, core formation models based on siderophile elements depletion pattern in angrites assume a CV-like starting composition which could affect the mass and composition of the APB core and therefore, the value of calculated $\delta^{56}Fe_{angrites}$. Based on present

knowledge of the angrite parent body, the δ^{30}Si and δ^{56}Fe of angrites cannot be explained by core formation and partial melting processes.

4.4.3 Mars and Vesta

The incorporation of Si into the cores of Mars and Vesta is possibly precluded due to the relatively low temperatures and high oxygen fugacity conditions of core formation (Righter and Drake, 1996; Steenstra et al., 2016) compared to that required for partitioning of Si into metallic cores (Gessmann et al., 2001; Kilburn and Wood, 1997; Wade and Wood, 2005). Therefore, the absence of Si in the cores of Mars (e.g., Yoshizaki and McDonough, 2020 and references therein) and Vesta (Steenstra et al., 2016) can explain the chondritic δ^{30}Si of the SNC and HED meteorites respectively (Georg et al., 2007; Fitoussi et al., 2009; Chakrabarti and Jacobsen, 2010; Armytage et al., 2011; Zambardi et al., 2013). The vaporization models that enrich the target in heavier isotopes of the vaporizing element (e.g., Young et al., 2019) are unable to explain the chondritic δ^{30}Si of Mars and Vesta.

Similarly, the chondritic δ^{56}Fe composition of meteorites from Mars and Vesta has been attributed to different accretion mechanisms wherein Earth, Moon, and angrite parent body experienced a loss of lighter Fe isotopes due to high-energy impacts while the Mars, Vesta, and the chondrites accreted through runaway growth (Poitrasson et al., 2019). Sossi et al. (2016a, b) propose that non-depletion of Fe from Mars and Vesta helps preserve their chondritic δ^{56}Fe. Alternatively, the chondritic δ^{56}Fe composition of meteorites from Mars and Vesta have been explained by formation of a Ni-S-bearing metallic core to form isotopically light silicate mantle which is followed by partial melting of their respective mantles (Elardo and Shahar, 2017; Elardo et al., 2019). Therefore, it is possible to explain the chondritic δ^{30}Si of Mars and Vesta due to the absence of Si in their cores whereas their chondritic δ^{56}Fe is possibly a result of core formation followed by partial melting.

4.4.4 Moon

The similarities in nucleosynthetic anomalies such as $\Delta^{17}O$, $\varepsilon^{50}Ti$, and $\varepsilon^{54}Cr$ between Earth and the Moon have been instrumental in putting constraints on the Moon forming mechanism and the isotopic composition of the impactor, Theia (Meier et al., 2014 and references therein). For instance, according to the canonical Giant Impact model (Canup and Asphaug, 2001), the Moon must derive most of its material from Theia which indicates that Theia must be isotopically similar to proto-Earth. In the likelihood that Theia is not isotopically similar to proto-Earth, a mechanism for post-impact, vapor-phase, isotopic re-equilibration and homogenization has been proposed (Pahlevan and Stevenson, 2007; Pahlevan et al., 2011). However, if the constraints of angular momentum are removed, then the Moon can derive significantly from the proto-Earth as is demonstrated by the hit-and-run model (Reufer et al., 2012), impact-fission model (Cúk and Stewart, 2012), and merger model (Canup, 2012). In an attempt to provide compositional constraints on Theia, Meier et al. (2014) suggested that Theia possessed an Earth-like (enstatite chondrite, aubrites, or NWA 5400) isotopic composition. An EC-like, i.e., reduced Theia has also been supported to explain the geochemical and isotopic characteristics of Earth and the Moon (Wade and Wood, 2016; Akram and Schönbächler, 2016; Dauphas et al., 2014b; Desch and Robinson, 2019). Additional evidence for isotopically similar Theia and proto-Earth comes from numerical simulations wherein the authors invoke a 'primordial compositional similarity' which posits that composition of giant impactors are statistically more likely to be similar to their target-planets, i.e., a large fraction of the planet-impactor pairs has almost identical compositions (Mastrobuono-Battisti et al., 2015).

Since terrestrial basalts faithfully record the $\delta^{30}Si$ of their mantle sources due to limited fractionation of Si isotopes during partial melting (Savage et al., 2010; Savage et al., 2014), mare basalts can be considered to be representative of the

bulk silicate Moon, BSM (Savage et al., 2014). The similarity in Si isotopes between the bulk silicate Earth (BSE) and BSM has been interpreted to reflect the homogenization of Si isotopes in the aftermath of a Giant Impact (Armytage et al., 2012; Fitoussi and Bourdon, 2012; Zambardi et al., 2013). However, in order to explain the hydrogen systematics of lunar samples, Desch and Robinson (2019) preclude models that homogenize isotopes effectively, suggest an enstatite chondrite-like Theia that is isotopically similar to Earth, and invoke sequestration of Si in the cores of proto-Earth and Theia that led to their similar δ^{30}Si (~ –0.29‰) which is reflected in the δ^{30}Si of the Moon.

Contrary to the well-constrained δ^{30}Si of BSM, δ^{56}Fe of the Moon is much more debated (e.g., Poitrasson et al., 2004; Wang et al., 2015; Sossi and Moynier, 2017; Dauphas et al., 2017, Elardo and Shahar, 2017; Elardo et al., 2019). The variations in the δ^{56}Fe of different lithological units, viz. low-Ti basalts, high-Ti basalts, highland rocks have been attributed to the heterogeneity of the mantle sources (Poitrasson et al., 2004; Weyer et al., 2005; Liu et al., 2010; Sossi and Moynier, 2017). Recently, Poitrasson et al., 2019 compiled high precision Fe isotope composition of Apollo samples after excluding meteorites of lunar origin due to uncertainties associated with location of origin, shock modification, and potential terrestrial weathering. Assuming no Fe isotope fractionation occurs during either core formation and partial melting, Poitrasson et al. (2019) propose a ~0.1‰ for the bulk Moon based on mare basalts and highland rocks (with >10% modal pyroxene) which they attribute to vaporization of light Fe isotopes during the Moon-forming impact (Poitrasson et al., 2004; Poitrasson, 2007; Poitrasson et al., 2019). Based on Mg, Ti, and Fe isotopes, Dauphas et al., 2017 suggested that the low-Ti mare basalts provide the best estimate for the BSM. On the other hand, Sossi and Moynier, 2017 suggest that rocks from the lunar highlands Mg suite reflect the δ^{56}Fe of the bulk Moon. It is to be noted that the δ^{56}Fe of lunar highland rocks and low-Ti basalts were found be

indistinguishable (Poitrasson et al., 2019). On the contrary, Elardo et al. (2019) and Elardo and Shahar (2017) considered the Apollo 15 volcanic green glass to be the most primitive and relatively unfractionated mantle melt. The δ^{56}Fe of the volcanic green glass was explained by the partial melting of the green glass mantle source region (potentially the best estimate of the BSM) which itself was the result of equilibration between a silicate mantle and the Ni-S-bearing metallic core (Elardo and Shahar, 2017; Elardo et al., 2019).

4.4.5 Earth

The δ^{56}Fe of BSE is chondritic (Weyer et al., 2005; Dauphas et al., 2009; Teng et al., 2013; Craddock et al., 2013; Dauphas et al., 2017). Experimental data suggest that under the conditions of Earth's core formation, i.e., at the P and T at the base of the magma ocean, the $\Delta^{56}\mathrm{Fe}_{\mathrm{metal-silicate}}$ is diminished (Shahar et al., 2016; Elardo and Shahar, 2017; Elardo et al., 2019; Liu et al., 2017) such that Earth's core formation is associated with negligible Fe isotope fractionation. However, some studies favor a super-chondritic BSE (δ^{56}Fe ~ 0.1‰) citing evaporation during the Moon-forming giant impact (e.g., Poitrasson et al., 2004; Poitrasson et al., 2019), nebular or accretionary volatile depletion (Sossi et al., 2016a); fractionation between metallic Fe and mantle minerals at ultra-high pressures (Polyakov, 2009) or lower mantle disproportionation of Fe^{2+} into Fe^{0} and Fe^{3+} during perovskite crystallization (Williams et al., 2012).

Discrepancy of δ^{30}Si and Mg/Si between ECs and BSE has either precluded the former from being the starting composition for Earth (Fitoussi and Bourdon, 2012) or necessitated the sequestration of enormous and unrealistic quantities of Si in the Earth's core during equilibration at the base of a magma ocean (Fitoussi et al., 2009; Armytage et al., 2011). Even when a continuous core formation model is used (Zambardi et al., 2013), an EC-like composition results in ~29 wt% Si in Earth's

core. This far exceeds the required presence of light elements in Earth's core to reconcile the density deficit (Birch, 1964). Alternatively, Young et al. (2019) posit a 15% loss of Si due to near-equilibrium evaporation from magma oceans on ~700 km planetesimals of CI composition along with Si isotope fractionation associated with 3−6 wt% Si in Earth's core to explain the δ^{30}Si of BSE. They, however, emphasize that evaporation of EC-like planetesimals cannot explain the δ^{30}Si of Earth. The exclusion of an EC-like starting composition is contradictory to studies which suggest that Earth's precursors accreted from a feeding zone with a primarily EC-like composition (e.g., Javoy et al., 2010; Dauphas, 2017). In order to reconcile the heavy δ^{25}Mg of BSE compared to chondrites, Hin et al. (2017) proposed a 47% (by mass) vapor loss associated with a loss of 65% Si and 48% Fe during accretionary growth of planetesimals (irrespective of an EC- or CI-like starting composition). More recently, the similarity of δ^{30}Si between BSE and silicates from ECs (Sikdar and Rai, 2020) led the authors to suggest that ECs are viable precursors of Earth. However, they rule out core-mantle equilibration in a deep magma ocean as having a major role in shaping the δ^{30}Si of BSE in favor of nebular fractionation in reduced conditions followed by the vapor loss from a terrestrial magma ocean.

Here, we consider the heterogeneous, multistage core-formation model of Rubie et al. (2011) to test whether core-mantle equilibration within accreting planetesimals results in the δ^{30}Si (-0.29 ± 0.07‰; Savage et al., 2014) and δ^{56}Fe (0.025 ± 0.025‰; Craddock et al., 2013) of BSE. In their work, Rubie et al. (2011) model the formation of Earth's core via a series of impacts and metal-silicate equilibration between the growing Earth and accreting bodies. The differentiated Earth-forming impactors vary in mass from $0.01M_e$ to $0.1M_e$ (where M_e is the current mass of Earth) and oxidation state such that the initial ~ 67% of Earth's mass is highly reduced and the remaining ~33% is relatively more oxidized. We have used the temperature of equilibration (T_e), composition and mass fractions of core and

mantle of each impactor to calculate its δ^{30}Si and δ^{56}Fe. Similarly, using the aforementioned parameters, we further calculated the δ^{30}Si and δ^{56}Fe of the growing Earth at the end of each accretionary stage I_n. For the reduced impactors, an EC-like δ^{30}Si (−0.64‰ which is the average of EH and EL chondrites) and δ^{56}Fe (~0‰) has been adapted while for oxidized impactors, an OC/CC-like ^{30}Si (−0.47‰) and δ^{56}Fe (~0‰) has been used. At the end of 24 accretions (Rubie et al., 2011), the δ^{30}Si and δ^{56}Fe of BSE is −0.003‰ and −0.594‰ respectively. The calculated δ^{56}Fe of the terrestrial mantle here is similar, within error, to that measured using samples that potentially represent the terrestrial mantle (e.g., Craddock et al., 2013). Partial melting of the terrestrial mantle results in the formation of terrestrial basalts that are enriched in the heavy isotopes of iron (e.g., Weyer et al., 2005; Schoenberg and von Blanckenburg, 2006; Weyer and Ionov, 2007; Dauphas et al., 2009; Teng et al., 2013). However, the calculated δ^{30}Si is lighter than what is measured for terrestrial mantle (e.g., Savage et al., 2010). This discrepancy between the calculated (this study) and measured δ^{30}Si of the terrestrial mantle suggests that bulk Earth is probably not chondritic in terms of its Si isotope composition either due to 1) volatilization of the lighter Si isotopes (Hin et al., 2017; Moynier et al., 2020) or 2) a larger component of the high-temperature forsterite component characterized by high Mg/Si and δ^{30}Si (Dauphas et al., 2015). More recently, Morbidelli et al., 2020 posited that ~40% of Earth was constituted from a first-generation of refractory-rich planetesimals characterized by supra-solar Al/Si and Mg/Si ratios. It is possible that this refractory-rich component with high Mg/Si ratio possessed heavy δ^{30}Si (Dauphas et al., 2015; Kadlag et al., 2019) and can account for the heavy δ^{30}Si of bulk silicate Earth.

4.5. Conclusions

1) The δ^{56}Fe and δ^{30}Si of aubrites can be attributed to the formation of a Si-bearing core followed by partial mantle of the silicate mantle on an EH-like parent body. Although the predicted δ^{56}Fe of the AuPB core is similar to that measured for Horse Creek iron meteorite, the δ^{30}Si of Horse Creek is heavier than predicted which indicates that the equilibration T of Horse Creek iron meteorite was ~1850 K which is not expected to occur on the AuPB. Nonetheless, if the Horse Creek iron meteorite were to represent the core of a distinct parent body with an EH-like composition, its δ^{30}Si could be a result of partitioning of Si into the core such that $f_{Si}^{core} \sim 0.031$ and $\frac{M_{mantle}}{M_{core}} \sim 3.12$.

2) The magnitude of Fe isotope fractionation between metal and silicate ($\Delta^{56}Fe_{metal-silicate}$) is higher in ECs than in aubrites, i.e., $(\Delta^{56}Fe_{metal-silicate})_{EH} < (\Delta^{56}Fe_{metal-silicate})_{aubrites}$. This suggests that metal-silicate equilibration at higher temperature in aubrites resulted in the fractionation of Fe isotopes. On the other hand, magnitude of Si isotope fractionation between silicate and metal ($\Delta^{30}Si_{silicate-metal}$) is more or less similar for EH and aubrites. Moreover, there is no correlation between the δ^{30}Si and Si content as well as $\Delta^{30}Si_{silicate-metal}$ and equilibration T of the aubrite metals, contrary to what was observed for δ^{56}Fe and Si content (Chapter 3). This is possibly reflective of post-core formation processes on the AuPB that affect the Si isotopes and not the Fe isotopes.

3) The calculated δ^{56}Fe and δ^{30}Si of the 'missing' aubrite basalts plot on the correlation line between δ^{56}Fe and δ^{30}Si of other planetary basalts. Therefore, we assessed whether core formation and partial melting can explain the δ^{56}Fe and δ^{30}Si of planetary basalts other than the putative aubrite basalts. Basalts from Mars and Vesta have chondritic δ^{56}Fe and δ^{30}Si which is characteristic of formation of Si-free cores followed by partial melting of the mantle. Similarly,

δ^{56}Fe and δ^{30}Si of the lunar basalts can be explained by core formation and partial melting without invoking the giant-impact induced vaporization of the lighter Fe and Si isotopes. The chondritic δ^{56}Fe of the terrestrial mantle can be acquired by core formation while the heavy δ^{30}Si required additional processes. Although volatilization is a probable cause, it is also possible that a first-generation of refractory-rich planetesimals possessing heavy δ^{30}Si were accreted to Earth. Similarly, we cannot explain the heavy δ^{56}Fe and δ^{30}Si of angrites by core formation and partial melting. Since, vaporization models are not able to reproduce the δ^{56}Fe and δ^{30}Si of angrites, it is likely that angrites represent a refractory-rich component with heavy δ^{30}Si. At present, we cannot conclude whether such refractory-rich material had heavy δ^{56}Fe as well. However, it is possible that the assumption of a CV-like starting material for angrites affects the determination of its core fraction and composition and therefore, affects the calculation of $\delta^{56}Fe_{angrites}$.

CHAPTER 5

COMBINED IRON AND SILICON ISOTOPE COMPOSITIONS OF BRACHINITES AND UNGROUPED ACHONDRITES: IMPLICATIONS FOR OXYGEN FUGACITY AND PARTIAL MELTING IN PLANETESIMALS

5.1 Introduction

Ungrouped achondrites are achondrites that have been characterized well enough to determine that they cannot be categorized under any established group of meteorites. The identification of numerous ungrouped achondrites which originate on distinct parent bodies provides an opportunity to understand the diversity of processes operating in the Solar System. Ungrouped achondrites sample parent bodies that have undergone different stages of differentiation (primitive to evolved), formed under various redox conditions, accreted and differentiated at various times relative to CAI formation, and originate both from the inner and outer Solar System. Therefore, it is imperative to understand the processes and conditions that control the formation mechanisms of parent bodies of ungrouped achondrites. Stable isotopic composition, such as Fe and Si isotope compositions, of such ungrouped achondrites can provide insights into the evolution of their parent bodies and test the validity of using stable isotopic compositions as tracers of differentiation.

Iron isotope composition (expressed as $\delta^{56}Fe$ which is the deviation in parts per thousand of $^{56}Fe/^{54}Fe$ ratio of the sample relative to the IRMM 524A standard) have the potential to trace the evolution of planetary and asteroidal bodies. Iron's ubiquity and variable oxidation states (0, +2, +3) in planetary reservoirs make it a powerful tracer of partial melting and oxygen fugacity (Williams et al., 2005; Williams et al., 2009; Weyer and Ionov, 2007; Dauphas et al., 2009; Sossi et al., 2012; Dauphas et al., 2014a). The $\delta^{56}Fe$ of whole-rock and mineral separates from mantle peridotites and pyroxenites correlate with indices of melt extraction and

oxidation (Williams et al., 2005; Weyer and Ionov, 2007). Using island arc basalts that formed by flux melting in the New-Britain Island arc, Dauphas et al., 2009 demonstrated that the degree of partial melting is correlated to their $\delta^{56}Fe$. Specifically, basalts with higher TiO_2 concentrations (a proxy for low degree of partial melting) have heavy $\delta^{56}Fe$ similar to MORBs (mid ocean ridge basalts) and OIBs (ocean island basalts) while basalts with low TiO_2 content (high degree of partial melting) have chondritic $\delta^{56}Fe$. Furthermore, Dauphas et al., 2009 invoked the equilibrium fractionation between Fe^{2+} and incompatible, isotopically heavier Fe^{3+} during mantle melting to explain the heavier $\delta^{56}Fe$ of MORBs and OIBs or lack thereof, to explain the chondritic $\delta^{56}Fe$ of martian and vestian basalts which formed at lower fO_2 conditions than those on Earth (Wadhwa, 2008). Subsequently, Dauphas et al., 2014a posited that only 1/3 of the Fe isotopic offset between MORBs and mantle peridotites could be explained by the isotopic fractionation factor derived from reduced partition function ratios of Fe^{2+} and Fe^{3+}. In silicate minerals, Fe is usually in 6-fold coordination while in basaltic melts, the effective coordination of Fe is ~ 5, with Fe^{3+} (Young et al., 2015 and references therein). Since, low coordination number facilitates the enrichment of heavier isotopes of an element, melts are expected to have heavier $\delta^{56}Fe$ compared to their source. For instance, the heavier $\delta^{56}Fe$ value of terrestrial basalt compared to mantle xenoliths, komatiites, boninites, and high degree partial melting island arc basalts (Weyer et al., 2005; Weyer and Ionov, 2007; Dauphas et al., 2009; Craddock et al., 2013; Teng et al., 2013) has been attributed to the partitioning of the incompatible Fe^{3+} to the melt as well as the lower co-ordination number of ~5 of Fe in basaltic melt compared to that of 6 in co-existing olivine and pyroxenes.

A change in the silicon isotopic composition (expressed as $\delta^{30}Si$ which is the deviation in parts per thousand of $^{30}Si/^{28}Si$ ratio of the sample relative to the NBS-28 standard) in response to partial melting is fairly constrained. Indistinguishable $\delta^{30}Si$

of terrestrial ultramafic and basaltic rocks from a wide variety of tectonic settings led to the conclusion that a limited Si isotope fractionation was associated with mantle partial melting to form basalts (Savage et al., 2014 and references therein). However, calculations using first principles (Grant, 1954) and density functional theory (Méheut et al, 2009) revealed control of degree of polymerization (increase in SiO_2) and network-forming cations (such as Al) in the silicate structure on the fractionation of Si isotopes. Using a variety of terrestrial igneous rocks from varied tectonic settings, Savage et al. (2011; 2013), observed an 'igneous array', i.e., a linear correlation between their $\delta^{30}Si$ values and SiO_2 content which is defined by $\delta^{30}Si$ (‰) = 0.0056 × SiO_2 (wt%) – 0.567. The caveat with samples adhering to the 'igneous array' involves that they must belong to equilibrium melt assemblages. Although initially not resolvable (Armytage et al., 2012), a similar correlation between the degree of polymerization (i.e., SiO_2 concentration and tectosilicate content) and $\delta^{30}Si$ was also observed for lunar samples ranging from basalts to granites and anorthosites (Poitrasson and Zambardi, 2015). Since, Si is not redox sensitive and has a single valence state (4+) in silicate melt, the $\delta^{30}Si$ of partial melts and residues is not expected to change with the redox of the sample. However, redox indirectly controls the $\delta^{30}Si$ of a sample such that under low fO_2 conditions, Si is incorporated into the metallic core, thereby forming a mantle (and consequently partial melts) with heavy $\delta^{30}Si$ compared to starting composition, usually assumed to be chondritic. Therefore, combined $\delta^{56}Fe$ and $\delta^{30}Si$ of achondrites have the potential to furnish information about their petrogenesis, redox, and degree of partial melting.

In this study, we report the $\delta^{56}Fe$ and $\delta^{30}Si$ values for ten ungrouped achondrites (GRA 06129, NWA 5297, Tafassasset, NWA 6926, NWA 6962, NWA 8777, NWA 10503, NWA 2976, NWA 8486, and NWA 11119) varying in their redox conditions, degree of melting, and origin in the inner versus outer Solar System. We also report the $\delta^{56}Fe$ and $\delta^{30}Si$ values of four brachinites for two reasons; (1) this is

the first study to report the $\delta^{30}Si$ of brachinites and (2) the ungrouped achondrite GRA 06129 is considered to be the partial melt complement of the residual brachinites and therefore, constitute a melt-residue pair to study the change in $\delta^{56}Fe$ and $\delta^{30}Si$ due to partial melting under oxidizing conditions. This study is an attempt to ascertain whether the $\delta^{56}Fe$ and $\delta^{30}Si$ of ungrouped achondrites can be used as tracers of differentiation processes.

5.2 Samples

The samples in this study include FeO-rich achondrites, i.e., those achondrites that formed under oxidizing conditions, such as brachinites (Eagles Nest, NWA 3151, NWA 4882, and Reid 013) and the ungrouped achondrites GRA 06129, Tafassasset, NWA 6926, NWA 6962, NWA 8777, NWA 10503, and NWA 2976. On the other end of the spectrum, FeO-poor and reduced achondrites such as NWA 8486 and NWA 11119 are also studied.

5.3 Methods

5.3.1 Thermodynamics calculation

For this study, we determined the equilibration temperature and oxygen fugacity of six samples; NWA 5297, Tafassasset, NWA 10503, NWA 8777, NWA 2976, and NWA 11119 using compositional data for appropriate mineral assemblages (Tables 5.1 – 5.4). Using compositional data of co-existing olivine, chromite, and orthopyroxene acquired from EPMA, we calculated the closure temperature and fO_2 for the achondrites NWA 5297 and NWA 8777 using the online version of the MELTS calculator (Olivine-spinel-orthopyroxene geothermometer-oxybarometer) (Sack and Ghiorso, 1991a and b). For the remaining four achondrites, viz., NWA 6962, NWA 10503, NWA 2796, and NWA 11119 that did not have all the three mineral

assemblages, we calculated the closure temperatures using the olivine-spinel and two-pyroxene geothermometers for appropriate mineral assemblages. Closure temperatures were calculated using the online version of the MELTS calculator (http://melts.ofm-research.org/CORBA_CTserver/Olv_Spn_Opx/index.php) for the olivine-chromite pairs (NWA 6962 and NWA 10503) and the QUILF program (Anderson et al., 1993) for the two-pyroxene mineral pairs (NWA 2976 and NWA 11119). The corresponding oxygen fugacity (fO_2) was determined at the calculated closure temperature for each mineral pair using the quartz-iron-fayalite (QIFa) buffer reaction (equations 5.1 and 5.2) for the olivine-chromite pairs and the quartz-iron-ferrosilite buffer reaction (QIFs) buffer reaction (equations 5.3 and 5.4) for the two-pyroxene pairs. The buffer reactions and their corresponding equations to calculate the fO_2 are as follows:

$$2Fe + SiO_2 + O_2\,(g) = Fe_2SiO_4. \quad (5.1)$$

$$\log(fO_2) = \log(a_{Fa}) - \log K_1 - 2\log(a_{Fe}) - \log(aSiO_2) \quad (5.2)$$

and

$$2Fe + 2SiO_2 + O_2\,(g) = 2FeSiO_3 \quad (5.3)$$

$$\log(fO_2) = 2\log(a_{Fs}) - \log K_2 - 2\log(a_{Fe}) - 2\log(aSiO_2) \quad (5.4)$$

The activities of fayalite (a_{Fa}) and ferrosilite (a_{Fs}) were calculated from the online MELTS Supplemental Calculator (http://melts.ofm-research.org/CalcForms/index.html) (Sack and Ghiorso, 1989; Hirschmann, 1991). The activity of Fe (a_{Fe}) of Fe-Ni metal was equal to the average mole fraction of Fe in the metal. The activity of silica ($aSiO_2$) is assumed to be 0.9 (Benedix et al., 2005) for all achondrites except for NWA 11119 where it is 1 due to the presence of a pure silica phase. The HSC 7.0 Chemistry Reaction Equation module was used to obtain the temperature dependent equilibrium constant (K). Each fO_2 was then referenced

to the iron-wüstite (IW) buffer, which was also determined using HSC Chemistry. All calculations were performed at a pressure of 1 bar which is a reasonable approximation for asteroids (Benedix et al., 2005; Gardner-Vandy et al., 2013; Schrader et al., 2017). Closure temperatures for each meteorite are error-weighted averages of at least six pairs of relevant mineral pairs and their uncertainties are approximately ±50 ℃ (1σ) for olivine-spinel temperatures (e.g., Benedix et al., 2005; Schrader et al., 2017), and are determined for each mineral pair directly by the QUILF program for two-pyroxene temperatures (from ±35 ℃ to ±65 ℃; 1σ). Similarly, fO_2 are averages of at least six pairs of minerals and errors are 1σ.

5.3.2 Sample digestion

To ensure low procedural blanks, all reagents used during the course of this work were obtained or prepared as follows. We obtained Suprapur sodium hydroxide monohydrate flakes ($NaOH.H_2O$). Hydrochloric acid (HCl) was distilled once from trace metal grade acid using the Savillex DST-1000 Acid Purification System. To purify water used for acid dilutions and chromatography, reverse osmosis (RO) water was passed through a Millipore Super-Q® water purification system (resistivity ~18 MΩ-cm) and a Millipore Milli-Q® water purification system with a 0.1 µm final filter (resistivity >18.2 MΩ-cm). About 20-100 mg of a fresh, interior piece of each meteorite was powdered using a boron carbide mortar and pestle. Thereafter, ~1mg homogenized powder of each sample was mixed with about ~200 mg $NaOH.H_2O$ flakes in a round-bottomed Teflon beaker. This 200:1 flux-sample mixture was heated on a hotplate at 250ºC for ~96 hours to ensure complete digestion. Details of this alkali fusion technique have been described in Chapter 2. After a fused cake was formed, appropriate volume of concentrated HCl and Milli-Q® water was added to make 10 ml final solution with pH of ~2.

5.3.3 Chromatographic purification of silicon and iron and measurement of isotopes

Solutions containing ~15 ug of Si and proportional concentration of other elements (including Fe), were loaded onto columns with 1.8ml of AG50W-X8 (200-400 mesh) cation exchange resin. Since Si occurs as neutral or negative ions, it is not exchanged on the cation exchange resin, facilitating its elution using incremental volumes of a total 15 ml of Milli-Q® water. The Si cut was acidified using concentrated HCl to make a final solution of 0.05 N HCl. Silicon yields were always better than 98.5%. Elements such as Fe exist as cations in the solution and are adsorbed onto the cation exchange resin. After elution of Si from the cation resin column into collection beakers, another column containing 1ml of AG1-X8 (200-400 mesh) anion exchange resin was placed under it. To elute the cations adsorbed on the cation exchange resin, 22 ml of 6N HCl was passed through it. In a 6 N HCl medium, Fe has low distribution co-efficient (K_d) for cation exchange resin. After being eluted from the cation exchange resin, Fe gets adsorbed on the anion exchange resin placed below. After this, the resin column with the cation exchange resin was removed and Fe separation procedure (modified after Arnold et al., 2004) was carried out. To separate Fe from the anion exchange resin, 24 ml of 6N HCl was passed to elute other cations, followed by 14 ml of 0.5 N HCl to elute Fe. The Fe cut was then dried down on a hot plate and brought up in 2% HNO_3. Iron column yields were always better than 99%. The remaining solution was made up into final solutions with an Fe concentration of 0.5 ppm and doped with 0.5 ppm NIST-Cu for measurement of Fe isotopes. The details of measurement of the Si and Fe isotopes have been described in previous chapters.

5.4 Results

5.4.1 Equilibration temperature and oxygen fugacity

The equilibration temperature and oxygen fugacity of the six samples calculated in this study (NWA 5297, NWA 6962, NWA 10503, NWA 8777, NWA 2976, and NWA 11119) have been presented in Table 5.5. The temperatures range between 673±50℃ (NWA 5297) and 1190±66℃ (NWA 11119). The meteorites also record a wide range of redox conditions ranging from ΔIW+0.35±0.33 (NWA 5297) to ΔIW−3.41±0.1 (NWA 11119). Amongst all the six samples studied here, NWA 5297 records the lowest equilibration T and highest fO_2 while NWA 11119 records the highest equilibration T and the lowest fO_2. The equilibration temperature and oxygen fugacity of the remaining eight samples have been reported from literature and are also presented in Table 5.5. Therefore, when considering all the 14 samples, the fO_2 spans ~5.4 log units from ΔIW+2 (GRA 06129) to ΔIW−3.41±0.1 (NWA 11119).

5.4.2 Silicon isotopes of achondrites

The Si isotope compositions of the achondrites are reported in Table 5.6. All but one brachinite (Eagle Nest) have similar δ^{29}Si (average = −0.268±0.019‰, 2SD) and δ^{30}Si (average = −0.511±0.021‰, 2SD). The brachinite Eagle Nest is distinct and has δ^{29}Si = −0.156±0.029‰ and δ^{30}Si = −0.291±0.022‰. The δ^{29}Si of the ungrouped achondrites range between −0.103±0.015‰ to −0.316±0.028‰ and the δ^{30}Si range between −0.213±0.052‰ to −0.552±0.018‰.

5.4.3 Iron isotopes of achondrites

The Fe isotope compositions of the achondrites are reported in Table 5.6. The δ^{56}Fe of brachinites range between 0.009±0.016‰ and 0.063±0.020‰ while the δ^{57}Fe range between 0.022±0.030‰ and 0.081±0.048‰. For the ungrouped

achondrites, the $\delta^{56}Fe$ have a wide range between -0.316 ± 0.020‰ and 0.077 ± 0.013‰ and the $\delta^{57}Fe$ range between -0.459 ± 0.040‰ and 0.097 ± 0.019‰.

Table 5.1. Representative compositions (in wt%) of mineral pairs used for calculation of equilibration temperature and oxygen fugacity using the olivine-spinel-orthopyroxene geothermometer (Sack and Ghiorso, 1991a and b)

Meteorite	**NWA 5297**			**NWA 8777**		
Oxide	olivine	pyroxene	chromite	olivine	pyroxene	chromite
SiO_2	37.52	53.97	0.16	37.42	53.85	0.04
CaO	bdl	1.89	0.05	0.06	1.65	0.09
TiO_2	bdl	0.26	3.21	bdl	0.14	0.97
Al_2O_3	bdl	0.26	4.66	bdl	1.22	16.88
Cr_2O_3	0.37	0.48	55.13	0.33	0.66	47.84
V_2O_3	bdl	nd	0.68	bdl	nd	0.40
FeO	26.47	16.18	32.35	26.06	16.08	26.06
Fe_2O_3	—	—	1.03	—	—	0.82
MnO	0.45	0.44	0.64	0.55	0.54	0.46
MgO	35.74	26.43	1.81	35.87	25.93	5.80
ZnO	bdl	nd	0.28	bdl	nd	bdl
Total	100.62	99.99	99.95	100.32	100.08	99.27

Table 5.2. Representative compositions (in wt%) of mineral pairs used for calculation of equilibration temperature and oxygen fugacity using the olivine-spinel geothermometer

Meteorite	**NWA 6962**		**NWA 10503**	
Oxide	olivine	chromite	olivine	chromite
SiO_2	34.83	0.06	37.14	0.06
CaO	0.45	0.06	0.08	0.05
TiO_2	bdl	2.35	bdl	5.11
Al_2O_3	bdl	14.84	bdl	9.01
Cr_2O_3	0.19	44.59	0.28	47.33
V_2O_3	bdl	0.80	bdl	0.83
FeO	38.58	30.15	27.84	32.10
Fe_2O_3	—	2.58	—	0.96
MnO	0.54	0.42	0.33	0.34
MgO	25.22	3.84	34.75	3.56
ZnO	bdl	bdl	bdl	bdl
Total	99.87	99.64	100.46	99.31

Table 5.3. Representative compositions (in wt%) of mineral pairs used for calculation of equilibration temperature using the two-pyroxene geothermometer and oxygen fugacity. lcp: low-Ca pyroxene; hcp: high-Ca pyroxene

Meteorite	**NWA 11119**		**NWA 2976**	
Oxide	lcp	hcp	lcp	hcp
SiO_2	56.57	53.06	47.95	48.72
CaO	2.52	17.26	4.61	15.55
TiO_2	0.15	0.45	0.49	0.78
Al_2O_3	0.90	1.72	0.64	1.19
Cr_2O_3	0.84	1.02	0.24	0.40
FeO	6.73	5.48	35.58	23.98
MnO	0.94	0.93	0.53	0.36
MgO	31.50	19.48	9.68	8.69
Total	100.16	99.49	99.73	99.75

Table 5.4. Representative compositions (in wt%) of metal used for calculation of oxygen fugacity

Meteorite	**NWA 6962**	**NWA 11119**	**NWA 2976**	**NWA 10503**
Element	metal	metal	metal*	metal
Fe	93.69	96.42	42.17	53.87
Ni	5.00	0.76	51.12	43.06
Co	0.37	0.15	0.62	1.78
Cr	bdl	0.01	bdl	bdl
S	bdl	0.96	1.70	0.02
P	bdl	bdl	bdl	bdl
Si	bdl	0.11	2.55	bdl
Total	99.06	98.41	98.16	98.73

metal*: In NWA 2976, metal occurrence was rare and often in close association with sulfides. Metal grains were about a few microns in size that led to mixed analyses from neighboring silicates or sulfides. If we eliminated S, Si, and Mg (0.83 wt% not shown here) and recalculated the total, the corresponding fO_2 is ΔIW-0.51±0.11 which is similar, within error, to ΔIW-0.44±0.11 calculated using the composition shown in Table 4.

For all the above analyses, standards used and detection limit (in wt%) for each element are as follows;
pyroxene: wollastonite for Ca (0.02) and Si (0.02), San Carlos augite for Al (0.02), Johnstown Hypersthene for Mg (0.02), rhodonite for Mn (0.02), chromite for Cr (0.02), FeO for Fe (0.04), and rutile for Ti (0.08);
olivine: San Carlos olivine for Si (0.02) and Mg (0.02), synthetic fayalite for Fe (0.04), Johnstown Hypersthene for Ca (0.02), chromite for Al (0.02), Ti (0.1), and Cr (0.02), rhodonite for Mn (0.02), vanadium for V (0.02), and ZnO for Zn (0.05);
chromite: Johnstown Hypersthene for Si (0.03) and Ca (0.02), FeO for Fe (0.04), chromite for Al (0.02) and Mg (0.03), San Carlos augite for Na (0.04), rhodonite for Mn (0.02), chromium for Cr (0.02), vanadium for V 0.02), ZnO for Zn (0.06), and rutile for Ti (0.08).

metal: Iron for Fe (0.04), nickel for Ni (0.04), cobalt for Co (0.02), chromite for Cr (0.01), troilite for S (0.02), schreibersite for P (0.03), and Johnstown Hypersthene for Si (0.02).

Table 5.5. Equilibration temperature and oxygen fugacity of achondrites in this study

Meteorite	Ref.	T (°C)	Method	ΔIW	Method
Eagles Nest	[2]	1047±9	[b]	−1.45±0.02	[b]
NWA 4882	[2]	1049±44	[b]	−1.21±0.04	[b]
		844±53	[c]	−1.82±0.01	[c]
Reid 013	[2]	1041±26	[b]	−1.16±0.02	[b]
		836±28	[c]	−1.04±0.01	[c]
NWA 3151	[3]	1054±27	[b]	−1.0±0.04	[b]
Tafassasset	[4]	937	[b]	−1.2	[b]
		1073	[c]	−1.0	[c]
NWA 5297	[1]	673±50	[a]	+0.35±0.33	[a]
NWA 6926	[5]	900	[b]	+1.47	[e]
		1050	[c]		
NWA 6962	[1]	1079±50	[b]	−1.02±0.01	[b]
NWA 8777	[1]	968±50	[a]	−1.44±0.33	[a]
NWA 10503	[1]	868±50	[b]	−0.98±0.03	[b]
GRA 06129	[6]	733 to 868	[a]	+2.0±0.5 to −0.1±0.5	[a]
		670±50	[c]		
		962	[d]	+1.1	[d]
NWA 2976	[1]	865±35	[c]	−0.44±0.11	[c]
NWA 8486	[7,8]	1180	[e]	−3.1±0.2	[f]
NWA 11119	[1]	1190±66	[c]	−3.41±0.1	[c]

[1]This study; [2]Crossley et al. (2020); [3]Gardner-Vandy et al. (2013); [4]Gardner-Vandy et al. (2012); [5]Hibiya et al. (2019) NWA 6926 is paired with NWA 6704; [6]Shearer et al. (2010); [7]Goodrich et al. (2017b) NWA 8486 is paired with NWA 7325; [8]Sutton et al. (2017).

[a] Equilibration temperature and oxygen fugacity calculated using the olivine-chromite-pyroxene oxythermobarometer.

[b] Equilibration temperature calculated using the olivine-chromite geothermometer; ΔIW is the deviation in log units from the iron-wustite buffer of the log fO_2 calculated using the olivine-chromite T and quartz-iron-fayalite (QIFa) system.

[c] Equilibration temperature calculated using the two-pyroxene geothermometer; ΔIW is the deviation in log units from the iron-wustite buffer of the log fO_2 calculated using the two-pyroxene T and quartz-iron-ferrosilite (QIFs) system.

[d] Fe–Ti oxide mineral pairs
[e] distribution of Ca between olivine and augite. The fO_2 of NWA 6926 was reported as FMQ = –2.6 in Hibiya et al., 2019. It was converted to IW+1.47 at 900 °C according to Frost (1991).
[f] valences of Cr, Ti, and V determined by micro-XANES spectroscopy.

Table 5.6. Silicon and iron isotopic composition (‰) of meteorites.

Meteorite	**Type**	**δ^{29}Si±2SE**	**δ^{30}Si±2SE**	**δ^{56}Fe±2SE**	**δ^{57}Fe±2SE**
Eagles Nest	brachinite	−0.156±0.029	−0.291±0.022	0.063±0.020	0.081±0.049
NWA 4882	brachinite	−0.260±0.007	−0.500±0.036	0.042±0.012	0.059±0.021
Reid 013	brachinite	−0.279±0.029	−0.513±0.021	0.006±0.022	0.008±0.020
NWA 3151	brachinite	−0.266±0.026	−0.521±0.026	0.009±0.016	0.022±0.030
Tafassasset	prim. ung. ach.	−0.316±0.028	−0.543±0.060	−0.055±0.007	−0.056±0.015
NWA 5297	prim. ung. ach.	−0.276±0.015	−0.552±0.018	−0.009±0.007	0.013±0.014
NWA 6926	ung. ach.	−0.239±0.040	−0.476±0.024	0.015±0.035	0.033±0.060
NWA 6962	ung. ach.	−0.259±0.012	−0.480±0.017	−0.011±0.019	0.015±0.021
NWA 8777	ung. ach.	−0.212±0.030	−0.471±0.029	0.056±0.011	0.090±0.027
NWA 10503	ung. ach.	−0.228±0.047	−0.443±0.079	0.017±0.012	0.021±0.020
GRA 06129	ung. ach.	−0.248±0.029	−0.454±0.052	0.056±0.013	0.081±0.030
GRA 06129	ung. ach.	−0.248±0.029	−0.454±0.052	0.056±0.013	0.081±0.030
NWA 2976	ung. ach.	−0.143±0.029	−0.230±0.052	0.077±0.013	0.095±0.020
NWA 8486	ung. ach.	−0.185±0.019	−0.372±0.034	−0.316±0.020	−0.459±0.040
NWA 11119	ung. ach.	−0.103±0.015	−0.221±0.020	0.057±0.017	0.097±0.019

prim. ung. ach. – primitive ungrouped achondrite
ung. ach. – ungrouped achondrite

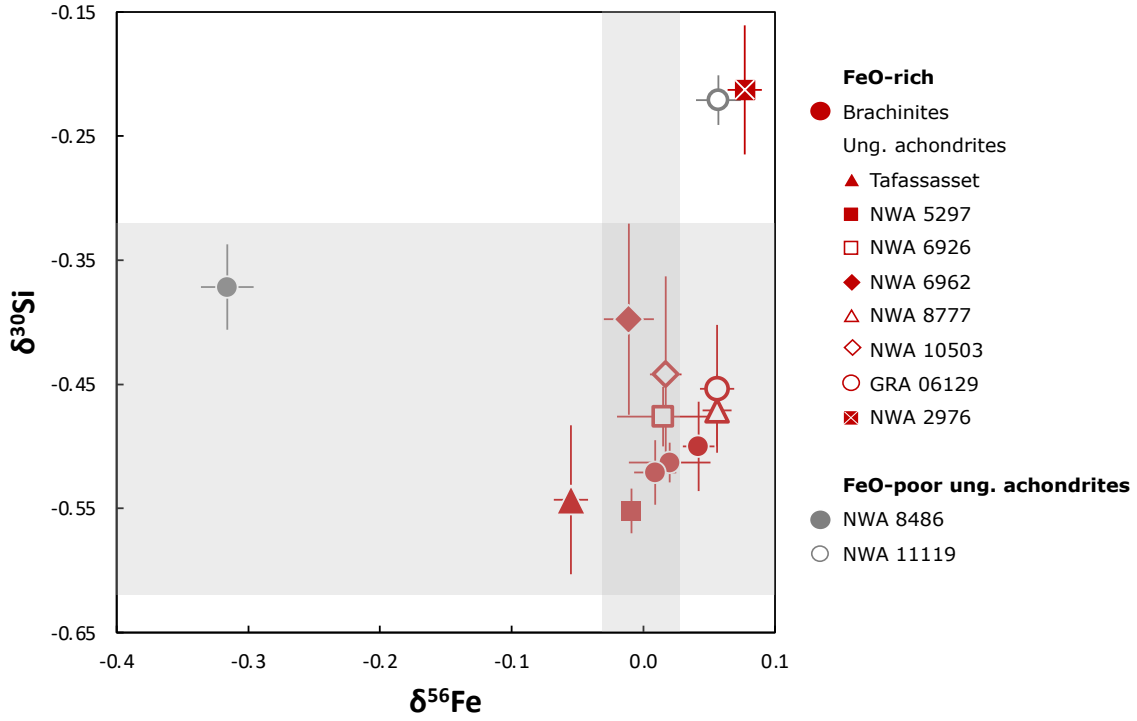

Figure 5.1. $\delta^{30}Si$ – $\delta^{56}Fe$ of brachinites and ungrouped achondrites. The horizontal grey bar represents the $\delta^{30}Si$ (avg±2SD) of the ordinary and carbonaceous chondrites. The vertical grey bar represents the $\delta^{56}Fe$ (avg±2SD) of enstatite, ordinary, and carbonaceous chondrites. Maroon symbols: FeO-rich achondrites; Grey symbols: FeO-poor achondrites.

5.5 Discussion

5.5.1 FeO-rich meteorites

Ferrous oxide-rich achondrites comprise of brachinites, brachinite-like achondrites, and several ungrouped achondrites thought to have been derived from volatile-rich asteroids that underwent variable degrees of partial melting leading to the formation of melt residues, cumulates, and melt (Day et al., 2019). The preponderance of high FeO in silicates (Mg# <80) and oxidizing conditions of formation (~IW-1 to +2) distinguishes FeO-rich achondrites from other partially melted achondrites such as ureilites, acapulcoites, and lodranites. Ferrous oxide-rich achondrites therefore have the potential to provide information on the role of oxidizing condition and degree of partial melting in influencing their Si and Fe isotope

composition. In the following section, we discuss the Fe and Si isotope composition of the FeO-rich achondrites in this study in light of their possible petrogenesis and the differentiation processes occurring on their parent bodies.

5.5.1.1 Brachinites

Brachinites have been suggested to be igneous cumulate rocks (Warren and Kallemeyn, 1989; Swindle et al., 1998; Mittlefehldt and Berkeley, 2002; Mittlefehldt et al., 2003) and impact melt rock (Ryder, 1982). However, their olivine-dominated mineralogy, recrystallized texture, equilibrated mineral compositions, incompatible element depletion, and equilibration temperatures above the silicate eutectic strongly suggest brachinites are residues left behind after varying degrees of partial melting (Nehru et al., 1983; 1992; 1996; Prinz, 1998; Wadhwa et al., 1998a; b; Gardner-Vandy et al., 2013; Goodrich and Delaney, 2000; Goodrich et al., 2011; Day et al., 2012; Day et al., 2019). Gardner-Vandy et al. (2013) determined that the equilibration temperatures of brachinites ALH 84025, Hughes 026, NWA 3151, NWA 4969, Brachina and EET 99402 are above the ordinary chondrite Fe-FeS eutectic (~950 °C; Kullerud, 1963) and all but ALH 84025 and EET 99405 have reached the silicate eutectic in fayalite-rich systems (~1050 °C; Schairer and Yoder, 1961). This suggests that, during heating of a chondrite-like parent lithology, partial melts may have been removed leaving behind an ultramafic, highly olivine-normative residue in form of the brachinites. Most brachinites have very little sulfide, suggesting that the Fe-FeS eutectic melt was largely removed (Keil, 2014). The removal of a pyroxene-plagioclase melt during low degrees of partial melting is also corroborated by the depleted Na/Sc and Sm/Sc ratios compared to a chondritic composition of some brachinites (Goodrich et al., 2011). Furthermore, experiments involving 14−31% partial melting of an R-chondrite starting material at 1250 °C, 1 bar, and IW-1

conditions, result in residual phases with mineralogical compositions similar to brachinites (Gardner-Vandy et al., 2013).

All four brachinites in this study, viz., Eagles Nest, NWA 3151, NWA 4882, and Reid 013 have equilibration temperatures close to the silicate eutectic (1050 °C) which indicates removal of silicate melt. In order to assess the effect of partial melt removal on the δ^{56}Fe and δ^{30}Si isotopic composition of brachinites, we consider the three brachinites NWA 3151, NWA 4882, and Reid 013. We exclude Eagles Nest because its compositional data such as LREE enrichment and negative Ce anomaly along with several mineralogical and petrographic indicators like Fe-rich oxide rims around olivine grains and fracture filled with potentially wind-blown terrestrial quartz and orthoclase (Swindle et al., 1998) attest to the fact that Eagles Nest has undergone substantial terrestrial contamination. Such intensive terrestrial weathering is also reflected in the 'terrestrial' δ^{56}Fe and δ^{30}Si values for Eagles Nest, i.e., 0.063±0.020‰ and −0.291±0.022‰, respectively.

The effect of partial melting on the residue, i.e., brachinites can be determined using the mass balance equation from Craddock et al. (2013),

$$\delta^{56}\mathrm{Fe}_{\mathrm{residue}} - \delta^{56}\mathrm{Fe}_{\mathrm{source}} \approx -\mathrm{F} * (\Delta^{56}\mathrm{Fe}_{\mathrm{melt-solid}}) \quad (5.5)$$

where F is the degree of melting which is 14−30% (Day et al., 2012; Gardner-Vandy et al., 2013) and $\Delta^{56}\mathrm{Fe}_{\mathrm{melt-solid}}$= 0.053±0.017 in Fe^{3+}-free systems (Elardo and Shahar, 2017; Elardo et al., 2019). Since the δ^{56}Fe of chondrites is fairly uniform irrespective of their oxidation state or group (Craddock and Dauphas, 2011) and considering that a R-chondrite like composition is a suitable precursor for brachinites (Gardner-Vandy et al., 2013), we have assumed the $\delta^{56}Fe_{source}$ to be 0.005±0.006‰ (Craddock and Dauphas, 2011). The δ^{56}Fe of the residue, i.e., brachinites, is estimated to range between −0.002±0.006‰ and −0.011±0.007‰ corresponding to 14 and 30% of partial melting, respectively. Therefore, partial melting, as has been demonstrated previously by Craddock et al., 2013, has limited effect on the

residue such that brachinites which are considered to be partial melt residues of a chondritic source will retain a chondritic $\delta^{56}Fe$ composition (Wang et al., 2014a). The $\delta^{56}Fe$ values of the three brachinites in this study as well as of the six brachinites (avg. 0.01±0.02‰) reported by Wang et al. (2014a) are similar to chondrites and therefore, support the origin of brachinites as partial melts of a chondritic source. The slightly heavier $\delta^{56}Fe$ of NWA 4882 compared to other brachinites could be attributed to a potential secondary thermal event ~15 Ma after the formation of Brachina as suggested by the younger ^{53}Mn-^{53}Cr age of 4549.4 ± 2.3 Ma of NWA 4882 (Dunlap, 2021).

Magmatic differentiation processes such as fractional crystallization and partial melting lead to formation of olivine-rich cumulates or residues, respectively. Since, olivine is enriched in the lighter isotopes of Si as has been demonstrated through theoretical predictions (Méheut and Schauble, 2014; Rabin et al., 2021) and terrestrial samples (e.g., Savage et al., 2011), the formation of brachinites as olivine-rich residues of partial melting has rendered them with a light Si isotope composition. Recently, Rabin et al. (2021) investigated the effect of second atomic neighbors using ab initio calculations and concluded that the increase in olivine Fe content results in a decrease of force constant and thereby, facilitates the enrichment of the lighter Si isotopes in olivine. This should hold true for FeO-rich olivine which form a major component of brachinites and thereby, result in a light $\delta^{30}Si$ value. To summarize, brachinites are olivine-dominated meteorites with a recrystallized texture whose $\delta^{56}Fe$ and $\delta^{30}Si$ compositions can be interpreted as evidence of partial melting and melt removal on the brachinite parent body.

Brachinite-like achondrites are similar to brachinites in terms of their olivine dominated mineralogy (e.g., Day et al., 2012; Goodrich et al., 2017a) and oxygen isotope compositions (Greenwood et al., 2012; 2014). Brachinite-like achondrites, which have more magnesian compositions and a larger fraction of orthopyroxene

than brachinites, seem to have undergone similar melt-depletion processes to brachinites, but on different parent bodies (Day et al., 2012). Our study does not include any brachinite-like achondrite as enlisted by Day et al. (2012) and Goodrich et al. (2017a). However, Dauphas et al. (2015) reported the weighted average value for δ^{30}Si of brachinite-like achondrites NWA 5400/NWA 5363 to be -0.468 ± 0.033‰ which is similar, within error, to the average δ^{30}Si of brachinites (-0.511 ± 0.021‰) in this study. It is likely that the slightly lower Fa content of the brachinite-like achondrites results in a minor enrichment of the heavier Si isotopes compared to brachinites.

5.5.1.2 Ungrouped achondrites

5.5.1.2.1 Tafassasset

Tafassasset is an ungrouped primitive achondrite with an oxygen isotope composition similar to CR chondrites (Gardner-Vandy et al., 2012). The closure temperature for Tafassasset derived from the olivine-spinel and two pyroxene thermometers suggest the removal of a partial melt from a parent body that never attained isotopic homogeneity or complete melting (Gardner-Vandy et al., 2012). However, the degree of partial melting in Tafassasset is lower than that inferred for brachinites and therefore, most likely resulted in the textural and mineralogical heterogeneity observed in Tafassasset (Gardner-Vandy et al., 2012). Although Tafassasset is predominantly composed of FeO-rich olivine (avg. ~58%), it is heterogeneous in the proportions of Fe-Ni metal (avg. ~10 vol.%) and sulfide (avg. ~3 vol.%). While sampling a 'bulk composition' of Tafassasset, we avoided the large metal grains (up to a size of 3 mm) which would have been difficult to digest using the alkali fusion method. Additionally, the presence of excess Fe from the metal would have led to the fractionation of Si isotopes due to adsorption of Si on Fe hydroxides as has been documented for iron-rich samples (Chen et al., 2017 and

references therein). The δ^{56}Fe value of Tafassasset reported here (-0.055 ± 0.013‰) is lighter than the 'chondritic' δ^{56}Fe expected for a primitive achondrite. The light δ^{56}Fe value can be attributed to the unsampled metal grains that are potential reservoirs of heavy Fe isotopes. To test this hypothesis, we use the following mass balance equation to calculate the δ^{56}Fe of the non-metallic fraction of Tafassasset ($\delta^{56}Fe_{Tafa*}$) by assuming a 'chondritic' δ^{56}Fe for bulk Tafassasset ($Fe_{bulkTafa}$).

$$\left[\left(1-f_{metal}^{Fe}\right)*\delta^{56}Fe_{Tafa*}\right]+\left[f_{metal}^{Fe}*\delta^{56}Fe_{metal}\right]=\delta^{56}Fe_{bulkTafa} \quad (5.6)$$

where f_{metal}^{Fe} is the fraction of total Fe in Tafassasset metal. Assuming 10 vol% metal, density of 7.8 g/cm^3, and 89.16 wt% Fe in the metal (Gardner-Vandy et al., 2012), 1 cm^3 of Tafassasset contains 0.695 g of Fe in the metal. Similarly, with 90 vol% non-metal, density of ~3.3 g/cm^3, and 40.4 wt% Fe (Gardner-Vandy et al., 2012), 1 cm^3 of Tafassasset contains 1.2 g of Fe in the non-metallic portion. Therefore, using f_{metal}^{Fe}= 0.695/(0.695+1.2) = 0.367, $\delta^{56}Fe_{metal}$ = 0.1‰, and $\delta^{56}Fe_{bulkTafa}$ ~ 0‰ in equation 5.6, the $\delta^{56}Fe_{Tafa*}$ is estimated to be ~ -0.05‰ which is similar to the δ^{56}Fe value measured in this study (Table 5.6). It is to be noted that this a first-order approximation of $\delta^{56}Fe_{Tafa*}$ and is meant to demonstrate that non-sampling of the large metal grains could have resulted in the lighter δ^{56}Fe of Tafassasset reported here. Therefore, the δ^{56}Fe of bulk Tafassasset can be considered to be 'chondritic' as is expected for primitive achondrites that have experienced partial melt removal. The δ^{30}Si = -0.543 ± 0.060 is similar to brachinites and the primitive achondrite NWA 5297 and is unlikely to be affected by the non-sampling of the Si-free metal.

5.5.1.2.2 NWA 5297

NWA 5297 has been classified as an ungrouped primitive achondrite with a poikiloblastic, metamorphic texture which contains too much metal (10 vol%) to be

considered a metamorphic product of LL chondrites despite their similar oxygen isotope composition (Irving and Kuehner, 2010). The mineralogy of NWA 5297 comprises predominantly of olivine, low-Ca pyroxene, sodic plagioclase, and minor Ni-bearing troilite. The silicates of NWA 5297 plot within the field of brachinites and primitive achondrites on a plot of Fe/Mn versus Fe/Mg ratios. (Dunlap et al., 2015). The δ^{56}Fe and δ^{30}Si compositions of NWA 5297 are -0.009 ± 0.007‰ and -0.552 ± 0.018‰, respectively which are similar to that of brachinites. The δ^{56}Fe and δ^{30}Si values of NWA 5297 suggest its parent body was affected by processes that similar to those operating on the brachinite parent body(s) and also attest to the primitive nature of NWA 5297.

5.5.1.2.3 NWA 6926

NWA 6926 is paired with the extensively studied NWA 6693 and NWA 6704 ungrouped achondrites (Irving and Kuehner, 2012a; Jambon et al., 2012; Warren et al., 2013; Hibiya et al., 2019; Day et al., 2019; Sanborn et al., 2019) and could potentially be a portion of the NWA 6704 meteorite (Irving and Kuehner, 2012b). It has an overall igneous cumulate texture composed of low-Ca pyroxene (with modal abundance of 76.9%) along with olivine (11.6%), plagioclase (11.1%), chromite (0.14%), awaruite (0.27%), merrillite (0.05%), and sporadic metal and sulfides. The FeO-rich, subchondritic MgO/SiO_2 bulk composition coupled with the high concentrations and limited fractionation amongst non-chalcophile, non-volatile elements indicate its formation as an igneous cumulate and precludes extensive fractional crystallization processes (Warren et al., 2013). In an independent study of the paired achondrite NWA 6704, Hibiya et al. (2019) do not support the formation of NWA 6704/6693 as cumulates as was proposed by Warren et al. (2013) and Day et al. (2019). Instead, Hibiya et al. (2019) interpreted the 1) mostly chondritic major element and HSE abundances, 2) unfractionated or weakly fractionated REE and

siderophile patterns, 3) significant depletion of highly volatile elements (i.e., T_c > 900 K), and 4) lack of systematic depletion of highly incompatible lithophile elements to reflect the rapid melting of a chondritic precursor to generate melt from which highly volatile elements were lost followed by rapid crystallization to ensure minimal segregation of metal and sulfides and silicate differentiation. The rapid cooling of NWA 6704/NWA 6693 is also supported by the concordant ages determined using multiple isotopic systems, viz., ^{26}Al-^{26}Mg (Sanborn et al., 2019), ^{53}Mn-^{53}Cr (Sanborn et al., 2019), and ^{207}Pb-^{206}Pb ages (Amelin et al., 2019). The precursor of NWA 6704/6693 is considered to be extremely oxidized, FeO-rich, primitive material as suggested by the high Ni content of olivine, metal and sulfide phases, ferric content in chromite and fO_2 estimations ranging from ΔIW+2.2 to +0.7 determined from the vanadium content in spinel and olivine-pyroxene-spinel oxybarometer respectively (Warren et al., 2013) and FMQ−2.6 using the olivine-spinel oxygen geobarometry (Hibiya et al., 2019). The chondritic δ^{56}Fe (0.015±0.035‰) and δ^{30}Si (−0.476±0.024‰) composition of NWA 6926 supports its origin via minimal differentiation.

Hibiya et al. (2019) interpreted the subchondritic Mg/Si (~0.52×CI) of NWA 6704 to reflect significant nebular fractionation of forsterite in its provenance. According to the trend observed between the Mg/Si and δ^{30}Si, Dauphas et al. (2015) proposed that Si isotope variations were a result of isotopic fractionation between gaseous SiO and forsterite in the nebula. Following this line of evidence, the subchondritic Mg/Si of NWA 6926 should correspond to a light δ^{30}Si. However, the δ^{30}Si of NWA 6926, which is similar to that of carbonaceous and ordinary chondrites, suggests either (1) the correlation between Mg/Si and δ^{30}Si is weak suggesting limited effect of nebular forsterite condensation on δ^{30}Si (Moynier et al., 2020); or (2) the subchondritic Mg/Si of NWA 6926 reflects its cumulative nature (Warren et al., 2013).

5.5.1.2.4 NWA 6962

NWA 6962 is an ungrouped achondrite which predominantly consists of equant olivine grains along with interstitial intergrowths of plagioclase, clinopyroxene, and minor merrillite, and accessory minerals such as Ti-poor chromite, kamacite, and iron sulfide. Although NWA 6962 is considered as being brachinite-like (Irving and Kuehner, 2015), it has a distinct oxygen isotope composition, higher Fe content in olivine ($Fa_{47.1\text{-}47.9}$) and clinopyroxene ($Fs_{15.4\text{-}20.0}$) compared to brachinites (Dunlap et al., 2015). However, its $\delta^{56}Fe = -0.011 \pm 0.019‰$ coincides with the range estimated for brachinites (Section 5.1.1) and it has a $\delta^{30}Si = -0.480 \pm 0.017‰$ which overlaps with that of the carbonaceous and ordinary chondrites.

5.5.1.2.5 NWA 8777

Although similar to some brachinites in terms of oxygen isotope composition and texture, NWA 8777 is classified as an ungrouped achondrite due to its orthopyroxene-dominated mineralogy (88.6 vol%), low olivine content (9 vol%), and high-Ca plagioclase (Irving and Kuehner, 2017a). The $\delta^{56}Fe$ of NWA 8777, i.e., $0.056 \pm 0.011‰$ is heavier than a chondritic value and could be attributed to melt fertilization wherein interaction with heavy $\delta^{56}Fe$ melt has enriched NWA 8777 in the heavy isotopes of Fe. 'The chondritic' $\delta^{30}Si$ of NWA 8777, i.e., $-0.471 \pm 0.029‰$ could be interpreted to support melt re-fertilization. Based on the similarity in oxygen isotope composition and redox conditions between NWA 8777 and brachinites, it seems likely that NWA 8777 originated from a precursor that sampled a reservoir similar to brachinites. As seen previously, the partial melt GRA 06129 which formed on a volatile-rich, oxidized precursor possessed a slightly heavy $\delta^{56}Fe$ and chondritic $\delta^{30}Si$. In principle, if a similar partial melt originating on the parent body of NWA 8777 reacted with it, the $\delta^{56}Fe$ would be driven to heavier values

without altering the 'chondritic' $\delta^{30}Si$. Therefore, it is likely that NWA 8777 underwent melt-rock interactions. Reaction with isotopically heavy melts were similarly invoked to explain the heavy $\delta^{56}Fe$ of several mantle peridotites (Weyer and Ionov, 2007).

5.5.1.2.6 NWA 10503

NWA 10503 is an ungrouped achondrite with a mineralogy consisting predominantly of Fe-rich olivine (Fa_{32}), clinopyroxene, plagioclase and other accessory phases. Although NWA 10503 has a mineral composition similar to brachinites, their oxygen isotope compositions are distinct (Irving and Kuehner, 2017b). The $\delta^{56}Fe$ (0.017±0.012‰) and $\delta^{30}Si$ (−0.443±0.079‰) are similar to that of carbonaceous and ordinary chondrites and reflect the primitive nature of NWA 10503.

5.5.1.2.7 GRA 06129

The formation of brachinites as residues of partial melting of a volatile-rich, oxidized chondritic source implies the presence of complementary partial melts. The ancient whole rock ^{26}Al-^{26}Mg model ages for the brachinites Brachina and NWA 4882 indicate that the brachinite body accreted and began melting within ~0.5 Ma of Solar System formation (Dunlap, 2021). Despite early silicate melting on the brachinite parent body, the absence of basalts complementary to the residual brachinites has been interpreted as the brachinite parent body being <100 km in radius that resulted in the loss of basalts to space due to explosive volcanism (Keil, 2014). However, the paired achondrites GRA 06128 and GRA 06129 with felsic, andesitic to trachy-andesitic bulk composition have been considered to be the evolved felsic crust of the brachinite parent body (Day et al., 2009). Similarities in oxygen isotope composition, oxygen fugacity, contemporaneous melting-crystallization model ages, and

complementary petrology and trace-element geochemistry (Zeigler et al., 2008; Day et al., 2009; Day et al., 2012; Shearer et al., 2010) suggest that GRA 06218/9 are the felsic crustal complements to the residual brachinites. GRA 06128/9 is hypothesized to have formed by low-to-moderate- degree (13–30%) partial melting of a primitive, volatile-rich source region from an asteroid that had not fully differentiated a metallic core (Day et al., 2009; Shearer et al., 2010). Melts produced due to 14-31% partial melting of R chondrite at 1250°C are depleted in SiO_2, Al_2O_3 and enriched in FeO, MgO and CaO compared to GRA 06129. Therefore, Gardner-Vandy et al., 2013 suggested that either (a) R chondrite-like material is not a viable precursor for GRA 06129 or (b) GRA 06129 forms by low degrees (<10%) of partial melting of R chondrites below 1250°C. Subsequent partial melting experiments at 1140°C were able to produce melts akin to GRA 06129 under both equilibrium and non-equilibrium regimes (Lunning et al., 2017). Partial melting of a chondritic source (Mg/Si ~1-1.03, high NaK#) at IW-1 (Collinet and Grove, 2020) or an R chondrite-like precursor at IW+1 (Lunning et al., 2017) can lead to the formation of silica- and alkali-rich melts akin to the GRA 06129. Two models have emerged for the formation of GRA 06128/9. Given its unusual bulk composition and texture, Day et al. (2009) and Day et al. (2012) argued that GRA 06128/9 samples a single, crystallized partial melt. In contrast, Shearer et al. (2010) suggested that GRA 06128/9 is an annealed breccia consisting of a nearly-pure feldspar lithology and a mafic assemblage, the former of which might require physical separation of feldspar, akin to magma ocean processes. The elevated HSE concentrations of bulk GRA 06128/9 precludes segregation of a metallic core before partial melting of the chondritic source to form GRA 06128/9. Therefore, we do not account for the Fe isotopic fractionation associated with core formation on the parent body of GRA 06128/9. To estimate the $\delta^{56}Fe$ of the partial melt that would originate on the brachinite parent body, we use the mass balance from Craddock et al., 2013,

$$\delta^{56}Fe_{melt} - \delta^{56}Fe_{source} \approx (1 - F) \times (\Delta^{56}Fe_{melt-solid}) \quad (5.7)$$

where F is the degree of melting and $\Delta^{56}Fe_{melt-solid}$= 0.053±0.017‰ in Fe^{3+}-free systems (Elardo and Shahar, 2017; Elardo et al., 2019). Assuming F=14−30% partial melting on the brachinite parent body (Day et al., 2012; Gardner-Vandy et al., 2013) and $\delta^{56}Fe_{source}$ of 0.005±0.006‰ (see Section 5.1.1.), we have estimated the $\delta^{56}Fe$ of the corresponding melt ($\delta^{56}Fe_{melt}$) to be 0.051±0.016‰ (at 14% partial melting) or 0.042±0.013‰ (at 30% partial melting). The $\delta^{56}Fe$ of GRA 06129 determined in this study is consistent with the calculated value. However, Wang et al. (2014a) reported the $\delta^{56}Fe$ value of GRA 06128/9 to be −0.08±0.06‰; the first crustal sample with a lighter $\delta^{56}Fe$ value compared to chondrites. They attributed the light $\delta^{56}Fe$ composition to the sulfide-rich melt that formed during partial melting of chondritic precursors. It has been demonstrated that the $\delta^{56}Fe$ of various minerals in a meteorite is different such that $\delta^{56}Fe$ of silicates is heavier compared to co-existing sulfides (Wang et al., 2014a). Therefore, the difference in the $\delta^{56}Fe$ value of the relatively coarse-grained GRA 06129 between this study and Wang et al., 2014a could be due to non-representative sampling. In order to make a first-order estimate of the $\delta^{56}Fe$ of bulk GRA 06128/9 based on modal mineralogy, we use the following mass balance equation,

$$(\delta^{56}Fe_{opx} * f_{opx}^{Fe}) + (\delta^{56}Fe_{cpx} * f_{cpx}^{Fe}) + (\delta^{56}Fe_{ol} * f_{ol}^{Fe}) + (\delta^{56}Fe_{sul} * f_{sul}^{Fe}) = \delta^{56}Fe_{bulk} \quad (5.8)$$

Assuming the appropriate values (i.e., modal mineralogy and FeO wt% of distinct mineral phases from Day et al., 2012; density of each phase and their $\delta^{56}Fe$ from Wang et al., 2012), the $\delta^{56}Fe_{bulk}$ of GRA 06129 is estimated to be 0.008±0.040‰ which overlaps within error of the $\delta^{56}Fe$ of GRA 06129 (0.056±0.013‰) measured in this study as well as that reported by Wang et al., 2014a (−0.08±0.06‰).

Based on principles of Si isotope fractionation, partial melts should have a $\delta^{30}Si$ value heavier compared to its precursor. For example, based on the correlation of Si isotopic composition of various samples as a function of degree of differentiation (i.e., silica content) from the Hekla volcano, Savage et al., 2011 reported a $\Delta^{30}Si_{solid-melt} \sim -0.125‰$. Therefore, GRA 06129, which is the product of partial melting of a chondritic source, should have a heavy $\delta^{30}Si$ compared to its chondritic precursor. However, its $\delta^{30}Si$ value ($-0.454 \pm 0.052‰$) is similar to ordinary and carbonaceous chondrites and does not align with the proposed origin as an andesitic partial melt of a chondritic source. It has been shown that the presence of neighboring cations such as Fe, Na, and Al affect the Si isotope composition (Méheut and Schauble, 2014; Rabin et al., 2021). Therefore, it is possible that the Fe- and Na-rich chemistry of GRA 06129 influence its Si isotope composition and preclude the enrichment of heavy Si isotopes during partial melting.

5.5.1.2.8 NWA 2976

NWA 2976 like its paired basaltic achondrites NWA 011 and NWA 2400, is mineralogically similar but chemically distinct from basaltic eucrites (Connolly et al., 2007; Yamaguchi et al., 2002; Floss et al., 2005). The bulk elemental abundances of NWA 2976/011 reveal depletions in volatile alkali metals such as K and Rb compared to chondrites (Bouvier et al., 2011) and higher volatile Mn compared to eucrites (Yamaguchi et al., 2002). Radiometric ages (Al–Mg and Pb–Pb isotope systematics) of NWA 2976 indicate that it formed by the earliest stages of extensive melting and magmatic fractionation on its parent body (Bouvier et al., 2011). NWA 2976 is considered a carbonaceous achondrite based on its Cr, Ti, O, and Sr anomalies (Trinquier et al., 2009; Moynier et al., 2012; Sanborn et al., 2019). The higher abundances of siderophile elements in NWA 2976/011 have been interpreted to reflect (1) the assimilation of an iron meteorite impactor (Yamaguchi et al., 2002) or

(2) the higher concentration of siderophile elements in the source region of NWA 2976/011 and lack of complete equilibration with Fe metal due to its oxidized nature (Korotchantseva et al., 2003). Regardless, it is unclear if the parent body of NWA 2976/011 formed a metallic core. In terms of its Si and Fe isotopic composition, NWA 2976 is distinct from the 'chondritic' composition of eucrites and is enriched in the heavy isotopes of Fe and Si. In the potential absence of a heavy Fe isotope enriched Fe-Ni metallic core, the silicate mantle of the parent body will not have a light $\delta^{56}Fe$ (Elardo and Shahar, 2017; Elardo et al., 2019) and therefore, high degree of partial melting of a chondritic source could result in a basalt with heavy $\delta^{56}Fe$. But that still doesn't explain the heavy $\delta^{30}Si$ as basaltic partial melting leads to restricted Si isotope fractionation (Savage et al., 2011; 2014). Therefore, alternative explanations such as volatilization of the lighter Fe and Si isotopes (Hin et al., 2017; Young et al., 2019) or forsterite condensation in the nebula (Dauphas et al., 2015) are required to explain the heavy $\delta^{56}Fe$ and $\delta^{30}Si$ values of NWA 2976.

5.5.2 FeO-poor meteorites

Ferrous oxide-poor meteorites formed under reducing conditions and provide a unique opportunity to understand the evolution of the Fe and Si isotope composition in response to differentiation processes under reducing conditions which thus far, was confined to aubrites. In this study, we discuss the $\delta^{56}Fe$ and $\delta^{30}Si$ of reduced achondrites NWA 8486 and NWA 11119 in light of their modes of formation.

5.5.2.1 NWA 8486

NWA 8486, an ungrouped achondrite and its widely studied paired achondrite NWA 7325, are essentially plagioclase-rich cumulate gabbroic rocks consisting primarily of calcic plagioclase (55-60 vol %), diopside (25-30 vol %), forsterite (10-15 vol %), and other accessory minerals (Irving et al., 2015; Garvie, 2017). Bulk

compositional analyses reveal high MgO and Al_2O_3 and low Fe, Mn, alkalis, Na/Al, Ga/Al, and Zn/Al all of which indicate volatile-depleted parent body that formed under reduced conditions (Barrat et al., 2015a). Suggestions that NWA 7325/8486 could potentially be a sample from Mercury arise from their similar bulk element ratios such as Al/Si and Mg/Si, highly reduced nature, and low FeO (Irving et al., 2013; Weider et al., 2012; Sutton et al., 2017). However, the ancient ages of crystallization, viz., Pb-Pb age of 4563.4±2.6 Ma (Koefoed et al., 2016), and Al-Mg age of 4562.8±0.3 Ma (Dunlap et al., 2014) and 4563.09±0.26 (Koefoed et al., 2016) for NWA 7325 were interpreted to be inconsistent with a potential origin on an evolved planetary crust such as Mercury's (Dunlap et al., 2014; Koefoed et al., 2016). NWA 8486 has similar Pb-Pb age of 4563.9 ± 1.7 Ma and Al-Mg age of 4563.06±0.26 Ma yielding an error weighted mean age of 4563.1±0.3 Ma for NWA 8486 (Dunlap, 2021). Several modes of formation of NWA 7325/8486 have been suggested, viz., 1) as a cumulate rock from an impact-remelted gabbroic rock (Barrat et al., 2015a) or basaltic melt (Goodrich et al., 2017b) depleted in incompatible trace elements or 2) melting and re-processing of an anorthositic source on an early planetesimal (Frossard et al., 2019). The highly depleted HSE abundances of NWA 8486/7325 relative to bulk chondrites are indicative of core formation and large-scale metal-silicate differentiation on its parent body (Archer et al., 2019). The light δ^{56}Fe of NWA 8486 could reflect its origin as a cumulate rock from a melt derived from the light Fe isotope-enriched silicate portion of a body left behind due to the separation of a metallic core enriched in the heavy Fe isotopes.

Aubrites, which are pyroxenitic achondrites that formed under reducing conditions (Keil, 2010; McCoy and Bullock, 2017; Chapter 3), have light δ^{56}Fe (Wang et al., 2014b) and heavy δ^{30}Si values (Savage and Moynier, 2013) compared to enstatite chondrites, their putative precursors. The Fe and Si isotopic composition of aubrites have been attributed to the segregation of a Si-bearing metallic core on the

aubrite parent body (See Chapter 3). Similarly, the light $\delta^{56}Fe$ of NWA 8486 can be explained in terms of separation of a metallic core enriched in the heavy Fe isotopes. Later reprocessing of this light Fe isotope enriched precursor led to the formation of the NWA 8486/7325. However, the 'chondritic' $\delta^{30}Si$ value of NWA 8486 suggests that various proposed modes of formation of NWA 8486/7325 did not induce any significant fractionation of Si isotopes. It is possible that the temperature or fO_2 prevalent during the core formation on the NWA 7325/8486 parent body did not facilitate the incorporation of Si into its core. This is further corroborated by the absence of Si-bearing metal in acapulcoites which formed under similar fO_2 conditions (Righter et al., 2016) and potentially from similar precursors/reservoir based on their O-Ti-Cr anomalies (Goodrich et al., 2017b).

5.5.2.2 NWA 11119

NWA 11119 is an ungrouped achondrite which has a bulk composition that is andesitic to dacitic with low total alkali, low bulk FeO content, and relatively unfractionated bulk REE pattern (Srinivasan et al., 2018). The mineralogy consists of plagioclase (38 vol%), pyroxene (39 vol%), silica (22 vol%), oxides (0.7 vol%), and sulfides (0.3 vol%). Compared to terrestrial orogenic andesites, NWA 11119 has a high Mg# of 84 and lower alkali content (0.93 wt%) (Srinivasan et al., 2018). Despite similar oxygen isotope compositions and presence of Cr-bearing high-Ca pyroxene, NWA 11119 and NWA 8486/7325 are considered to sample distinct parent bodies citing differences in free silica, and pyroxene Fe/Mn ratios (Srinivasan et al., 2018). A Pb-Pb age of 4565.42 ± 0.77 Ma (Dunlap, 2021), Mn-Cr age of 4563.78 ± 1.73 Ma (Dunlap, 2021), and an Al-Mg age of 4564.8 ± 0.3 Ma (Srinivasan et al., 2018) results in an error weighted mean age of 4564.8±0.3 Ma for NWA 11119 (Dunlap, 2021). Based on the FeO abundance of the basaltic-dacitic and andesitic-dacitic melts produced by melting of H chondrite at $\Delta IW-1$ (Usui et al., 2015) and

EH4 chondrite at ~ΔIW−5 (McCoy et al., 1999) precursors, respectively, Srinivasan et al. (2018) suggested that NWA 11119 could be the partial melt product of a chondritic source at an intermediate fO_2 (i.e., ~ΔIW−4). The heavy $\delta^{56}Fe$ of NWA 11119 can be attributed to the partial melting of its chondritic precursor which enriches the melt in the heavy Fe isotopes similar to what was observed for GRA 06129 (Section 5.1.2.3). The heavy $\delta^{30}Si$ of NWA 11119 is similar to terrestrial andesites (Savage et al., 2011) and is distinct from GRA 06129. The heavy $\delta^{30}Si$ is probably due to an increase in the degree of polymerization (Grant, 1954) and the presence of free silica which is enriched in heavy Si isotopes (Savage et al., 2011).

5.5.3 Redox conditions and its implications for $\delta^{30}Si$–$\delta^{56}Fe$ of achondrites

In an attempt to constrain the role of redox (using Fe^{3+}/Fe_{total} as a proxy) on the Fe isotopic fractionation between MORBs and mantle peridotites, Dauphas et al., 2014a were able to attribute 1/3 of the observed isotopic offset ($\delta^{56}Fe_{MORB}$–$\delta^{56}Fe_{mantle}$ ~0.08±0.03‰) to equilibrium fractionation between Fe^{2+} and Fe^{3+}. According to their results, in the absence of Fe^{3+}, there should be negligible isotopic fractionation between Fe^{2+} in melt and Fe^{2+} in solid. However, the change in coordination environment of Fe^{2+} between melt and solid should facilitate Fe isotope fractionation during partial melting (Young et al., 2015 and reference therein). Therefore, although Fe isotope fractionation is sensitive to redox (as observed from the correlation between force constant and Fe^{3+}/Fe_{total}), irrespective of the presence of Fe^{3+}, partial melting should result in the enrichment of heavy Fe isotopes in the partial melts.

There is a wide range in the fO_2 of achondrites in this study (Table 5.5). However, for the range of fO_2 investigated, there seems to be no clear correlation between fO_2 and isotopic compositions ($\delta^{56}Fe$ and $\delta^{30}Si$) of the achondrites. In Fig 5.2a, all but two achondrites (NWA 11119 and NWA 2976) have $\delta^{30}Si$ similar to

CC/OC although they range in their fO_2 values from ΔIW~ −3.5 to +2. Similarly, in Fig. 5.2b, there is no correlation between $\delta^{56}Fe$ and fO_2 of the achondrites. This suggests that the role of redox is not very predominant in controlling the Fe and Si isotopic compositions of the studied achondrites. For instance, $\delta^{56}Fe$ of the two andesites (NWA 11119 and GRA 06129) are similar although they originate on parent bodies with distinct fO_2 (ΔIW −3.41± 0.1 and ΔIW +2± 0.5, respectively). We also note that NWA 11119 and NWA 8486 have distinct $\delta^{56}Fe$ and $\delta^{30}Si$ values despite their similar fO_2 values (ΔIW −3.41± 0.1 and ΔIW −3.1± 0.2, respectively). The lack of correlation between $\delta^{56}Fe$ and fO_2 of the achondrites in this study is possibly due to the absence of Fe^{3+} under the range of fO_2 probed here and therefore, does not adhere to the empirically observed correlation between $\delta^{56}Fe$ and Fe^{3+}/Fe_{total} (Dauphas et al., 2014a). The presence of minor Fe^{3+} present in the chromite grains of meteorites NWA 5297, NWA 8777, NWA 6962, and NWA 10503 seems unlikely to have facilitated the fractionation of Fe isotopes. It is possible that the $\delta^{56}Fe$ of partial melts of extremely oxidized chondrites such as CK chondrites (i.e., FMQ+2 to +4; Righter and Neff, 2007) could be influenced by their high fO_2. However, it is currently unknown whether achondrites that represent partial melts of CK chondrites exist.

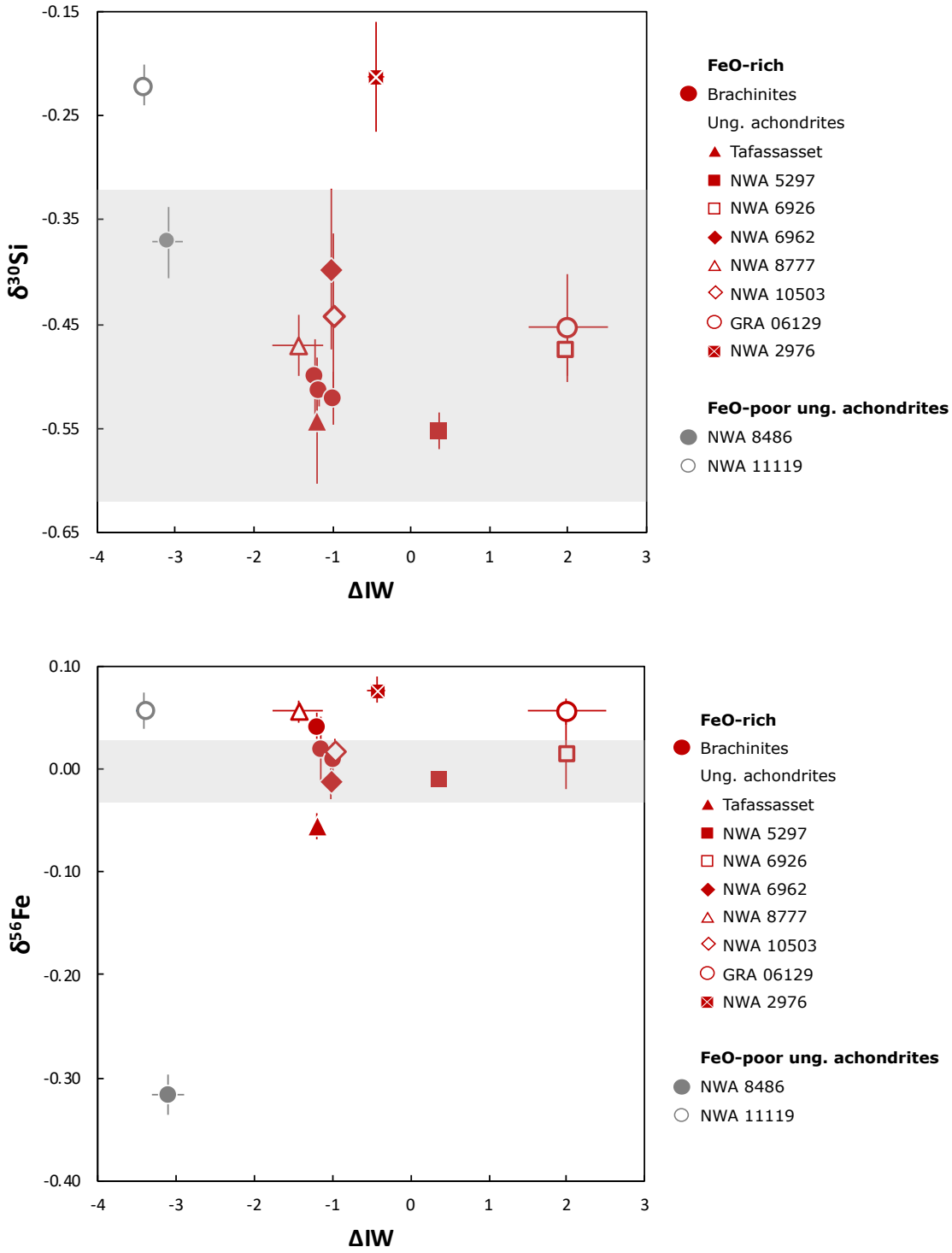

Figure 5.2. (a) $\delta^{30}Si$ vs. ΔIW of brachinites and ungrouped achondrites. The horizontal grey bar represents the $\delta^{30}Si$ (avg±2SD) of ordinary and carbonaceous chondrites. (b) $\delta^{56}Fe$ vs. ΔIW of brachinites and ungrouped achondrites. The horizontal grey bar represents the $\delta^{56}Fe$ (avg±2SD) of enstatite, ordinary, and carbonaceous chondrites. Maroon symbols: FeO-rich achondrites; Grey symbols: FeO-poor achondrites.

5.5.4 Degree of differentiation and its implications for $\delta^{30}Si$–$\delta^{56}Fe$ of achondrites

Based on isotopic anomalies of elements such as O, Ti, Cr, and Mo, meteorites can be classified as belonging to either (1) the non-carbonaceous (NC) reservoir or (2) carbonaceous (CC) reservoir (Warren et al., 2011; Kruijer et al., 2017). This division of the Solar System into the NC reservoir and CC reservoir, corresponding to the inner and outer Solar System respectively, has been attributed to the rapid growth of Jupiter to open a gap in the disk (Kruijer et al., 2017; Desch et al., 2018); formation of one or multiple pressure maxima near Jupiter's location (Brasser and Mojzsis, 2020); or migration of the snow line (Lichtenberg et al., 2021).

Of the 14 achondrites in this study, five (Tafassasset, NWA 10503, NWA 2976, NWA 6962, and NWA 6926) belong to the CC reservoir while the remaining nine originated in the NC reservoir. The presence of achondrite parent bodies and magmatic iron meteorites in both the inner and outer Solar System, suggests that differentiation processes were occurring in both the reservoirs (e.g., Kruijer et al., 2017; Sanborn et al., 2019). Based on the results of this study, it seems that the processes controlling the Fe and Si isotopes in the inner and outer Solar System were similar. The achondrites that had restricted differentiation have $\delta^{56}Fe$ and $\delta^{30}Si$ similar to their chondritic precursors irrespective of their oxygen fugacity or origin in inner versus outer Solar System. More evolved achondrites like the andesitic GRA 06129 and NWA 11119 (NC reservoir) and basaltic NWA 2976 (CC reservoir) have heavy $\delta^{56}Fe$ which is most likely a result of partial melting. The $\delta^{30}Si$ for these achondrites, however, need distinct explanations: the chondritic $\delta^{30}Si$ of GRA 06129 is probably a result of its Na- and Al-rich composition which alters the electronic density, vibrational frequency of the crystallographic sites, and the Si-O bond strength (Méheut and Schauble, 2014; Rabin et al., 2021) and therefore, does not facilitate the enrichment of heavy Si isotopes as envisaged for andesites (Savage et al., 2011); the heavy $\delta^{30}Si$ of NWA 11119 is aligned with that expected for andesites

and is a result of presence of free silica and partial melting leading to increasing polymerization. The ancient yet contemporaneous ages of NWA 2976 (CC reservoir) and angrites (NC reservoir) (Bouvier et al., 2011; Brennecka and Wadhwa, 2012) along with their volatile-depleted basaltic nature, and heavy δ^{56}Fe (Wang et al., 2012) and δ^{30}Si (Pringle et al., 2014; Dauphas et al., 2015) could point towards similar processes responsible for their Fe and Si isotope composition. These processes could either be (1) forsterite condensation in the nebula (Dauphas et al., 2015) or (2) volatilization of the lighter isotopes (Pringle et al., 2014; Hin et al., 2017). Therefore, we conclude that the degree of partial melting exerts a major control on the δ^{56}Fe and δ^{30}Si of the achondrites in this study.

5.5.5 Evolved silica-rich asteroidal crusts

The discovery of several silica-rich asteroidal crusts such as GRA 06129 (Day et al., 2009); NWA 11119 (Srinivasan et al., 2018); ALM-A (Bischoff et al., 2014); Erg Chech 002 (Barrat et al., 2021) reveals the diversity of the magmatism that occurred in the early Solar System. Through a series of experiments, Collinet and Grove (2020) demonstrated that low degrees of partial melting (<15%) of chondritic precursors that are relatively undepleted in alkalis, led to the formation of trachyandesitic lavas irrespective of fO_2 and mode of melt extraction. Wang et al. (2012; 2014a) also posited that although fO_2 is one of the primary controls on Fe isotope fractionation in higher degrees of partial melting leading to formation basalts (such as angrites, eucrites, shergottites), its role is diminished on parent bodies that undergo low degrees of partial melting.

Both GRA 06129 (SiO_2 = 55 wt%; Na_2O = 6.74 wt%; FeO = 11.8 wt%; Day et al., 2009) and NWA 11119 (SiO_2 = 61.37 wt %; Na_2O = 0.89 wt %; FeO = 1.49 wt % Srinivasan et al., 2018) have andesitic compositions. However, GRA 06129 is more SiO_2-poor, FeO-rich (oxidized), and alkali-rich (probably related to its more

volatile-rich nature) compared to NWA 11119. These differences, however, between the two meteorites, do not seem to affect the $\delta^{56}Fe$ composition significantly. The similar $\delta^{56}Fe$ values of GRA 06129 and NWA 11119 are heavier than chondrites which suggests the role of partial melting of a chondritic source to form heavier melts. The $\delta^{30}Si$ values, on the contrary, are dissimilar. There are two possible scenarios for this, 1) The heavy $\delta^{30}Si$ value of NWA 11119 aligns with and can be attributed to its SiO_2-rich nature as is the case with terrestrial andesites (Savage et al., 2011; 2014) while the 'chondritic' $\delta^{30}Si$ of GRA 06129 is due to its Na- and Al-rich composition; 2) alternatively, it is possible that low degrees of partial melting do not significantly alter the Si isotope composition of resulting melts. Therefore, the $\delta^{30}Si$ value of GRA 06129 reflects the $\delta^{30}Si$ of its chondritic source. Following the same logic, NWA 11119 should possess a chondritic $\delta^{30}Si$ in principle, however, the presence of abundant free-silica and low-alkali perhaps drives the $\delta^{30}Si$ to a heavier value. Experimental data on the fractionation of Si isotopes during low degrees of partial melting in the presence of alkalis might help to determine the cause of the difference in the $\delta^{30}Si$ values of GRA 06129 and NWA 11119.

The ureilitic trachyandesitic lava clast ALM-A which is possibly a partial melt derived on the ureilite parent body (Bischoff et al., 2014) also has heavy $\delta^{56}Fe$ composition (Barrat et al., 2015b) which is coherent with its origin as partial melt of a chondritic source. Although its $\delta^{30}Si$ has not been measured yet, based on its Na-rich plagioclase composition, it is possible that it has a 'chondritic' $\delta^{30}Si$ similar to GRA 06129. Similarly, it is possible that the Na-rich andesite Erg Chech 002 (Barrat et al., 2021) possesses a heavy $\delta^{56}Fe$ but 'chondritic' $\delta^{30}Si$. Therefore, if the silica-rich, evolved achondrites have heavy $\delta^{56}Fe$, it indicates that low degrees of partial melting of a chondritic source, results in the enrichment of the heavy Fe isotopes in the melt. On the other hand, if the Na-rich andesitic to trachyandesitic lavas have

'chondritic' $\delta^{30}Si$, it could point towards the effect of the presence of cations Na and Al on the $\delta^{30}Si$ value.

5.6 Conclusions

Based on the results of this study, we conclude that,

1) Irrespective of the wide range in the fO_2 ($\Delta IW \sim -3.5$ to $+2$) of the achondrites in this study, redox does not seem to play a major role in determining their $\delta^{56}Fe$ and $\delta^{30}Si$ values.
2) It seems that the mode of formation and degree of partial melting exerts major control on the $\delta^{56}Fe$ and $\delta^{30}Si$ values of the studied achondrites irrespective of their redox or origin in the inner versus outer Solar System. For instance, brachinites, brachinite-like achondrites, and other primitive achondrites have 'chondritic' $\delta^{56}Fe$ and $\delta^{30}Si$ as removal of partial melts does not alter the isotopic composition of residues to a great extent. However, terrestrial weathering has potentially altered the $\delta^{56}Fe$ and $\delta^{30}Si$ of Eagle Nest while secondary thermal event (NWA 4882), and melt-rock interaction (NWA 8777) have potentially affected their $\delta^{56}Fe$ only. Ungrouped achondrites that are basaltic and andesitic-trachyandesitic in composition have heavy $\delta^{56}Fe$ which is possibly the result of partial melting leading to the enrichment of heavy Fe isotopes. The Si isotopic composition, however, seems to be affected by the presence of cations such as Na and Al as has previously been suggested by Méheut and Schauble, 2014; Rabin et al., 2021.
3) The combined $\delta^{56}Fe$ and $\delta^{30}Si$ of achondrites can be used as tracers of differentiation and modes of formation in combination with their mineralogy and chemical composition.

REFERENCES

Abraham K., Opfergelt S., Fripiat F., Cavagna A. J., de Jong J. T. M., Foley S. F., André L. and Cardinal D. (2008) δ^{30}Si and δ^{29}Si Determinations on USGS BHVO-1 and BHVO-2 Reference Materials with a New Configuration on a Nu Plasma Multi-Collector ICP-MS. *Geostand. Geoanalytical Res.* **32**, 193–202.

Akram W. and Schönbächler M. (2016) Zirconium isotope constraints on the composition of Theia and current Moon-forming theories. *Earth Planet. Sci. Lett.* **449**, 302–310.

Amelin Y., Koefoed P., Iizuka T., Fernandes V. A., Huyskens M. H., Yin Q. Z. and Irving A. J. (2019) U-Pb, Rb-Sr and Ar-Ar systematics of the ungrouped achondrites Northwest Africa 6704 and Northwest Africa 6693. *Geochim. Cosmochim. Acta* **245**, 628–642.

Anbar A. D. (2004) Iron stable isotopes: Beyond biosignatures. *Earth Planet. Sci. Lett.* **217**, 223–236.

Anderson D. J., Lindsley D. H. and Davidson P. M. (1993) QUILF: a PASCAL program to assess equilibria among Fe– Mg–Ti oxides, pyroxenes, olivine, and quartz. *Comput. Geosci.* **19**, 1333–1350.

Archer G. J., Walker R. J. and Irving A. J. (2019) Highly siderophile element and 187 Re- 187 Os isotopic systematics of ungrouped achondrite Northwest Africa 7325: Evidence for complex planetary processes. *Meteorit. Planet. Sci.* **54**, 1042–1050.

Armytage R. M. G., Georg R. B., Savage P. S., Williams H. M. and Halliday A. N. (2011) Silicon isotopes in meteorites and planetary core formation. *Geochim. Cosmochim. Acta* **75**, 3662–3676.

Armytage R. M. G., Georg R. B., Williams H. M. and Halliday A. N. (2012) Silicon isotopes in lunar rocks: Implications for the Moon's formation and the early history of the Earth. *Geochim. Cosmochim. Acta* **77**, 504–514.

Arnold G. L., Weyer S. and Anbar A. D. (2004) Fe Isotope Variations in Natural Materials Measured Using High Mass Resolution Multiple Collector ICPMS. *Anal. Chem.* **76**, 322–327.

Baedecker P. A. and Wasson J. T. (1975) Elemental fractionation among chondrites. *Geochim. Cosmochim. Acta* **39**, 735–765.

Baker J. A., Schiller M. and Bizzarro M. (2012) 26Al- 26Mg deficit dating ultramafic meteorites and silicate planetesimal differentiation in the early Solar System? *Geochim. Cosmochim. Acta* **77**, 415–431.

Barrat J. A., Greenwood R. C., Verchovsky A. B., Gillet P., Bollinger C., Langlade J. A., Liorzou C. and Franchi I. A. (2015a) Crustal differentiation in the early

solar system: Clues from the unique achondrite Northwest Africa 7325 (NWA 7325). *Geochim. Cosmochim. Acta* **168**, 280–292.

Barrat J. A., Rouxel O., Wang K., Moynier F., Yamaguchi A., Bischoff A. and Langlade J. (2015b) Early stages of core segregation recorded by Fe isotopes in an asteroidal mantle. *Earth Planet. Sci. Lett.* **419**, 93–100.

Barrat J. A., Greenwood R. C., Keil K., Rouget M. L., Boesenberg J. S., Zanda B. and Franchi I. A. (2016) The origin of aubrites: Evidence from lithophile trace element abundances and oxygen isotope compositions. *Geochim. Cosmochim. Acta* **192**, 29–48.

Barrat J. A., Chaussidon M., Yamaguchi A., Beck P., Villeneuve J., Byrne D. J., Broadley M. W. and Marty B. (2021) A 4,565-My-old andesite from an extinct chondritic protoplanet. *Proc. Natl. Acad. Sci. U. S. A.* **118**, 1–7.

Benedix G. K., Lauretta D. S. and McCoy T. J. (2005) Thermo- dynamic constraints on the formation conditions of winonaites and silicate-bearing IAB irons. *Geochim. Cosmochim. Acta* **69**, 5123–5131.

Berthet S., Malavergne V. and Righter K. (2009) Melting of the Indarch meteorite (EH4 chondrite) at 1 GPa and variable oxygen fugacity: Implications for early planetary differentiation processes. *Geochim. Cosmochim. Acta* **73**, 6402–6420.

Bigeleisen J. and Mayer M.G. (1947) Calculation of equilibrium constants for isotopic exchange reactions. *J. Chem. Phys*. **15**, 261–267 (1947).

Birch F. (1964) Density and composition of the mantle and the core. *Journal of Geophysical* Research **69**, 4377-4388.

Bischoff A., Horstmann M., Barrat J. A., Chaussidon M., Pack A., Herwartz D., Ward D., Vollmer C. and Decker S. (2014) Trachyandesitic volcanism in the early Solar System. *Proc. Natl. Acad. Sci. U. S. A.* **111**, 12689–12692.

Black J. R., Epstein E., Rains W. D., Yin Q. Z. and Casey W. H. (2008) Magnesium-isotope fractionation during plant growth. *Environ. Sci. Technol.* **42**, 7831–7836.

Bonnand P. and Halliday A. N. (2018) Oxidized conditions in iron meteorite parent bodies. *Nat. Geosci.* **11**, 401–404.

Bourdon B., Roskosz M. and Hin R. C. (2018) Isotope tracers of core formation. *Earth-Science Rev.* **181**, 61–81.

Bouvier A., Spivak-Birndorf L. J., Brennecka G. A. and Wadhwa M. (2011) New constraints on early Solar System chronology from Al-Mg and U-Pb isotope systematics in the unique basaltic achondrite Northwest Africa 2976. *Geochim. Cosmochim. Acta* **75**, 5310–5323.

Brantley S. L., Liermann L. and Bullen T. D. (2001) Fractionation of Fe isotopes by soil microbes and organic acids. *Geology* **29**, 535–538.

Brasser R. and Mojzsis S. J. (2020) The partitioning of the inner and outer Solar System by a structured protoplanetary disk. *Nat. Astron.* **4**, 492–499.

Brennecka G. A. and Wadhwa M. (2012) Uranium isotope compositions of the basaltic angrite meteorites and the chronological implications for the early Solar System. *Proc. Natl. Acad. Sci. U. S. A.* **109**, 9299–9303.

Buchwald V. F. (1975) Handbook of Iron Meteorites: Their History, Distribution, Composition and Structure 1418 pp. University of California Press.

Canup R. M. and Asphaug E. (2001) Origin of the Moon in a giant impact near the end of the Earth's formation. *Nature* **412**, 708–712.

Canup R. M. (2012) Composition via a Giant Impact. *Science* **338**, 1052–1056.

Cardinal D., Alleman L. Y., De Jong J., Ziegler K. and André L. (2003) Isotopic composition of silicon measured by multicollector plasma source mass spectrometry in dry plasma mode. *J. Anal. At. Spectrom.* **18**, 213–218.

Casanova I., Keil K. and Newsom H. E. (1993) Composition of metal in aubrites: Constraints on core formation. *Geochim. Cosmochim. Acta* **57**, 675–682.

Castillo-Rogez J., Johnson T. V., Lee M. H., Turner N. J., Matson D. L. and Lunine, J. (2009) ^{26}Al decay: Heat production and a revised age for Iapetus. *Icarus* **204**, 658–662.

Chakrabarti R. and Jacobsen S. B. (2010) Silicon isotopes in the inner Solar System: Implications for core formation, solar nebular processes and partial melting. *Geochim. Cosmochim. Acta* **74**, 6921–6933.

Chen X., Lapen T. J. and Chafetz H. S. (2017) Accurate and Precise Silicon Isotope Analysis of Sulfur- and Iron-Rich Samples by MC-ICP-MS. *Geostand. Geoanalytical Res.* **41**, 427–435.

Collinet M. and Grove T. L. (2020) Widespread production of silica- and alkali-rich melts at the onset of planetesimal melting. *Geochim. Cosmochim. Acta* **277**, 334–357.

Connolly, Jr., H. C., Smith C., Benedix G., Folco L., Righter K., Zipfel J., Yamaguchi A. and Chennaoui Aoudjehane H. (2007) The Meteoritical Bulletin, No. 93, March 2008. *Meteorit. Planet. Sci.* **43**, 571–632.

Corgne A., Keshav S., Wood B. J., McDonough W. F. and Fei Y. (2008) Metal-silicate partitioning and constraints on core composition and oxygen fugacity during Earth accretion. *Geochim. Cosmochim. Acta* **72**, 574–589.

Craddock P. R. and Dauphas N. (2011) Iron Isotopic Compositions of Geological Reference Materials and Chondrites. *Geostand. Geoanalytical Res.* **35**, 101–123.

Craddock P. R., Warren J. M. and Dauphas N. (2013) Abyssal peridotites reveal the near-chondritic Fe isotopic composition of the Earth. *Earth Planet. Sci. Lett.* **365**, 63–76.

Crossley S. D., Ash R. D., Sunshine J. M., Corrigan C. M., McCoy T. J., Mittlefehldt D. W. and Puchtel I. S. (2020) Sulfide-dominated partial melting pathways in brachinites. *Meteorit. Planet. Sci.* **55**, 2021–2043.

Ćuk M. and Stewart S. T. (2012) Making the moon from a fast-spinning earth: A giant impact followed by resonant despinning. *Science* **338**, 1047–1052.

Dauphas N., Janney P. E., Mendybaev R. A., Wadhwa M., Richter F. M., Davis A. M., Van Zuilen M., Hines R. and Foley C. N. (2004) Chromatographic separation and multicollection-ICPMS analysis of iron. Investigating mass-dependent and -independent isotope effects. *Anal. Chem.* **76**, 5855–5863.

Dauphas N. and Rouxel O. (2006) Mass spectrometry and natural variations of iron isotopes. *Mass Spectrom. Rev.* **25**, 515–550.

Dauphas N., Craddock P. R., Asimow P. D., Bennett V. C., Nutman A. P. and Ohnenstetter D. (2009) Iron isotopes may reveal the redox conditions of mantle melting from Archean to Present. *Earth Planet. Sci. Lett.* **288**, 255–267.

Dauphas N., Roskosz M., Alp E. E., Neuville D. R., Hu M. Y., Sio C. K., Tissot F. L. H., Zhao J., Tissandier L., Médard E. and Cordier C. (2014a) Magma redox and structural controls on iron isotope variations in Earth's mantle and crust. *Earth Planet. Sci. Lett.* **398**, 127–140.

Dauphas N., Burkhardt C., Warren P. H. and Teng F. Z. (2014b) Geochemical arguments for an Earth-like Moon-forming impactor. *Philos. Trans. R. Soc. A Math. Phys. Eng. Sci.* **372**.

Dauphas N., Poitrasson F., Burkhardt C., Kobayashi H. and Kurosawa K. (2015) Planetary and meteoritic Mg/Si and δ^{30}Si variations inherited from solar nebula chemistry. *Earth Planet. Sci. Lett.* **427**, 236–248.

Dauphas N. (2017) The isotopic nature of the Earth's accreting material through time. *Nature* **541**, 521–524.

Dauphas N., John S. G. and Rouxel O. (2017) Iron isotope systematics. In Non-Traditional Stable Isot. *Reviews in Mineralogy and Geochemistry* **82**, 415–510.

Day J. M. D., Ash R. D., Liu Y., Bellucci J. J., Rumble D., McDonough W. F., Walker R. J. and Taylor L. A. (2009) Early formation of evolved asteroidal crust. *Nature* **457**, 179–182.

Day J. M. D., Walker R. J., Ash R. D., Liu Y., Rumble D., Irving A. J., Goodrich C. A., Tait K., McDonough W. F. and Taylor L. A. (2012) Origin of felsic achondrites Graves Nunataks 06128 and 06129, and ultramafic brachinites and brachinite-like achondrites by partial melting of volatile-rich primitive parent bodies. *Geochim. Cosmochim. Acta* **81**, 94–128.

Day J. M. D., Corder C. A., Assayag N. and Cartigny P. (2019) Ferrous oxide-rich asteroid achondrites. *Geochim. Cosmochim. Acta* **266**, 544–567.

Desch S. J. and Robinson K. L. (2019) A unified model for hydrogen in the Earth and Moon: No one expects the Theia contribution. *Chemie der Erde* **79,** 125546.

Desch S. J., Kalyaan A. and Alexander C. M. O. (2018) The Effect of Jupiter's Formation on the Distribution of Refractory Elements and Inclusions in Meteorites. *Astrophys. J. Suppl. Ser.* **238**, 11.

Dunlap D. R., Wadhwa M. and Romaniello S. R. (2014) ^{26}Al-^{26}Mg systematics in the unusual ungrouped achondrite NWA 7325 and the eucrite Juvinas. *Lunar Planet. Sci. XLV.* #2186 (abstract).

Dunlap D. R., Ku Y-J., Garvie L. A. J. and Wadhwa M. (2015) Petrology of ungrouped and anomalous achondrites SaU 493, NWA 4470, NWA 6962 and NWA 5297. *Lunar Planet. Sci. XLVI.* #2570 (abstract).

Dunlap D. R. (2021) Chronology of Planetesimal Differentiation based on the Timing of Achondrite Formation in the Early Solar System. PhD thesis.

Elardo S. M. and Shahar A. (2017) Non-chondritic iron isotope ratios in planetary mantles as a result of core formation. *Nat. Geosci.* **10**, 317–321.

Elardo S. M., Shahar A., Mock T. D. and Sio C. K. (2019) The effect of core composition on iron isotope fractionation between planetary cores and mantles. *Earth Planet. Sci. Lett.* **513**, 124–134.

Engström E., Rodushkin I., Baxter D. C. and Öhlander B. (2006) Chromatographic purification for the determination of dissolved silicon isotopic compositions in natural waters by high-resolution multicollector inductively coupled plasma mass spectrometry. *Anal. Chem.* **78**, 250–257.

Fischer R. A., Nakajima Y., Campbell A. J., Frost D. J., Harries D., Langenhorst F., Miyajima N., Pollok K. and Rubie D. C. (2015) High pressure metal – silicate partitioning of Ni, Co, V, Cr, Si an O. *Geochim. Cosmochim. Acta* **167**, 177–194.

Fitoussi C., Bourdon B., Kleine T., Oberli F. and Reynolds B. C. (2009) Si isotope systematics of meteorites and terrestrial peridotites: implications for Mg/Si fractionation in the solar nebula and for Si in the Earth's core. *Earth Planet. Sci. Lett*. **287**, 77–85.

Fitoussi C. and Bourdon B. (2012) Silicon isotope evidence against an enstatite chondrite earth. *Science* **335**, 1477–1480.

Floss C., Taylor L. A., Promprated P. and Rumble D. (2005) Northwest Africa 011: A "Eucritic" basalt from a non-eucrite parent body. *Meteorit. Planet. Sci.* **40**, 343–360.

Flynn G. J., Consolmagno G. J., Brown P. and Macke, R. J. (2018) Physical properties of the stone meteorites: Implications for the properties of their parent bodies. *Chemie der Erde* **78**, 269–298.

Frossard P., Boyet M., Bouvier A., Hammouda T. and Monteux J. (2019) Evidence for anorthositic crust formed on an inner solar system planetesimal. *Geochemical Perspect. Lett.* **11**, 28–32.

Frost B. R. (1991) Introduction to oxygen fugacity and its petrologic importance. *Reviews in Mineralogy and Geochemistry* **25**, 1-9.

Gajos N. A., Lundstrom C. C. and Taylor A. H. (2016) Spatially controlled Fe and Si isotope variations: an alternative view on the formation of the Torres del Paine pluton. *Contrib. to Mineral. Petrol.* **171**, 1–20.

Gardner-Vandy K. G., Lauretta D. S., Greenwood R. C., McCoy T. J., Killgore M. and Franchi I. A. (2012) The Tafassasset primitive achondrite: Insights into initial stages of planetary differentiation. *Geochim. Cosmochim. Acta* **85**, 142–159.

Gardner-Vandy K. G., Lauretta D. S. and McCoy T. J. (2013) A petrologic, thermodynamic and experimental study of brachinites: Partial melt residues of an R chondrite-like precursor. *Geochim. Cosmochim. Acta* **122**, 36–57.

Garvie L. A. J. (2017) The Meteoritical Bulletin No. 103. *Meteorit. Planet. Sci.* **52**, 122-123.

Georg R. B., Reynolds B. C., Frank M. and Halliday A. N. (2006) New sample preparation techniques for the determination of Si isotopic compositions using MC-ICPMS. *Chem. Geol.* **235**, 95–104.

Georg R. B., Halliday A. N., Schauble E. A. and Reynolds B. C. (2007) Silicon in the Earth's core. *Nature* **447**, 1102–1106.

Gessmann C. K., Wood B. J., Rubie D. C. and Kilburn M. R. (2001) Solubility of silicon in liquid metal at high pressure: Implications for the composition of the Earth's core. *Earth Planet. Sci. Lett.* **184**, 367–376.

Ghanbarzadeh S., Hesse M. A., Prodanović M. and Schubert G. (2017) Percolative core formation in planetesimals enabled by hysteresis in metal connectivity. *Proc. Natl. Acad. Sci. U. S. A.* **114**, 13406–13411.

Goldstein J. I., Scott E. R. D. and Chabot N. L. (2009) Iron meteorites: Crystallization, thermal history, parent bodies, and origin. *Chemie der Erde* **69**, 293–325.

Goodrich C. A and Delaney J. S. (2000) Fe/Mg–Fe/Mn relations of meteorites and primary heterogeneity of primitive achondrite parent bodies. *Geochim. Cosmochim. Acta* **64**, 149–160.

Goodrich C. A., Kita N. T., Spicuzza M. J., Valley J. W., Zipfel J., Mikouchi T. and Miyamoto M. (2011) The Northwest Africa 1500 meteorite: Not a ureilite, maybe a brachinite. *Meteorit. Planet. Sci.* **45**, 1906–1928.

Goodrich C. A., Kita N. T., Sutton S. R., Wirick S. and Gross J. (2017a) The Miller Range 090340 and 090206 meteorites: Identification of new brachinite-like achondrites with implications for the diversity and petrogenesis of the brachinite clan. *Meteorit. Planet. Sci.* **52**, 949–978.

Goodrich C. A., Kita N. T., Yin Q. Z., Sanborn M. E., Williams C. D., Nakashima D., Lane M. D. and Boyle S. (2017b) Petrogenesis and provenance of ungrouped achondrite Northwest Africa 7325 from petrology, trace elements, oxygen, chromium and titanium isotopes, and mid-IR spectroscopy. *Geochim. Cosmochim. Acta* **203**, 381–403.

Grant F.S. (1954) The geological significance of variations in the abundances of the isotopes of silicon in rocks. *Geochim. Cosmochim. Acta* **5**, 225–242.

Greenwood R. C., Franchi I. A., Gibson J. M. and Benedix G. K. (2012) Oxygen isotope variation in primitive achondrites: The influence of primordial, asteroidal and terrestrial processes. *Geochim. Cosmochim. Acta* **94**, 146–163.

Greenwood R. C., Burbine T. H., Miller M. F. and Franchi I. A. (2017) Melting and differentiation of early-formed asteroids: The perspective from high precision oxygen isotope studies. *Chemie der Erde - Geochemistry* **77**, 1–43.

Gregory T., Luu T. H., Coath C. D., Russell S. S. and Elliott T. (2020) Primordial formation of major silicates in a protoplanetary disc with homogeneous 26Al/27Al. *Sci. Adv.* **6**, 1–9.

Halliday A. N., Lee D. C., Christensen J. N., Walder A. J., Freedman P. A., Jones C. E., Hall C. M., Yi W. and Teagle D. (1995) Recent developments in inductively coupled plasma magnetic sector multiple collector mass spectrometry. *Int. J. Mass Spectrom. Ion Process.* **146**–**147**, 21–33.

Halliday A. N., Lee D. C., Christensen J. N., Rehkämper M., Yi W., Luo X., Hall C. M., Ballentine C. J., Pettke T. and Stirling C. (1998) Applications of multiple collector-ICPMS to cosmochemistry, geochemistry, and paleoceanography. *Geochim. Cosmochim. Acta* **62**, 919–940.

Hans U., Kleine T. and Bourdon B. (2013) Rb-Sr chronology of volatile depletion in differentiated protoplanets: BABI, ADOR and ALL revisited. *Earth Planet. Sci. Lett.* **374**, 204–214.

Hevey P. J. and Sanders I. S. (2006) A model for planetesimal meltdown by 26Al and its implications for meteorite parent bodies. *Meteorit. Planet. Sci.* **41**, 95–106.

Hibiya Y., Archer G. J., Tanaka R., Sanborn M. E., Sato Y., Iizuka T., Ozawa K., Walker R. J., Yamaguchi A., Yin Q. Z., Nakamura T. and Irving A. J. (2019) The origin of the unique achondrite Northwest Africa 6704: Constraints from petrology, chemistry and Re–Os, O and Ti isotope systematics. *Geochim. Cosmochim. Acta* **245**, 597–627.

Hin R. C., Schmidt M. W. and Bourdon B. (2012) Experimental evidence for the absence of iron isotope fractionation between metal and silicate liquids at 1 GPa and 1250–1300 °C and its cosmochemical consequences. *Geochim. Cosmochim. Acta* **93**, 164–181.

Hin R. C., Fitoussi C., Schmidt M. W. and Bourdon B. (2014) Experimental determination of the Si isotope fractionation factor between liquid metal and liquid silicate. *Earth Planet. Sci. Lett.* **387**, 55–66.

Hin R. C., Coath C. D., Carter P. J., Nimmo F., Lai Y. J., Pogge von Strandmann P. A. E., Willbold M., Leinhardt Z. M., Walter M. J. and Elliott T. (2017) Magnesium isotope evidence that accretional vapour loss shapes planetary compositions. *Nature* **549**, 511–527.

Hirschmann M. M. (1991) Thermodynamics of multicomponent olivines and the solution properties of (Ni, Mg, Fe)$_2$SiO$_4$ and (Ca, Mg, Fe)$_2$SiO$_4$ olivines. *Am. Mineral.* **76**, 1232–1248.

Hohenberg C. M. and Pravdivtseva O. V. (2008) I-Xe dating: From adolescence to maturity. *Chemie der Erde* **68**, 339–351.

Irving A. J. and Kuehner S. M. (2010) The Meteoritical Bulletin No. 98. *Meteorit. Planet. Sci.* **45,** 1533.

Irving A. J. and Kuehner S. M. (2012a) The Meteoritical Bulletin No. 100. *Meteorit. Planet. Sci.* **49**, E30.

Irving A. J. and Kuehner S. M. (2012b) The Meteoritical Bulletin No. 99. *Meteorit. Planet. Sci.* **47**, E24.

Irving A. J. and Kuehner S. M. (2015) The Meteoritical Bulletin No. 101. *Meteorit. Planet. Sci.* **50**, 1-136.

Irving A. J. and Kuehner S. M. (2017a) Meteoritical Bulletin No. 104. *Meteorit. Planet. Sci.* **1**.

Irving A. J. and Kuehner S. M. (2017b) The Meteoritical Bulletin No. 105. *Meteorit. Planet. Sci.* **52**.

Irving A. J., Kuehner S. M., Bunch T. E., Ziegler K., Chen G., Herd C. D. K., Conrey R. M. and Ralew S. (2013) Ungrouped mafic achondrite Northwest Africa 7325: A reduced, iron-poor cumulate olivine gabbro from a differentiated planetary parent body. *Lunar Planet. Sci. XLIV.* #2164 (abstract).

Jacobsen B., Yin Q. zhu, Moynier F., Amelin Y., Krot A. N., Nagashima K., Hutcheon I. D. and Palme H. (2008) 26Al-26Mg and 207Pb-206Pb systematics of

Allende CAIs: Canonical solar initial 26Al/27Al ratio reinstated. *Earth Planet. Sci. Lett.* **272**, 353–364.

Jambon A., Humayun M. and Barrat J. A. (2012) Northwest Africa 6693: a unique achondritic cumulate. *Lunar Planet. Sci. Proceedings* **43**, #2099.

Javoy M., Kaminski E., Guyot F., Andrault D., Sanloup C., Moreira M., Labrosse S., Jambon A., Agrinier P., Davaille A. and Jaupart C. (2010) The chemical composition of the Earth: Enstatite chondrite models. *Earth Planet. Sci. Lett.* **293**, 259–268.

Johnson C. M., Beard B. L. and Albarede F. (2004) Geochemistry of Non-Traditional Stable Isotopes. *Rev. Mineral Geochem.* **55**. Mineralogical Society of America.

Jordan M. K., Tang H. L., Kohl I. E. and Young E. D. (2019) Iron isotope constraints on planetesimal core formation in the early solar system. *Geochim. Cosmochim. Acta* **246**, 461–477.

Jurewicz A. J. G., Mittlefehldt D. W. and Jones J. H. (1993) Experimental partial melting of the Allende (CV) and Murchison (CM) chondrites and the origin of asteroidal basalts. *Geochim. Cosmochim. Acta* **57**, 2123–2139.

Kadlag Y., Tatzel M., Frick D. A. and Becker H. (2019) The origin of unequilibrated EH chondrites – Constraints from in situ analysis of Si isotopes, major and trace elements in silicates and metal. *Geochim. Cosmochim. Acta* **267**, 300–321.

Kallemeyn G.W. and Wasson J.T. (1986) Compositions of enstatite (EH3, EH4,5 and EL6) chondrites: implications regarding their formation. *Geochim. Cosmochim. Acta* **50**, 2153-2164.

Keil K. (1989) Enstatite meteorites and their parent bodies. *Meteoritics.* **24**, 195–208.

Keil K. (2010) Enstatite achondrite meteorites (aubrites) and the histories of their asteroidal parent bodies. *Chemie der Erde* **70**, 295–317.

Keil K. (2012) Angrites, a small but diverse suite of ancient, silica-undersaturated volcanic-plutonic mafic meteorites, and the history of their parent asteroid. *Chemie der Erde* **72**, 191–218.

Keil K. (2014) Brachinite meteorites: Partial melt residues from an FeO-rich asteroid. Chemie der Erde **74**, 311–329.

Keil K., Ntaflos T., Taylor G. J., Brearley A. J., Newsom H. E. and Romig, A. D. (1989) The Shallowater aubrite: Evidence for origin by planetesimal impacts. *Geochim. Cosmochim. Acta* **53**, 3291–3307.

Kilburn M. R. and Wood B. J. (1997) Metal-silicate partitioning and the incompatibility of S and Si during core formation. *Earth Planet. Sci. Lett.* **152**, 139–148.

Kita N. T., Yin Q. Z., Macpherson G. J., Ushikubo T., Jacobsen B., Nagashima K., Kurahashi E., Krot A. N. and Jacobsen S. B. (2013) ^{26}Al-^{26}Mg isotope systematics of the first solids in the early solar system. *Meteorit. Planet. Sci.* **48**, 1383–1400.

Kleine, T. and Wadhwa, M. (2017) Chronology of Planetesimal Differentiation, In *Planetesimals*, Edited by L.T. Elkins-Tanton and B.P. Weiss Cambridge University Press.

Kleine T., Mezger K., Palme H., Scherer E. and Münker C. (2005) Early core formation in asteroids and late accretion of chondrite parent bodies: Evidence from 182Hf-182W in CAIs, metal-rich chondrites, and iron meteorites. *Geochim. Cosmochim. Acta* **69**, 5805–5818.

Kleine T., Hans U., Irving A. J. and Bourdon B. (2012) Chronology of the angrite parent body and implications for core formation in protoplanets. *Geochim. Cosmochim. Acta* **84**, 186–203.

Kleine T., Budde G., Burkhardt C., Kruijer T. S., Worsham E. A., Morbidelli A. and Nimmo F. (2020) The Non-carbonaceous–Carbonaceous Meteorite Dichotomy. *Space Sci. Rev.* **216,** 27 pp.

Koefoed P., Amelin Y., Yin Q. Z., Wimpenny J., Sanborn M. E., Iizuka T. and Irving A. J. (2016) U-Pb and Al-Mg systematics of the ungrouped achondrite Northwest Africa 7325. Geochim. Cosmochim. Acta **183**, 31–45.

Kong, P., Mori, T. & Ebihara, M. Compositional continuity of enstatite chondrites and implications for heterogeneous accretion of the enstatite chondrite parent body. *Geochim. Cosmochim. Acta* **61**, 4895–4914 (1997).

Korotchantseva E. V, Ivanova M. A., Lorenz C. A., Bouikine A. I., Trieloff M., Nazarov M. A., Promprated P., Anand M. and Taylor L. A. (2003) Major and trace element chemistry and Ar-Ar age of the NWA 011 achondrite. *Lunar Planet. Sci. XXXIV.* #1575 (abstract).

Kruijer T. S., Burkhardt C., Budde G. and Kleine T. (2017) Age of Jupiter inferred from the distinct genetics and formation times of meteorites. *Proc. Natl. Acad. Sci. U. S. A.* **114**, 6712–6716.

Kruijer T. S., Kleine T. and Borg L. E. (2020) The great isotopic dichotomy of the early Solar System. *Nat. Astron.* **4**, 32–40.

Kullerud G. (1963) The Fe–Ni–S system. Carnegie Institution of Washington Year-book. Report of the Director of the Geophysical Laboratory, vol. 62., pp. 175–189.

Lichtenberg T., Drążkowska J., Schönbächler M., Golabek G. J. and Hands T. O. (2021) Bifurcation of planetary building blocks during Solar System formation. *Science* **371**, 365–370.

Liu J., Dauphas N., Roskosz M., Hu M. Y., Yang H., Bi W., Zhao J., Alp E. E., Hu J. Y. and Lin J. F. (2017) Iron isotopic fractionation between silicate mantle and metallic core at high pressure. *Nat. Commun.* **8**, 1–6.

Liu Y., Spicuzza M. J., Craddock P. R., Day J. M. D., Valley J. W., Dauphas N. and Taylor L. A. (2010) Oxygen and iron isotope constraints on near-surface fractionation effects and the composition of lunar mare basalt source regions. *Geochim. Cosmochim. Acta* **74**, 6249–6262.

Lodders K. (2003) Solar System Abundances and Condensation Temperatures of the Elements. *Astrophys. J.* **591**, 1220–1247.

Lodders, K., Palme, H. and Wlotzka, F. (1993) Trace elements in mineral separates of the Peña Blanca Spring aubrite: Implications for the evolution of the aubrite parent body. *Meteoritics.* **28**, 538-551.

Lunning N. G., Gardner-Vandy K. G., Sosa E. S., McCoy T. J., Bullock E. S. and Corrigan C. M. (2017) Partial melting of oxidized planetesimals: An experimental study to test the formation of oligoclase-rich achondrites Graves Nunataks 06128 and 06129. Geochim. Cosmochim. Acta **214**, 73–85.

Ma Z. (2001) Thermodynamic description for concentrated metallic solutions using interaction parameters. *Metall. Mater. Trans. B Process Metall. Mater. Process. Sci.* **32**, 87–103.

Macke R. J. Consolmagno, G. J., Britt D. T. and Hutson, M. L. (2010) Enstatite chondrite density, magnetic susceptibility, and porosity. *Meteorit. Planet. Sci.* **45**, 1513–1526.

Mann U., Frost D. J. and Rubie D. C. (2008) The wetting ability of Si-bearing liquid Fe-alloys in a solid silicate matrix-percolation during core formation under reducing conditions? *Phys. Earth Planet. Inter.* **167**, 1–7.

Mastrobuono-Battisti A., Perets H. B. and Raymond S. N. (2015) A primordial origin for the compositional similarity between the Earth and the Moon. *Nature* **520**, 212–215.

McCoy T. J., and Bullock E. S. (2017) Differentiation Under Highly Reducing Conditions: Insights from Enstatite Meteorites and Mercury. Planetesimals, 71-91.

McCoy T. J., Dickinson T. L. and Lofgren G. E. (1999) Partial melting of the Indarch (EH4) meteorite: A textural, chemical, and phase relations view of melting and melt migration. *Meteorit. Planet. Sci.* **34**, 735–746.

Méheut M. and Schauble E. A. (2014) Silicon isotope fractionation in silicate minerals: Insights from first-principles models of phyllosilicates, albite and pyrope. Geochim. Cosmochim. Acta **134**, 137–154.

Méheut M., Lazzeri M., Balan E. and Mauri F. (2009) Structural control over equilibrium silicon and oxygen isotopic fractionation: A first-principles density-functional theory study. Chem. Geol. **258**, 28–37.

Meier M. M. M., Reufer A. and Wieler R. (2014) On the origin and composition of Theia: Constraints from new models of the Giant Impact. *Icarus* **242**, 316–328.

Mikouchi T., McKay G. and Jones J. (2008) Petrogenesis and crystallization history of quenched angrites. *Meteorit. Planet. Sci.* 43, A98.

Mittlefehldt, D. W. (2014) Achondrites. Treatise on Geochemistry: Second Edition vol. 1.

Mittlefehldt W. and Berkeley J. L. (2002) Petrology and Geochemistry of paired brachinites EET 99402 and EET 99407. *Lunar Planet. Sci. XXXIII* #1008 (abstract).

Mittlefehldt, D.W., McCoy, T.J., Goodrich, C.A. and Kracher, A. (1998) Non-chondritic meteorites from asteroidal bodies. *Reviews in Mineralogy and Planetary Materials*, **36**, Mineralogical Society of America, 1-195.

Mittlefehldt D. W., Bogard D. D., Berkley J. L. and Garrison D. H. (2003) Brachinites: igneous rocks from a differentiated asteroid. Meteorit. Planet. Sci. 38, 1601–1625.

Morbidelli A., Libourel G., Palme H., Jacobson S. A. and Rubie D. C. (2020) Subsolar Al/Si and Mg/Si ratios of non-carbonaceous chondrites reveal planetesimal formation during early condensation in the protoplanetary disk. Earth Planet. Sci. Lett. **538**, 1–10.

Moynier F., Yin Q. Z. and Schauble E. (2011a) Isotopic evidence of Cr partitioning into Earth's core. *Science* **331**, 1417–1420.

Moynier F., Paniello R. C., Gounelle M., Albarède F., Beck P., Podosek F. and Zanda B. (2011b) Nature of volatile depletion and genetic relationships in enstatite chondrites and aubrites inferred from Zn isotopes. *Geochim. Cosmochim. Acta* **75**, 297–307.

Moynier F., Day J. M. D., Okui W., Yokoyama T., Bouvier A., Walker R. J. and Podosek F. A. (2012) Planetary-scale strontium isotopic heterogeneity and the age of volatile depletion of early Solar System materials. *The Astrophysical Journa*l **758** (7 pp).

Moynier F., Deng Z., Lanteri A., Martins R., Chaussidon M., Savage P. and Siebert J. (2020) Metal-silicate silicon isotopic fractionation and the composition of the bulk Earth. *Earth Planet. Sci. Lett.* **549**, 116468.

Needham A. W., Porcelli D. and Russell S. S. (2009) An Fe isotope study of ordinary chondrites. *Geochim. Cosmochim. Acta* **73**, 7399–7413.

Nehru C. E., Prinz M., Delaney J. S., Dreibus G., Palme H., Spettel B., and Wänke H. (1983) Brachina: a new type of meteorite, not a chassignite. Proc. 14th Lunar Planetary Science Conference. *J. Geophys. Res*. **88**, B237–B244 (suppl.).

Nehru C. E., Prinz M., Weisberg M. K., Ebihara M. E., Clayton R. N. and Mayeda T. K. (1992) Brachinites: a new primitive achondrite group. *Meteoritics* **27**, 267 (abstr.).

Nehru C. E., Prinz M., Weisbert M. K., Ebihara M. E., Clayton R. N. and Mayeda T. K. (1996) A new brachinite and petrogenesis of the group. *Lunar Planet. Sci. XXVII.* #943 (abstract).

Norris T. L., Gancarz A. J., Rokop D. J. and Thomas K. W. (1983) Half-life of ^{26}Al. *J. Geophys. Res. Solid Earth* **88**, B331–B333.

Ntaflos T., Keil K. and Newsom, H. E. (1988) Khor Temiki: An enstatite achondrite with evidence of mixing of metal and sulfides from separate sources. *Lunar Planet. Sci. XIX,* 870–871.

Oelze M., Schuessler J. A. and Von Blanckenburg F. (2016) Mass bias stabilization by Mg doping for Si stable isotope analysis by MC-ICP-MS. *J. Anal. At. Spectrom.* **31**, 2094–2100.

Okada A., Keil K., Taylor G. J. and Newsom, H. (1988) Igneous history of the aubrite parent asteroid: evidence from the Norton County enstatite achondrite. *Meteoritics* **23**, 59–74.

Opeil C. P., Consolmagno G. J.and Britt, D. T. (2010) The thermal conductivity of meteorites: New measurements and analysis. *Icarus* **208**, 449–454.

Opeil C. P., Consolmagno G. J., Safarik D. J. and Britt, D. T. (2012) Stony meteorite thermal properties and their relationship with meteorite chemical and physical states. *Meteorit. Planet. Sci.* **47**, 319–329.

Pahlevan K. and Stevenson D. J. (2007) Equilibration in the aftermath of the lunar-forming giant impact. *Earth Planet. Sci. Lett.* **262**, 438–449.

Pahlevan K., Stevenson D. J. and Eiler J. M. (2011) Chemical fractionation in the silicate vapor atmosphere of the Earth. *Earth Planet. Sci. Lett.* **301**, 433–443.

Poitrasson F. (2007) Does planetary differentiation really fractionate iron isotopes? *Earth Planet. Sci. Lett.* **256**, 484–492.

Poitrasson F. and Zambardi T. (2015) An Earth-Moon silicon isotope model to track silicic magma origins. *Geochim. Cosmochim. Acta* **167**, 301–312.

Poitrasson F., Halliday A. N., Lee D. C., Levasseur S. and Teutsch N. (2004) Iron isotope differences between Earth, Moon, Mars and Vesta as possible records of contrasted accretion mechanisms. *Earth Planet. Sci. Lett.* **223**, 253–266.

Poitrasson, F., Levasseur, S. and Teutsch, N. (2005) Significance of iron isotope mineral fractionation in pallasites and iron meteorites for the core-mantle differentiation of terrestrial planets. *Earth Planet. Sci. Lett.* **234**, 151–164.

Poitrasson, F., Roskosz, M. and Corgne, A. (2009) No iron isotope fractionation between molten alloys and silicate melt to 2000 °C and 7.7 GPa: Experimental evidence and implications for planetary differentiation and accretion. *Earth Planet. Sci. Lett.* **278**, 376–385.

Poitrasson F., Zambardi T., Magna T. and Neal C. R. (2019) A reassessment of the iron isotope composition of the Moon and its implications for the accretion and differentiation of terrestrial planets. *Geochim. Cosmochim. Acta* **267**, 257–274.

Polyakov V. B. (2009) Equilibrium iron isotope fractionation at core-mantle boundary conditions. *Science* **323**, 912–914.

Pringle E. A., Savage P. S., Badro J., Barrat J. A. and Moynier F. (2013a) Redox state during core formation on asteroid 4-Vesta. *Earth Planet. Sci. Lett.* **373**, 75–82.

Pringle E. A., Savage P. S., Jackson M. G., Barrat J. A. and Moynier F. (2013b) Si isotope homogeneity of the solar nebula. *Astrophys. J.* **779**.

Pringle E. A., Moynier F., Savage P. S., Badro J. and Barrat J. A. (2014) Silicon isotopes in angrites and volatile loss in planetesimals. Proc. Natl. Acad. Sci. U. S. A. **111**, 17029–17032.

Prinz, M. (1998) Brachinites: a developing story. *Meteorit. Planet. Sci.* **33**, 3–4.

Qin L., Dauphas N., Wadhwa M., Masarik J. and Janney P. E. (2008) ^{182}Hf–^{182}W chronometry and thermal modeling. *Earth and Planetary Science Letters* **273**, 94-104.

Rabin S., Blanchard M., Pinilla C., Poitrasson F. and Gregoire M. (2021) First-principles calculation of iron and silicon isotope fractionation between Fe-bearing minerals at magmatic temperatures: The importance of second atomic neighbors. *Geochim. Cosmochim. Acta* **304**, 101–118.

Reufer A., Meier M. M. M., Benz W. and Wieler R. (2012) A hit-and-run giant impact scenario. *Icarus* **221**, 296–299.

Reynolds B. C., Aggarwal J., André L., Baxter D., Beucher C., Brzezinski M. A., Engström E., Georg R. B., Land M., Leng M. J., Opfergelt S., Rodushkin I., Sloane H. J., Van Den Boorn S. H. J. M., Vroon P. Z. and Cardinal D. (2007) An inter-laboratory comparison of Si isotope reference materials. *J. Anal. At. Spectrom.* **22**, 561–568.

Richter F. M. (2004) Timescales determining the degree of kinetic isotope fractionation by evaporation and condensation. *Geochim. Cosmochim. Acta* **68**, 4971–4992.

Richter F. M., Janney P. E., Mendybaev R. A., Davis A. M. and Wadhwa M. (2007) Elemental and isotopic fractionation of Type B CAI-like liquids by evaporation. *Geochim. Cosmochim. Acta* **71**, 5544–5564.

Righter K. and Drake M. J. (1996) Core formation in Earth's moon, Mars, and Vesta. *Icarus* **124**, 513–529.

Righter K. and Neff K. E. (2007) Temperature and oxygen fugacity constraints on CK and R chondrites and implications for water and oxidation in the early solar system. Polar Science **1**, 25–44.

Righter K., Yang H., Costin G. and Downs R. T. (2008) Oxygen fugacity in the Martian mantle controlled by carbon: New constraints from the nakhlite MIL 03346. *Meteorit. Planet. Sci.* **43**, 1709–1723.

Righter K., Sutton S. R., Danielson L., Pando K. and Newville M. (2016) Redox variations in the inner solar system with new constraints from vanadium XANES in spinels. *Am. Mineral.* **101**, 1928–1942.

Rouxel O., Bekker A. and Edwards K.J. (2005) Iron Isotope Constraints on the Archean and Paleoproterozoic Ocean Redox State. Science **307**, 1088–1091.

Rubie D. C., Frost D. J., Mann U., Asahara Y., Nimmo F., Tsuno K., Kegler P., Holzheid A. and Palme H. (2011) Heterogeneous accretion, composition and core-mantle differentiation of the Earth. *Earth Planet. Sci. Lett.* **301**, 31–42.

Ryder, G., (1982) Siderophiles in the Brachina meteorite: impact melting? *Nature* **299**, 805–807.

Sack R. O. and Ghiorso M. S. (1989) Importance of considerations of mixing properties in establishing an internally consistent thermodynamic database: thermochemistry of minerals in the system Mg_2SiO_4–Fe_2SiO_4–SiO_2. *Contrib. Mineral Petrol.* 102, 41–68.

Sack R. O. and Ghiorso M. S. (1991a) Chromite as a petrogenetic indicator. In Oxide Minerals: Petrologic and Magnetic Significance, vol. 25 (ed. D. H. Lindsley), pp. 323–353. *Reviews in Mineralogy.* Mineralogical Society of America, Washington DC.

Sack R. O. and Ghiorso M. S. (1991b) Chromian spinels as petrogenetic indicators: thermodynamics and petrological applications. *Am. Mineral.* 76, 827–847.

Sanborn M. E., Carlson R. W. and Wadhwa M. (2015) ^{147,146}Sm-^{143,142}Nd, ^{176}Lu-^{176}Hf, and ^{87}Rb-^{87}Sr systematics in the angrites: Implications for chronology and processes on the angrite parent body. *Geochim. Cosmochim. Acta* **171**, 80–99.

Sanborn M. E., Wimpenny J., Williams C. D., Yamakawa A., Amelin Y., Irving A. J. and Yin Q. (2019) ScienceDirect Carbonaceous achondrites Northwest Africa 6704/6693: Milestones for early Solar System chronology and genealogy. *Geochim. Cosmochim. Acta* **245**, 577–596.

Sanloup C., Guyot F., Gillet P. and Fei Y. (2002) Physical properties of liquid Fe alloys at high pressure and their bearings on the nature of metallic planetary cores. *J. Geophys. Res.: Solid Earth*. **107**, 2272-2280.

Sarafian A. R., Hauri E. H., McCubbin F. M., Lapen T. J., Berger E. L., Nielsen S. G., Marschall H. R., Gaetani G. A., Righter K. and Sarafian E. (2017a) Early accretion of water and volatile elements to the inner Solar System: Evidence from angrites. *Philos. Trans. R. Soc. A Math. Phys. Eng. Sci.* **375**.

Sarafian A. R., Nielsen S. G., Marschall H. R., Gaetani G. A., Hauri E. H., Righter K. and Sarafian E. (2017b) Angrite meteorites record the onset and flux of water to the inner solar system. *Geochim. Cosmochim. Acta* **212**, 156–166.

Savage P. S. and Moynier F. (2013) Silicon isotopic variation in enstatite meteorites: Clues to their origin and Earth-forming material. *Earth Planet. Sci. Lett.* **361**, 487–496.

Savage P. S., Georg R. B., Armytage R. M. G., Williams H. M. and Halliday A. N. (2010) Silicon isotope homogeneity in the mantle. *Earth Planet. Sci. Lett.* **295**, 139–146.

Savage P. S., Georg R. B., Williams H. M., Burton K. W. and Halliday A. N. (2011) Silicon isotope fractionation during magmatic differentiation. *Geochim. Cosmochim. Acta* **75**, 6124–6139.

Savage P. S., Georg R. B., Williams H. M. and Halliday A. N. (2013) The silicon isotope composition of the upper continental crust. *Geochim. Cosmochim.* Acta **109**, 384–399.

Savage P. S., Armytage R. M. G., Georg R. B. and Halliday A. N. (2014) High temperature silicon isotope geochemistry. *Lithos* **190**–**191**, 500–519.

Schairer J. F. and Yoder, Jr., H. S. (1961) The system albite–forsterite–silica. Carnegie Inst. Washington Year Book 1959–1960, 69–70.

Schauble E. A. (2004) Applying stable isotope fractionation theory to new systems. *Rev. Mineral. Geochemistry* **55**, 65–111.

Scherstén A., Elliott T., Hawkesworth C., Russell S. and Masarik J. (2006) Hf-W evidence for rapid differentiation of iron meteorite parent bodies. *Earth Planet. Sci. Lett*. **241**, 530–542.

Schiller M., Connelly J. N., Glad A. C. Mikouchi T. and Bizzarro M. (2015) Early accretion of protoplanets inferred from a reduced inner solar system 26Al inventory. *Earth and Planetary Science Letters* **420**, 45–54.

Schoenberg R. and Blanckenburg F. von (2006) Modes of planetary-scale Fe isotope fractionation. *Earth Planet. Sci. Lett.* **252**, 342–359.

Schrader D. L., McCoy T. J. and Gardner-Vandy K. (2017) Relict chondrules in primitive achondrites: Remnants from their precursor parent bodies. *Geochim. Cosmochim. Acta* **205**, 295–312.

Sedaghatpour F. and Teng F. Z. (2016) Magnesium isotopic composition of achondrites. *Geochim. Cosmochim. Acta* **174**, 167–179.

Sedaghatpour F. and Jacobsen S. B. (2019) Magnesium stable isotopes support the lunar magma ocean cumulate remelting model for mare basalts. *Proc. Natl. Acad. Sci. U. S. A.* **116**, 73–78.

Shahar A. and Young E. D. (2020) An assessment of iron isotope fractionation during core formation. *Chem. Geol.* **554**, 119800.

Shahar A., Young E. D. and Manning C. E. (2008) Equilibrium high-temperature Fe isotope fractionation between fayalite and magnetite: An experimental calibration. *Earth Planet. Sci. Lett.* **268**, 330–338.

Shahar A., Ziegler K., Young E. D., Ricolleau A., Schauble E. A. and Fei Y. (2009) Experimentally determined Si isotope fractionation between silicate and Fe metal and implications for Earth's core formation. *Earth Planet. Sci. Lett.* **288**, 228–234.

Shahar A., Hillgren V. J., Young E. D., Fei Y., Macris C. A. and Deng L. (2011) High-temperature Si isotope fractionation between iron metal and silicate. *Geochim. Cosmochim. Acta* **75**, 7688–7697.

Shahar A., Hillgren V. J., Horan M. F., Mesa-Garcia J., Kaufman L. A. and Mock T. D. (2015) Sulfur-controlled iron isotope fractionation experiments of core formation in planetary bodies. *Geochim. Cosmochim. Acta* **150**, 253–264.

Shahar A., Schauble E. A., Caracas R., Gleason A. E., Reagan M., Xiao Y., Shu J. and Mao W. (2016) Pressure-dependent isotopic composition of iron alloys. *Science.* **352**, 580–582.

Shahar, A., Savage, P. and Moynier, F. (2017) Stable Isotope Evidence for the Differentiation of Planetesimals, In *Planetesimals*, Edited by L.T. Elkins-Tanton and B.P. Weiss Cambridge University Press.

Shearer C. K., Burger P. V., Neal C., Sharp Z., Spivak-Birndorf L., Borg L., Fernandes V. A., Papike J. J., Karner J., Wadhwa M., Gaffney A., Shafer J., Geissman J., Atudorei N. V., Herd C., Weiss B. P., King P. L., Crowther S. A. and Gilmour J. D. (2010) Non-basaltic asteroidal magmatism during the earliest stages of solar system evolution: A view from Antarctic achondrites Graves Nunatak 06128 and 06129. *Geochim. Cosmochim. Acta* **74**, 1172–1199.

Shirai N., Humayun M. and Righter K. (2009) Analysis of moderately siderophile elements in angrites: Implications for core formation of the angrite parent body. *Lunar Planet. Sci. XL* #2122 (abstract).

Shukolyukov A. and Lugmair G. W. (2004) Manganese-chromium isotope systematics of enstatite meteorites. *Geochim. Cosmochim. Acta* **68**, 2875–2888.

Sikdar J. and Rai V. K. (2017) Simultaneous chromatographic purification of Si and Mg for isotopic analyses using MC-ICPMS. *J. Anal. At. Spectrom.* **32**, 822–833.

Sikdar J. and Rai V. K. (2020) Si-Mg isotopes in enstatite chondrites and accretion of reduced planetary bodies. *Sci. Rep.* **10**, 1–12.

Sossi P. A. and Moynier F. (2017) Chemical and isotopic kinship of iron in the Earth and Moon deduced from the lunar Mg-Suite. *Earth Planet. Sci. Lett.* **471**, 125–135.

Sossi P. A., Foden J. D. and Halverson G. P. (2012) Redox-controlled iron isotope fractionation during magmatic differentiation: An example from the Red Hill intrusion, S. Tasmania. *Contrib. to Mineral. Petrol.* **164**, 757–772.

Sossi P. A., Nebel O., Anand M. and Poitrasson F. (2016a) On the iron isotope composition of Mars and volatile depletion in the terrestrial planets. *Earth Planet. Sci. Lett.* **449**, 360–371.

Sossi P. A., Nebel O. and Foden J. (2016b) Iron isotope systematics in planetary reservoirs. *Earth Planet. Sci. Lett.* **452**, 295–308.

Srinivasan P., Dunlap D. R., Agee C. B., Wadhwa M., Coleff D., Ziegler K., Zeigler R. and McCubbin F. M. (2018) Silica-rich volcanism in the early solar system dated at 4.565 Ga. *Nat. Commun.* **9**, 1–8.

Steenstra E. S., Knibbe J. S., Rai N. and van Westrenen W. (2016) Constraints on core formation in Vesta from metal-silicate partitioning of siderophile elements. *Geochim. Cosmochim. Acta* **177**, 48–61.

Steenstra E. S., Sitabi A. B., Lin Y. H., Rai N., Knibbe J. S., Berndt J., Matveev S. and van Westrenen W. (2017) The effect of melt composition on metal-silicate partitioning of siderophile elements and constraints on core formation in the angrite parent body. *Geochim. Cosmochim. Acta* **212**, 62–83.

Sugiura N. and Fujiya W. (2014) Correlated accretion ages and ε^{54}Cr of meteorite parent bodies and the evolution of the solar nebula. *Meteorit. Planet. Sci.* **49**, 772–787.

Sutton J. N., André L., Cardinal D., Conley D. J., De Souza G. F., Dean J., Dodd J., Ehlert C., Ellwood M. J., Frings P. J., Grasse P., Hendry K., Leng M. J., Michalopoulos P., Panizzo V. N. and Swann G. E. A. (2018) A review of the stable isotope bio-geochemistry of the global silicon cycle and its associated trace elements. *Front. Earth Sci.* **5**.

Sutton S. R., Goodrich C. A. and Wirick S. (2017) Titanium, vanadium and chromium valences in silicates of ungrouped achondrite NWA 7325 and ureilite Y-791538 record highly-reduced origins. *Geochim. Cosmochim. Acta* **204**, 313–330.

Swindle T. D., Kring D. A., Burkland M. K., Hill D. H. and Boynton W. V. (1998) Noble gases, bulk chemistry, and petrography of olivine-rich achondrites Eagles Nest and Lewis Cliff 88763: Comparison to brachinites. *Meteorit. Planet. Sci.* **33**, 31–48.

Takafuji N., Hirose K., Mitome M. and Bando Y. (2005) Solubilities of O and Si in liquid iron in equilibrium with (Mg,Fe)SiO3 perovskite and the light elements in the core. *Geophys. Res. Lett.* **32**, 1–4.

Taylor G. J. (1992) Core formation in asteroids. *J. Geophys. Res.* **97**, 717–726.

Telus M., Dauphas N., Moynier F., Tissot F. L. H., Teng F. Z., Nabelek P. I., Craddock P. R. and Groat L. A. (2012) Iron, zinc, magnesium and uranium isotopic fractionation during continental crust differentiation: The tale from migmatites, granitoids, and pegmatites. *Geochim. Cosmochim. Acta* **97**, 247–265.

Teng F. Z., Dauphas N. and Helz R. T. (2008) Iron isotope fractionation during magmatic differentiation in Kilauea Iki lava lake. *Science* **320**, 1620–1622.

Teng F. Z., Dauphas N., Huang S. and Marty B. (2013) Iron isotopic systematics of oceanic basalts. *Geochim. Cosmochim. Acta* **107**, 12–26.

Teng F. Z., Watkins J. M., Dauphas N. (2017) Non-Traditional Stable Isotopes. *Reviews in Mineralogy and Geochemistry* **82**. Mineralogical Society of America.

Terasaki H., Frost D. J. and Rubie D. C., Langenhorst, F. (2008) Percolative core formation in planetesimals. *Earth Planet. Sci. Lett.* **273**, 132–137.

The Japan Society for the Promotion of Science and The Nineteenth Committee on Steelmaking Part 2: Recommended values of activity and activity coefficients, and interaction parameters of elements in iron alloys (1988). *Steelmaking Data Sourcebook*. Gordon and Breach Science Publishers, New York. pp. 273–297.

Theis, K. J., Burgess, R., Lyon, I. C. and Sears, D. W. (2008) The origin and history of ordinary chondrites: A study by iron isotope measurements of metal grains from ordinary chondrites. *Geochim. Cosmochim. Acta* **72**, 4440–4456.

Trinquier A., Elliott T., Ulfbeck D., Coath C., Krot A. N. and Bizzarro M. (2009) Origin of Nucleosynthetic Isotope Heterogeneity in the Solar Protoplanetary Disk. *Science* **324**, 374–377.

Urey H.C. (1947) The thermodynamic properties of isotopic substances. *J. Chem. Soc*. 562–581.

Usui T., Jones J. H. and Mittlefehldt D. W. (2015) A partial melting study of an ordinary (H) chondrite composition with application to the unique achondrite Graves Nunataks 06128 and 06129. *Meteorit. Planet. Sci.* **50**, 759–781.

Van Den Boorn S. H. J. M., Vroon P. Z., Van Belle C. C., Van Der Wagt B., Schwieters J. and Van Bergen M. J. (2006) Determination of silicon isotope ratios in silicate materials by high-resolution MC-ICP-MS using a sodium hydroxide sample digestion method. *J. Anal. At. Spectrom.* **21**, 734–742.

Wade, J. and Wood, B. J. (2005) Core formation and the oxidation state of the Earth. *Earth Planet. Sci. Lett.* **236**, 78–95.

Wade J. and Wood B. J. (2016) The oxidation state and mass of the Moon-forming impactor. *Earth Planet. Sci. Lett.* **442**, 186–193.

Wadhwa M. (2008) Redox conditions on small bodies, the Moon and Mars. *Reviews in Mineralogy & Geochemistry.* **68**, 493–510.

Wadhwa, M., Shukolyukov, A., Lugmair, G.W. (1998a) ^{53}Mn–^{53}Cr systematics in Brachina: a record of one of the earliest phases of igneous activity on an asteroid (abstract). *Lunar Planet. Sci. XXIX* (#1480-CD-ROM).

Wadhwa, M., Zipfel, J., Davis, A.M. (1998b) Constraints on the formation history of brachinites from rare-earth-element distributions (abstract). *Meteorit. Planet. Sci.* **33** (Suppl.), A161.

Wahl S. M. and Militzer B. (2015) High-temperature miscibility of iron and rock during terrestrial planet formation. *Earth Planet. Sci. Lett.* **410**, 25–33.

Wang K., Moynier F., Dauphas N., Barrat J. A., Craddock P. and Sio C. K. (2012) Iron isotope fractionation in planetary crusts. *Geochim. Cosmochim. Acta* **89**, 31–45.

Wang K., Day J. M. D., Korotev R. L., Zeigler R. A. and Moynier F. (2014a) Iron isotope fractionation during sulfide-rich felsic partial melting in early planetesimals. *Earth Planet. Sci. Lett.* **392**, 124–132.

Wang K., Savage P. S. and Moynier F. (2014b) The iron isotope composition of enstatite meteorites: Implications for their origin and the metal/sulfide Fe isotopic fractionation factor. *Geochim. Cosmochim. Acta* **142**, 149–165.

Wang K., Jacobsen S. B., Sedaghatpour F., Chen H. and Korotev R. L. (2015) The earliest Lunar Magma Ocean differentiation recorded in Fe isotopes. *Earth Planet. Sci. Lett.* **430**, 202–208.

Wang W., Wei H. Z., Jiang S. Y., Liu X., Lei F., Lin Y. B., Zhao Y. (2019) Applications G. Silicon Isotope Geochemistry: Fractionation Linked to Silicon Complexations and Its Geological Applications. *Molecules* **24**, 1415.

Warren P. H. (2011) Stable-isotopic anomalies and the accretionary assemblage of the Earth and Mars: A subordinate role for carbonaceous chondrites. *Earth Planet. Sci. Lett.* **311**, 93–100.

Warren P. H. and Kallemeyn G. W. (1989) Allan Hills 84025: the second brachinite, far more differentiated than Brachina, and an ultramafic achondritic clast from

L chondrite Yamato 75097. *Proceedings of the 19th Lunar Planetary Science Conference*, pp. 475–486.

Warren P. H., Rubin A. E., Isa J., Brittenham S., Ahn I. and Choi B. G. (2013) Northwest Africa 6693: A new type of FeO-rich, low-Δ17O, poikilitic cumulate achondrite. *Geochim. Cosmochim. Acta* **107**, 135–154.

Wasson, J.T., Kallemeyn, G.W. and Rubin, A.E. (1994) Equilibration temperatures of EL chondrites: a major downward revision in the ferrosilite contents of enstatite. *Meteoritics* **29**, 658–662.

Watters T. R. and Prinz M. (1979) Aubrites: Their origin and relationship to enstatite chondrites. *Proc. Lunar Planet Sci. Conf. X*, 1073–1093.

Watters, T. R. and Prinz, M. (1980) Mt. Egerton and the aubrite parent body. *Lunar Planet. Sci. Conf. XI*, 1225-1226.

Weider S. Z., Nittler L. R., Starr R. D., McCoy T. J., Stockstill-Cahill K. R., Byrne P. K., Denevi B. W., Head J. W. and Solomon S. C. (2012) Chemical heterogeneity on Mercury's surface revealed by the MESSENGER X-Ray Spectrometer. *J. Geophys. Res. E Planets* **117**, 1–15.

Weiss B. P., Berdahl J. S., Elkins-Tanton L., Stanley S., Lima E. A. and Carporzen L. (2008) Magnetism on the angrite parent body and the early differentiation of planetesimals. *Science* **322**, 713–716.

Weyer S. and Ionov D. A. (2007) Partial melting and melt percolation in the mantle: The message from Fe isotopes. *Earth Planet. Sci. Lett.* **259**, 119–133.

Weyer S., Anbar A. D., Brey G. P., Münker C., Mezger K. and Woodland A. B. (2005) Iron isotope fractionation during planetary differentiation. *Earth Planet. Sci. Lett.* **240**, 251–264.

Williams H. M., McCammon C. A., Peslier A. H., Halliday A. N., Teutsch N., Levasseur S. and Burg J. P. (2004) Iron isotope fractionation and the oxygen fugacity of the mantle. *Science* **304**, 1656–1659.

Williams H. M., Peslier A. H., McCammon C., Halliday A. N., Levasseur S., Teutsch N. and Burg J. P. (2005) Systematic iron isotope variations in mantle rocks and minerals: The effects of partial melting and oxygen fugacity. *Earth Planet. Sci. Lett*. **235**, 435–452.

Williams H. M., Markowski A., Quitté G., Halliday A. N., Teutsch N. and Levasseur S. (2006) Fe isotope fractionation in iron meteorites: New insights into metal-sulphide segregation and planetary accretion. *Earth Planet. Sci. Lett.* **250**, 486–500.

Williams H. M., Nielsen S. G., Renac C., Griffin W. L., O'Reilly S. Y., McCammon C. A., Pearson N., Viljoen F., Alt J. C. and Halliday A. N. (2009) Fractionation of oxygen and iron isotopes by partial melting processes: Implications for the

interpretation of stable isotope signatures in mafic rocks. *Earth Planet. Sci. Lett.* **283**, 156–166.

Williams H. M., Wood B. J., Wade J., Frost D. J. and Tuff J. (2012) Isotopic evidence for internal oxidation of the Earth's mantle during accretion. *Earth Planet. Sci. Lett.* **321**–**322**, 54–63.

Wilson L. and Keil K. (1991) Consequences of explosive eruptions on small Solar System bodies: the case of the missing basalts on the aubrite parent body. *Earth Planet. Sci. Lett.* **104**, 505–512.

Yamaguchi A., Clayton R. N., Mayeda T. K., Ebihara M., Oura Y., Miura Y. N., Haramura H., Misawa K., Kojima H. and Nagao K. (2002) A new source of basaltic meteorites inferred from Northwest Africa 011. *Science* **296**, 334–336.

Yoshizaki T. and McDonough W. F. (2020) The composition of Mars. *Geochim. Cosmochim. Acta* **273**, 137–162.

Young E. D., Tonui E., Manning C. E., Schauble E. and Macris C. A. (2009) Spinel-olivine magnesium isotope thermometry in the mantle and implications for the Mg isotopic composition of Earth. *Earth Planet. Sci. Lett.* **288**, 524–533.

Young E. D., Manning C. E., Schauble E. A., Shahar A., Macris C. A., Lazar C. and Jordan M. (2015) High-temperature equilibrium isotope fractionation of non-traditional stable isotopes: Experiments, theory, and applications. *Chem. Geol.* **395**, 176–195.

Young E. D., Shahar A., Nimmo F., Schlichting H. E., Schauble E. A., Tang H. and Labidi J. (2019) Near-equilibrium isotope fractionation during planetesimal evaporation. *Icarus* **323**, 1–15.

Zambardi T. and Poitrasson F. (2011) Precise Determination of Silicon Isotopes in Silicate Rock Reference Materials by MC-ICP-MS. *Geostand. Geoanalytical Res.* **35**, 89–99.

Zambardi T., Poitrasson F., Corgne A., Méheut M., Quitté G. and Anand M. (2013) Silicon isotope variations in the inner solar system: Implications for planetary formation, differentiation and composition. *Geochim. Cosmochim. Acta* **121**, 67–83.

Zambardi T., Lundstrom C. C., Li X. and McCurry M. (2014) Fe and Si isotope variations at Cedar Butte volcano; insight into magmatic differentiation. *Earth Planet. Sci. Lett.* **405**, 169–179.

Zhu X. K., Guo Y., O'Nions R. K., Young E. D. and Ash R. D. (2001) Isotopic homogeneity of iron in the early solar nebula. *Nature* **412**, 311–313.

Ziegler R. A., Jolliff B., Korotev R., Rumble D., Carpenter P.K. and Wang A. (2008) Petrology, geochemistry and likely provenance of unique achondrite Graves Nunatak 06128. *Lunar and Planetary Sci. XLIX,* #2456 (abstr.).

Ziegler K., Young E. D., Schauble E. A. and Wasson J. T. (2010) Metal-silicate silicon isotope fractionation in enstatite meteorites and constraints on Earth's core formation. *Earth Planet. Sci. Lett.* **295**, 487–496.

APPENDIX A

SUPPLEMENTARY MATERIAL FOR CHAPTER 3

Supplementary Table A3.1: Parameters used to calculate the metal-silicate equilibration temperature (T in Kelvin) of aubrite metals.

Parameters	values
(*nbo/t*)*	1.74
a**	2.97
b**	-21800
c**	-11
d**	-0.24
γ_{Fe}^{metal}**	0.8
γ_{Si}^{0} †	0.0013 at 1873 K
ε_{Si}^{Si} †	0.103 at 1873 K
ε_{Si}^{Ni} †	0.005 at 1873 K
ε_{Si}^{P} †	0.09 at 1873 K

* For calculating T, *nbo/t* is the average value for all experiments with starting composition (SM-2) similar to E-chondrite. Values adapted from Table 2 of previous study[1].
** Adapted values[1].
† Adapted values[2].
The x_i^{phase} used for calculation of T for each metal is given in Supplementary Table A3.2.

Supplementary Table A3.2: Molar fraction (x_i^{phase}) of component '*i*' in the phase of interest. The values for x_i^{metal} have been calculated from elemental composition given in Table 3.1. Values for $x_i^{silicate}$ have been calculated using published data[3]. For each meteorite, $x_i^{silicate}$ is the weighted average of the mole fractions of '*i*' in various silicates present in that particular meteorite.

Samples	x_{Fe}^{metal}	x_{Si}^{metal}	x_{Ni}^{metal}	x_{Co}^{metal}	x_{P}^{metal}	$x_{SiO_2}^{silicate}$	$x_{FeO}^{silicate}$
NC2	0.908199	0.015875	0.066962	0.008254	0.000711	0.473208	0.000437
NC3	0.925137	0.007495	0.056820	0.009296	0.001252	0.473208	0.000437
NC4	0.932362	0.005701	0.053058	0.007097	0.001783	0.473208	0.000437
NC6	0.929859	0.006266	0.054816	0.007461	0.001598	0.473208	0.000437
NC7	0.904802	0.032682	0.054409	0.006279	0.001828	0.473208	0.000437
NC8	0.904239	0.027397	0.061400	0.005534	0.001430	0.473208	0.000437
NC9	0.892520	0.041172	0.058825	0.006426	0.001057	0.473208	0.000437
NC10	0.895092	0.034393	0.062727	0.006897	0.000891	0.473208	0.000437
NC11	0.911620	0.012726	0.067651	0.006380	0.001623	0.473208	0.000437
NC12	0.900899	0.014544	0.076937	0.005993	0.001626	0.473208	0.000437
ME1	0.900992	0.039138	0.051643	0.006985	0.001242	0.499335	0.000488
ME2	0.888494	0.038952	0.064678	0.006640	0.001236	0.499335	0.000488
ME3	0.890667	0.039088	0.062236	0.006599	0.001411	0.499335	0.000488
ME4	0.894279	0.040223	0.057184	0.006721	0.001593	0.499335	0.000488
BSP3	0.932745	0.001937	0.057272	0.006966	0.001080	0.525280	0.000459
SW1	0.919705	0.017365	0.049161	0.007331	0.006438	0.444562	0.000354
SW3	0.890702	0.017135	0.081975	0.005916	0.004271	0.444562	0.000354

Supplementary Table A3.3: Parameters used to calculate temperature (T in Kelvin) at different radial distances (r) from the center of the aubrite parent body using equation (3.11).

	Parameters	Value	Units	Reference
T_0	Ambient temperature	280* and 194** at 1.5 Myr† 305* and 208** at 1.3 Myr† 335* and 230** at 1.0 Myr†	K	[4]
K	Thermal conductivity	5 at 1 AU 5.3 at 2 AU	W m^{-1} K^{-1}	[5,6]
ρ	Density of ECs	3550	kg m^{-3}	[7]
C_P	Specific heat capacity	800 at 1 AU 540 at 2 AU	J kg^{-1} K^{-1}	[8]
κ	Thermal diffusivity	1.76×10^{-6} at 1 AU 2.76×10^{-6} at 2 AU	m^2 s^{-1}	$K/\rho C_P$
A_0	Power output per unit volume	1.37×10^{-4} at 1.5 Myr† 1.67×10^{-4} at 1.3 Myr† 2.24×10^{-4} at 1.0 Myr †	W m^{-3}	See below for details
λ	Decay constant of ^{26}Al	3.1170×10^{-14}	s^{-1}	$ln\,(2)/T_{1/2}$
$T_{1/2}$	Half-life of ^{26}Al	705000	yr	[9]
R	Radius of aubrite parent body	100	km	[10]

* T_0 in Kelvin at 1 AU from the Sun
** T_0 in Kelvin at 2 AU from the Sun
† Time of accretion after CAI formation

Calculation of the power output per unit volume at the time of planetesimal formation (A_0)

The energy per decay of ^{26}Al can be converted to the heat output (H_0) per unit mass in W/kg according to,

$$\mathrm{H_0} = \frac{\mathrm{N_A}}{\mathrm{m_{26}}}\mathrm{E_d e_v \lambda}$$

where,
N_A (Avogadro's number) = 6.0221415×10^{23}
m_{26} (mass of 1 mole of ^{26}Al) = 25.987×10^{-3} kg
E_d (amount of energy released per decay) =3.12 MeV[11]
e_v = 1.60217646×10^{-19} J/eV
λ (decay constant of ^{26}Al) = 3.1170×10^{-14} s^{-1}

Then, A_0 which is the power output per unit volume at the time of planetesimal formation in W/m^3 can be calculated according to,

$$\mathrm{A_0} = \mathrm{H_0}\rho x \mathrm{C} e^{-\lambda t_{acc}}$$

where,

ρ (density) = 3550 kg/m^3 for enstatite chondrites[7].
x (weight fraction of Al in solid) = 0.00889; average value of enstatite chondrites[12].
C (canonical ^{26}Al/^{27}Al ratio) = 5.25×10^{-5} as shown in previous work[13].
t_{acc} (time of accretion of planetesimal relative to CAI formation); given that this is estimated to have an upper limit of ~1.5 Myr[14], we used values of 1.0, 1.3, and 1.5 Myr for illustrative purposes.

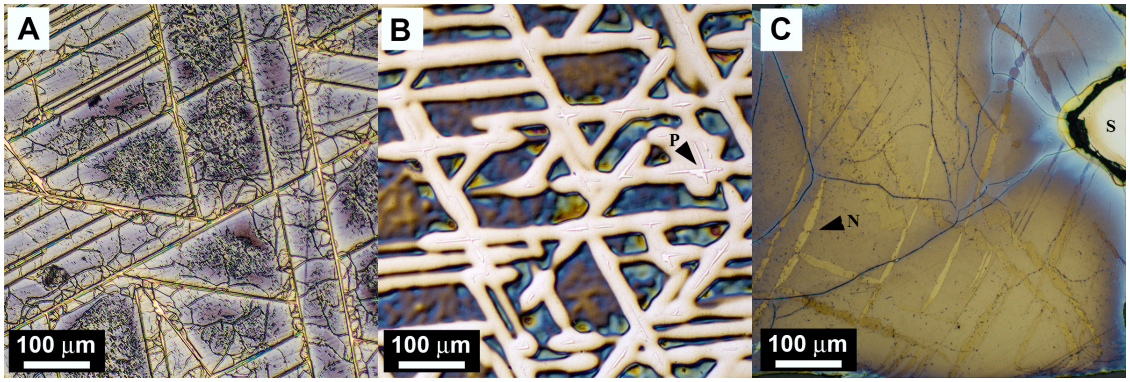

Supplementary Figure A3.1. Representative reflected light photographs of polished and stain-etched pieces of A) Norton County nodule NC8, B) Mount Egerton ME1, and C) Bishopville nodule BSP3. The sodium bisulfite stain-etch colors the Ni-poor kamacite shades of tan-purple-blue, whereas high Ni-metal and the inclusions remain unstained and shiny. The Norton County nodule NC8 (A) clearly shows the linear inclusions of perryite that divide the surface into triangular and trapezoidal regions. A similar pattern is shown by the Mount Egerton ME1 nodule (B), though perryite only forms discontinuous linear grains (region P indicated by arrow) within Ni-rich linear metal (bright lath-like features). Bishopville is dominated by kamacite and lacks perryite. S – schreibersite, N – Neumann band.

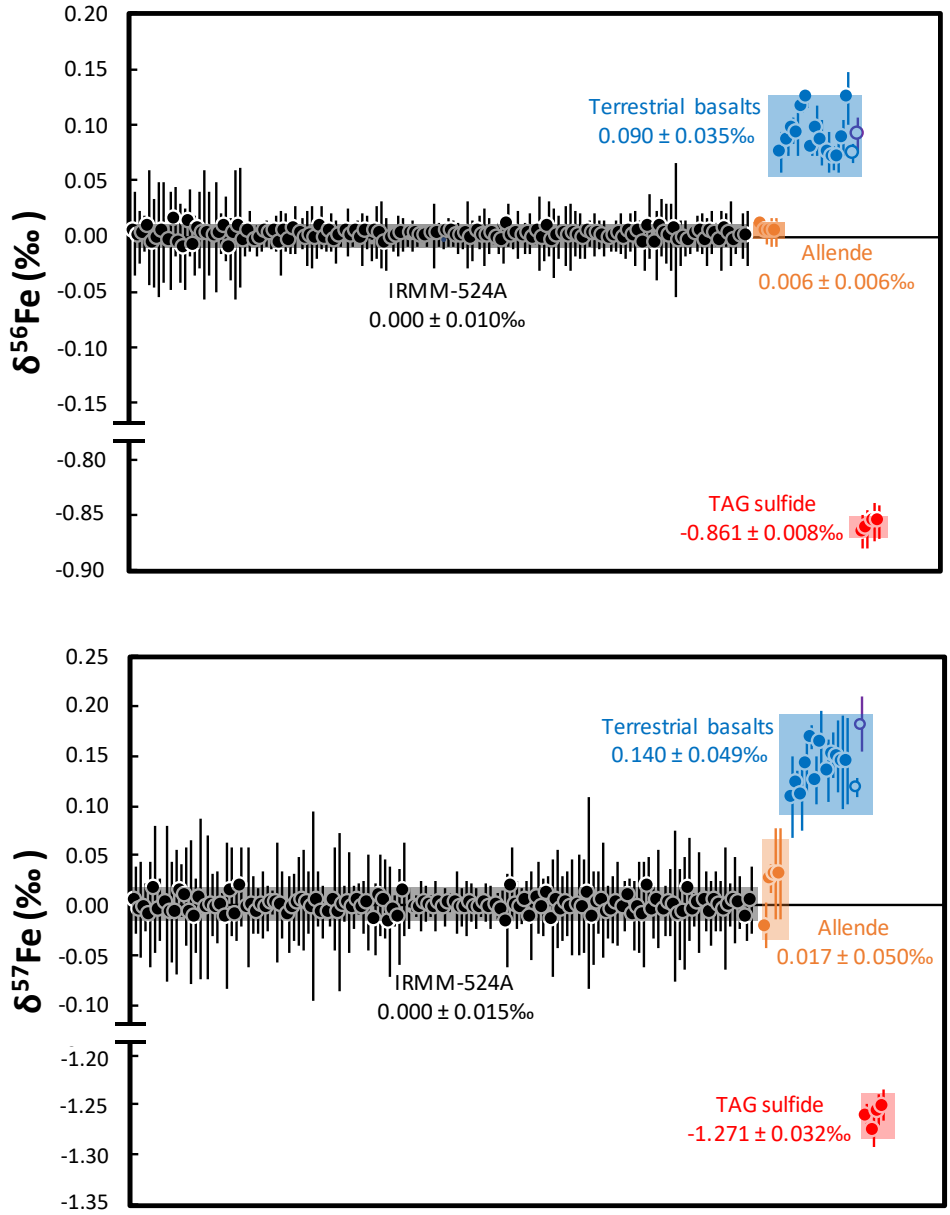

Supplementary Figure A3.2. Long-term external reproducibility of Fe isotope analyses in the Isotope Cosmochemistry and Geochronology Laboratory (ICGL) at ASU. Each data point represents an average of six repeat runs and is plotted with its 2SE uncertainty. Black circles show data for the IRMM-524A standard. Data for homogenized Allende powder is shown as orange circles; terrestrial basalt standards analyzed include BCR-2 (solid circles), BIR (blue open circle), and BHVO-1 (purple open circle); data for the Trans-Atlantic Geotraverse (TAG) sulfide are shown as the red circles. The shaded colored boxes represent the average (± 2SD) of all analyses for a given standard.

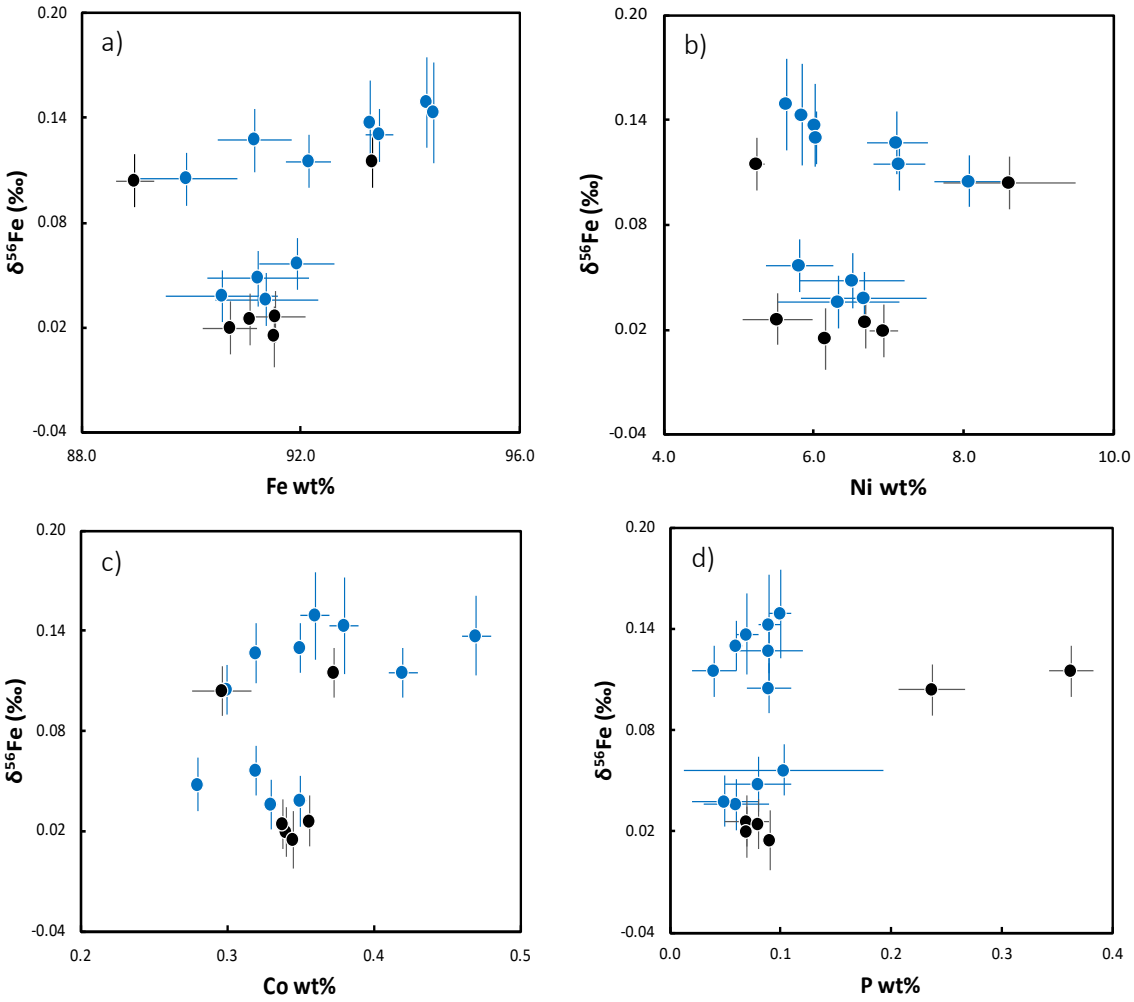

Supplementary Figure A3.3. δ^{56}Fe versus (a) Fe, (b) Ni, (c) Co, and (d) P content of the aubrite metals. Blue symbols are for metals from brecciated aubrites (Norton County and Bishopville) and black symbols are for metals from non-brecciated aubrites (Shallowater and Mount Egerton).

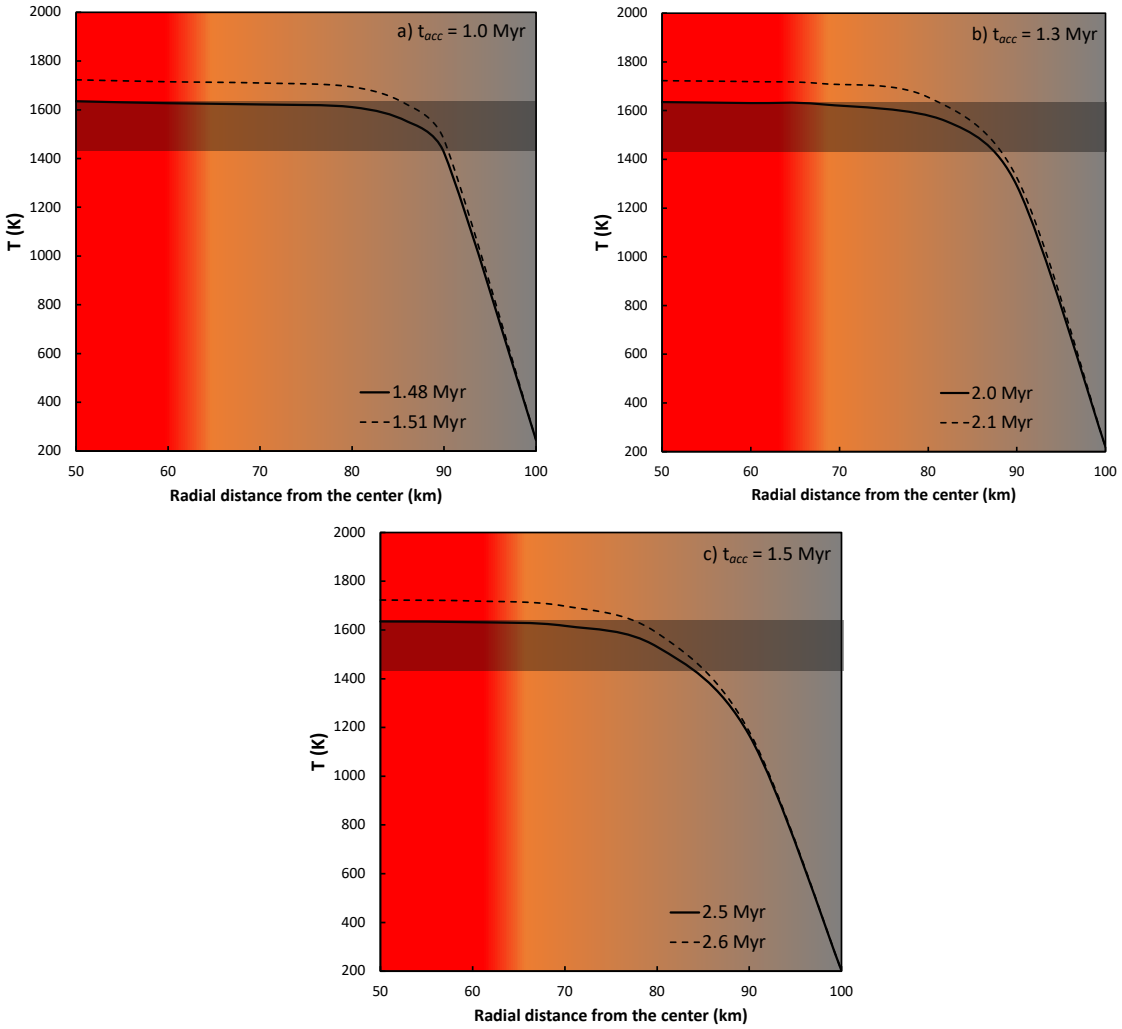

Supplementary Figure A3.4. The calculated temperature (T in Kelvin) versus radial distance (r in km) from the center of the 200 km diameter aubrite parent body at 2 AU from the Sun[4] at different times (shown by solid and dashed curves) assuming that the time of accretion (t_{acc}) was (a) 1.0 Myr; (b) 1.3 Myr; and (c) 1.5 Myr after CAI formation. The parameters used for these calculations are listed in Supplementary Table A3.3. Warmer colors represent higher temperatures with increasing depth from the surface. The black solid curve corresponds to the thermal profile with peak T of 1635 K (i.e., the highest estimated metal-silicate equilibration temperature recorded in the aubrite metals in this study). The black dashed curve represents the thermal gradient with peak T of 1723 K beyond which >50% silicate melting would lead to obliteration of the thermal gradient in the AuPB (see text for details). Horizontal gray bar illustrates the range of metal-silicate equilibration temperatures (1432–1635 K) estimated for the aubrite metals in this study. The thermal gradient within the AuPB inferred from the metal-silicate equilibration temperatures recorded by the aubrite metals in this study is attained by (a) 1.48–1.51 Myr (for t_{acc}= 1.0 Myr), (b) 2.0–2.1 Myr (for t_{acc}= 1.3 Myr), and (c) 2.5–2.6 Myr (for t_{acc}= 1.5 Myr) after CAI formation.

SUPPLEMENTARY REFERENCES

1. Corgne, A., Keshav, S., Wood, B. J., McDonough, W. F. & Fei, Y. Metal-silicate partitioning and constraints on core composition and oxygen fugacity during Earth accretion. *Geochim. Cosmochim. Acta* **72**, 574–589 (2008).

2. The Japan Society for the Promotion of Science and The Nineteenth Committee on Steelmaking Part 2: Recommended values of activity and activity coefficients, and interaction parameters of elements in iron alloys. In *Steelmaking Data Sourcebook*. Gordon and Breach Science Publishers, New York. pp. 273–297 (1988).

3. Watters, T. R. & Prinz, M. Aubrites: Their origin and relationship to enstatite chondrites. *Proc. Lunar Planet. Sci Conf.* **X**, 1073-1093 (1979).

4. Desch, S. J., Kalyaan, A. & Alexander C. M. O. The Effect of Jupiter's Formation on the Distribution of Refractory Elements and Inclusions in Meteorites. *Astrophys. J. Suppl. Ser.* **238**, 11 (2018).

5. Opeil, C. P., Consolmagno, G. J. & Britt, D. T. The thermal conductivity of meteorites: New measurements and analysis. *Icarus* **208**, 449–454 (2010).

6. Opeil, C. P., Consolmagno, G. J., Safarik, D. J. & Britt, D. T. Stony meteorite thermal properties and their relationship with meteorite chemical and physical states. *Meteorit. Planet. Sci.* **47**, 319–329 (2012).

7. Macke, R. J., Consolmagno, G. J., Britt, D. T. & Hutson, M. L. Enstatite chondrite density, magnetic susceptibility, and porosity. *Meteorit. Planet. Sci.* **45**, 1513–1526 (2010).

8. Flynn, G. J., Consolmagno, G. J., Brown, P. & Macke, R. J. Physical properties of the stone meteorites: Implications for the properties of their parent bodies. *Chemie der Erde* **78**, 269–298 (2018).

9. Norris, T. L., Gancarz, A. J., Rokop, D. J. & Thomas, K. W. Half-life of ^{26}Al. *J. Geophys. Res. Solid Earth* **88**, B331–B333 (1983).

10. Wilson, L. & Keil, K. Consequences of explosive eruptions on small Solar System bodies: the case of the missing basalts on the aubrite parent body. *Earth Planet. Sci. Lett.* **104**, 505–512 (1991).

11. Castillo-Rogez, J., Johnson, T. V., Lee, M. H., Turner, N. J., Matson, D. L. & Lunine, J. ^{26}Al decay: Heat production and a revised age for Iapetus. *Icarus* **204**, 658–662 (2009).

12. Kong, P., Mori, T. & Ebihara, M. Compositional continuity of enstatite chondrites and implications for heterogeneous accretion of the enstatite chondrite parent body. *Geochim. Cosmochim. Acta* **61**, 4895–4914 (1997).

13. Kita, N. T. *et al.* ^{26}Al-^{26}Mg isotope systematics of the first solids in the early solar system. *Meteorit. Planet. Sci.* **48**, 1383–1400 (2013).

14. Sugiura, N. &Fujiya, W. Correlated accretion ages and ε^{54}Cr of meteorite parent bodies and the evolution of the solar nebula. *Meteorit. Planet. Sci.* **49**, 772–787 (2014).

APPENDIX B

SUPPLEMENTARY MATERIAL FOR CHAPTER 5

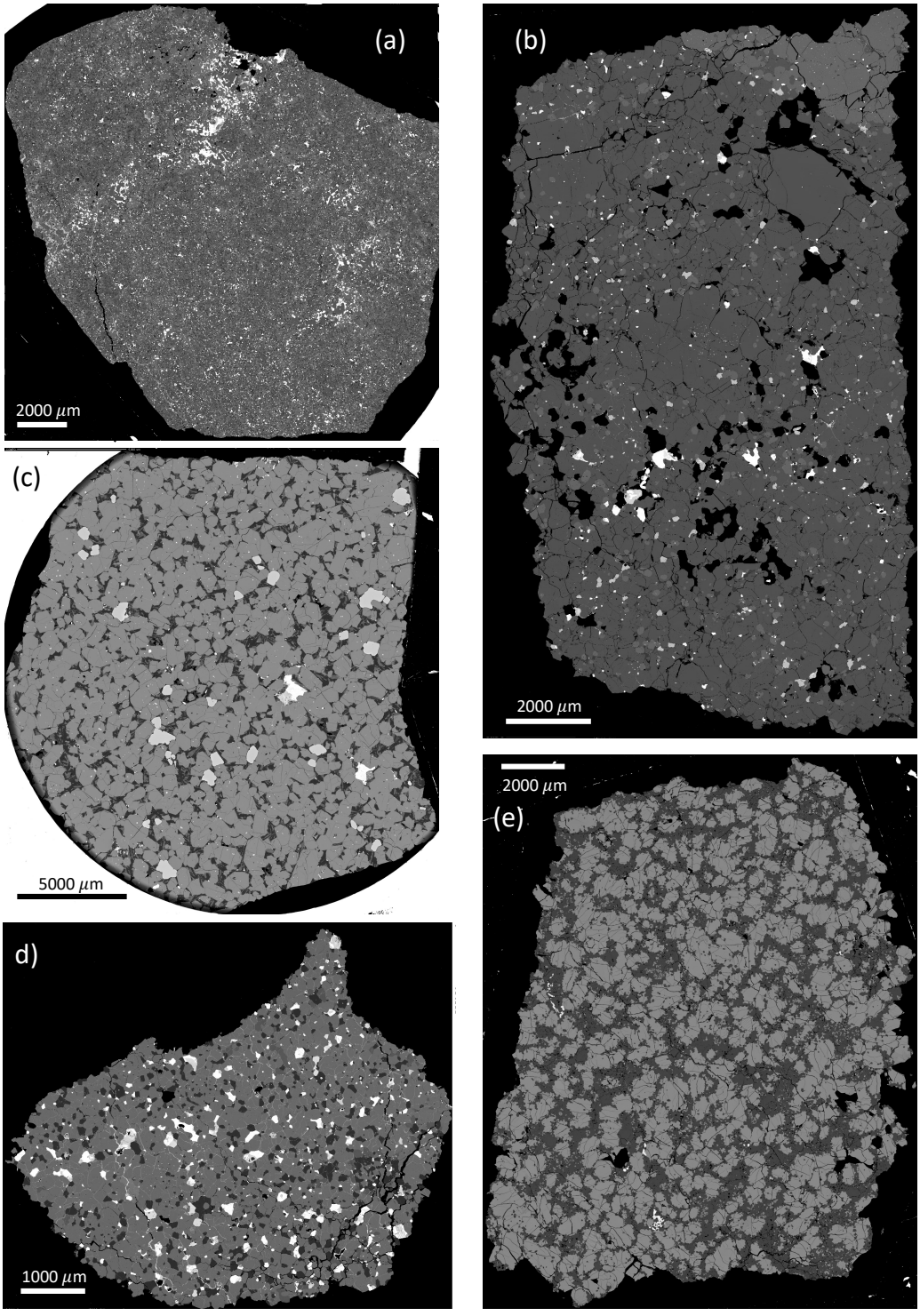
(a)
2000 μm
(b)
2000 μm
(c)
5000 μm
2000 μm
(e)
d)
1000 μm

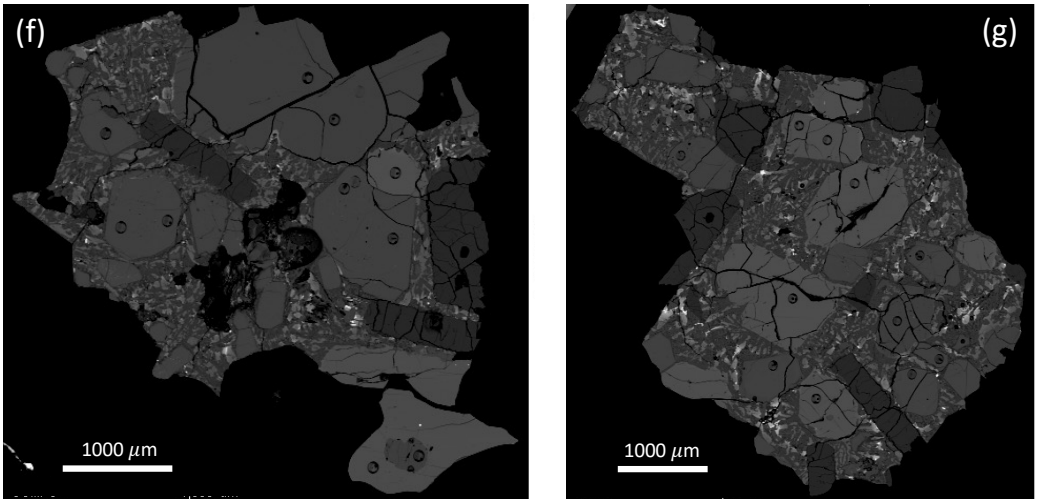

Supplementary Figure B5.1. Back-scattered electron images of the achondrites for which equilibration temperatures and oxygen fugacities were calculated in this study. (a) NWA 5297, (b) NWA 8777, (c) NWA 6962, (d) NWA 10503 (e) NWA 2976, (f) and (g) NWA 11119. Images and compositional data for NWA 8777 (except metal data) and NWA 10503 are from Dr. Devin Schrader. The sample NWA 11119 was loaned by Dr. Audrey Bouvier. All other samples were acquired from the Center for Meteorite Studies at ASU.

APPENDIX C

STATEMENT OF CO-AUTHORS

Chapter 2, Chapter 3, Chapter 4, and Chapter 5 of this dissertation are all co-authored manuscripts in various stages of publication or preparation for publication. Chapter 3 is currently in review at Nature Scientific Reports while Chapters 2,4, and 5 are in preparation for submission. I am the first author of each of these co-authored manuscripts, and all co-authors (listed below) have given their permission for the use of these documents in this dissertation.

Chapter 2 co-authors: Vinai K. Rai, Rebekah R. Hines, and Meenakshi Wadhwa.

Chapter 3 co-authors: Laurence A. J. Garvie, Vinai K. Rai, and Meenakshi Wadhwa.

Chapter 4 co-authors: Vinai K. Rai, and Meenakshi Wadhwa.

Chapter 5 co-authors: Devin L. Schrader, Vinai K. Rai, and Meenakshi Wadhwa.